# Performance Analysis of Wireless Powered Communication Networks with Imperfect CSI and Nonlinear Energy Harvesters

by

## Danyang Wang

A thesis submitted in partial fulfillment of the requirements for the degree of

Master of Science

in

Communications

Department of Electrical and Computer Engineering

University of Alberta

# Abstract

Harvesting energy from radio frequency signals is a promising solution to enhance the energy efficiency of portable wireless devices and/or wireless sensors. Toward this goal, in this thesis, wireless powered communication networks are studied. Such a network consists of a hybrid access point or a power beacon that transfers energy to the user. The user device then transmits data in the uplink by using its harvested energy. Performances of wireless powered communication networks are investigated in detail based on two practical scenarios: imperfect channel state information and nonlinear energy harvesting models. First, average throughput and average bit/symbol error rate are derived for imperfect channel state information case. Second, a new nonlinear energy harvesting model and its asymptotic version are proposed. The linear and rational energy harvesting models are also described for comparative purposes. The average throughput and average bit error rate of four energy harvesting models are investigated.

# Preface

Chapter 3 and Section 2.3 of the thesis has been accepted for the publication as D. Wang and C. Tellambura, "Performance Analysis of Energy Beamforming WPCN Links with Channel Estimation Errors," *IEEE Open Journal of the Communications Society.* in July, 2020. It also has been accepted for publication in part as D. Wang and C. Tellambura, "Exact and Asymptotic Performance Analysis of WPC Links with Channel Estimation Errors," in *Proceedings of the IEEE 92nd Vehicular Technology Conference (VTC2020-Fall)*, Victoria, Canada, October 2020.

Chapter 4 of the thesis has been submitted for the publication as D. Wang, F. Rezaei, and C. Tellambura, "Performance Analysis and Resource Allocations for a WPCN with a New Nonlinear Energy Harvester Model," *IEEE Open Journal of the Communications Society.* in July, 2020. I was responsible for the performance analysis and F. Rezaei was responsible for the resource allocation. Prof. Tellambura supervised us and edited the manuscript.

*Dedicated to my beloved parents.*

# Acknowledgements

My deepest gratitude goes first and foremost to my supervisor, Prof. Chintha Tellambura, for his technical guidance and invaluable support throughout my graduate studies. He has walked me through all the stages of the writing of this thesis. His enthusiasm and attitude towards research inspired me to explore more not only in graduate studies but also in my future life.

I would like to thanks members of my examining committee Prof. Hai Jiang and Prof. Majid Khabbazian. Thanks for their time and valuable feedback for improving the quality of the thesis. I am also deeply indebted to all the other professors who delivered lectures during my graduate study, faculty, and the administrative staff of the ECE for their direct and indirect help to me.

I would like to thank my labmates, including Fatemeh and Shashindra for the useful discussions we had and enjoyable times we spent together. I am also grateful to my classmates and friends in the ECE department. It has been a pleasure to study and work with them, and the intellectually challenging environment they create enhanced my learning experience.

Finally, I would like to express my deepest gratitude and respect to my family and my boyfriend for their loving considerations and great confidence in me all through these years.

# Contents

**Appendix B  Proofs for Chapter 4**                    **103**

# List of Tables

# List of Figures

# Chapter 1

# Introduction

## 1.1 The Evolution of Wireless Communications

Commercial wireless communications systems have evolved through several stages since the introduction of first generation (1G) in the 1980s. Each generation is a significant milestone in the development of wireless communications. This evolution is briefly discussed below.

- **First generation Wireless**

  The first generation mobile system was launched in 1979 in Japan by Nippon Telephone and Telegraph Corporation (NTT). 1G cellular telephone systems were based on frequency division multiple access (FDMA) and analog frequency modulation (FM) technology [1]. There were several drawbacks, such as poor voice quality, less security, limited to voice transmission, and the limited number of users as well as cellular coverage.

- **Second generation (2G) wireless**

  2G was first launched in Finland in 1991 based on the global systems for mobile communication (GSM) standard. Unlike 1G, the 2G system used digital mobile access technology such as time division multiple access (TDMA) and code division multiple access (CDMA) [2]. Since the 2G system used digital signals, the calls could be encrypted and the voice quality was better than the 1G system. In addition, 2G provided text, picture, and multiple media messages services.

- **Third generation (3G) Wireless**

  3G was commercially introduced in 2001. Two of the most widely used 3G standards are CDMA2000 (code division multiple access) and wideband code division multiple access (W-CDMA). CDMA2000 was based on IS-95 and IS95B technologies. 3G provided more services than 2G, such as mobile television, video conferencing, global positioning system (GPS), and better quality.

- **Fourth generation (4G) Wireless**

  4G system is an enhanced version of 3G. 4G has high speed (1 Gbps for stationary environments), high quality of service and high bandwidth efficiency (15 bits/s/Hz in the downlink and 6.75 bits/s/Hz) [1]. The two significant 4G standards are long term evolution (LTE) and worldwide interoperability for microwave access (WiMAX). 4G uses orthogonal frequency division multiple access (OFDMA) and single carrier frequency division multiple access (SC-FDMA).

- **Fifth generation (5G) Wireless**

  5G is currently being researched, developed and deployed. The complete deployment takes place between 2020 and 2030 [1], [3]. Compared to the previous generations, 5G has greater bandwidth (3.3–4.2 GHz), higher download data rate (up to 10 Gbit/s), lower latency (less than 1 milliseconds), and denser connectivity. Therefore, 5G provides more services than 4G, such as automated driving, mobile industrial automation, and smart cities in internet-of-things (IoT). 5G is the cornerstone of the growth of wireless devices.

## 1.2 Increased Demand for Wireless Devices

Wireless networks and devices have been developed rapidly and have become essential parts of daily life. For example, according to GSMA [4], the number of unique mobile subscribers is predicted to increase 1.9 % from 5.2 billion in 2019 to 5.8 billion in 2025. The use of smartphones increased from 65%
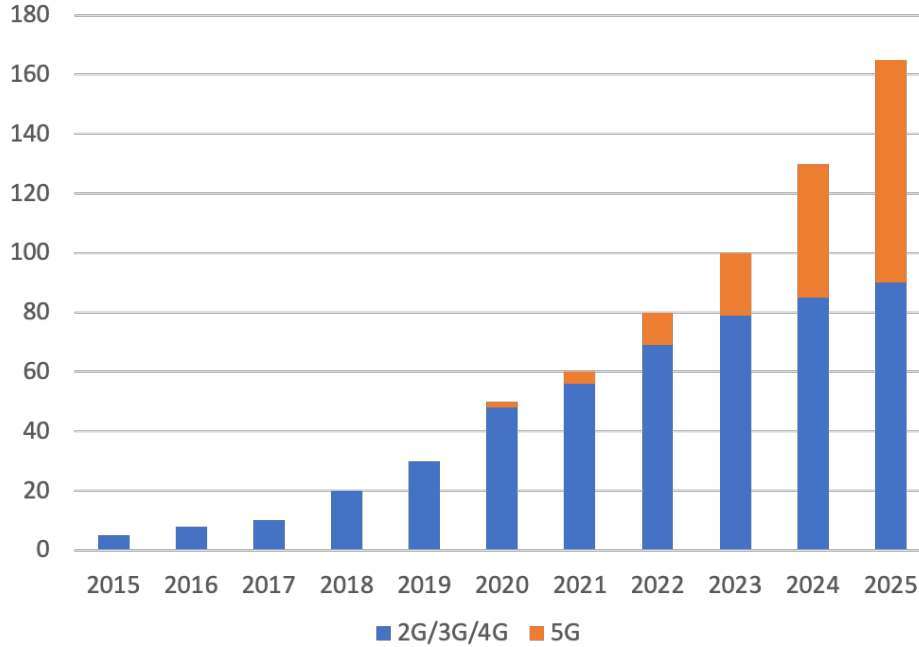
Figure 1.1:   Global mobile data traffic (EB per month) [6].

in 2019 to 80% in 2020.  The worldwide mobile data usage will grow from
7.5 GB per subscriber per month in 2019 to 28 GB per subscriber per month
in 2025, which is almost fourfold. Around 5.2 billion cellular IoT connections
are expected by 2025. However, there were only 1.5 billion connections in 2019,
which will increase 23% [5]. In Figure 1.1, the increase trend of global mobile
data traffic in exabytes (EB) per month is given. It will reach to 164 EB per
month in 2025.

   In order to address this growth, researchers have been developing several
technologies. These include the cognitive radio (CR) paradigm, which is based
various energy detection methods, which allows simultaneous spectrum access
for primary and secondary users in an interference tolerant basis, full duplex
radios, massive MIMO (multiple input multiple output), cooperative commu-
nications and others [7]–[11].

   With such a large increasing demand for wireless devices and nodes, the
lifetime of those energy-constrained devices/nodes is an essential issue and has
attracted a lot of research interests [12]–[15]. Large batteries could possibly
be used by wireless devices and nodes, but the problems are increased weight,

size, and cost [16]. Thus, the elimination or reduction of the use of batteries makes sense. Thus, a solution is i.e, wireless energy harvesting (EH) [12]. EH is a promising technique to improve the performance of energy-constrained wireless networks.

## 1.3  Wireless Energy Harvesting

Energy can be harvested from different sources. These sources are generally divided into four types: mechanical energy, thermoelectric energy, solar/light energy, and electromagnetic energy. All of them can be converted into electricity by different transducers [17]. Different energy sources may be influenced due to location, climate, and time.

Compared to conventional battery-powered networks, EH wireless communications networks provide several benefits. First, conventional devices depend on either batteries or cables to maintain the energy needed for communication. In some harsh environments (toxic, hostile, or inaccessible places), it is inconvenient to recharge and replace the batteries or connect devices with cables. Thus, EH helps in prolonging and self-sustaining the lifetime of battery-less or cable-free devices [12]. Second, unlike the energy from the power grid, the harvested energy from solar/light and mechanical energy (wind energy) are environmentally friendly. Although RF energy is not completely green, it is ubiquitous and ambient forms of it can power wireless devices.

## 1.4  Energy Sources

These sources can be generally divided into four types: mechanical energy, thermoelectric energy, solar/light energy and electromagnetic energy. These can be converted into electricity by different transducers.

### 1.4.1  Mechanical Energy

To convert mechanical motion, vibration, pressure or stress to electricity, electromagnetic, electrostatic and piezoelectric methods are available [18]. In the electromagnetic method, the relative motion between the magnet and the

metal coil can produce a current in the coil [19]. In the electrostatic method, the mechanical motion or vibration changes the distance between two electrodes of a capacitor to generate a current [18], while in the piezoelectric method, the current is generated by the mechanical strain acting on a layer of piezoelectric material.

## 1.4.2   Thermoelectric Energy

The thermoelectric effect is a direct conversion of the voltage generated by temperature differential between two different conductors. For example, one may harvest energy from the temperature gradient between human bodies and environment, but the power is relatively low and range from $10\,\mu W/cm^2$ to $1\,mW/cm^2$ [20].

## 1.4.3   Solar/Light Energy

Solar energy is one of the most popular green energy sources. To exploit this source, photons are converted into electricity through photovoltaic cells [21]. The energy can be harvested at a rate of $100\,mW/cm^2$ in the daytime, but the dependency of solar energy on the time and weather is a disadvantage. For indoor scenarios, an alternative is indoor light, which is controllable in contrast to solar energy.

## 1.4.4   Electromagnetic Energy

Wireless harvesting for electromagnetic energy is possible. Electromagnetic energy can be divided into two categories: near field and far field [17]. For near field, the applications are electromagnetic induction and magnetic resonance, while for far field, the radio frequency (RF) can be harvested from base station or WiFi routers.

These energy sources have different characteristics. For example, solar energy is available only when it is sunny. Wind energy can only be used when or where it is windy [17]. Hence, it is very important to choose the appropriate energy source. For mobile applications, harvesting energy from ubiquitous RF

signals are more suitable [22].

## 1.5   Electromagnetic Transfer Techniques

These can be separated into two kinds: one is for near-field distances and the other is for far-field applications [23].

Near-field techniques include inductive coupling and magnetic resonance coupling. Inductive coupling occurs between two coils, which are tuned to resonate at the same frequency. The electric power is transferred through the magnetic field between the two coils and the coupling can be increased by placing them together or winding them into coils on a common axis [24]. In magnetic resonance coupling [25], electrical energy is transferred between the transmitter and the receiver by magnetic fields. However, near-field energy transfer has multiple drawbacks; namely, such as the distance of near-field is constrained and the calibration of coils or resonators is hard. Therefore, near-field energy transfer is not suitable for mobile and remote energy charging [15].

On the contrary, far-field techniques can serve devices up to several kilometers away [23]. RF signals are ubiquitous with a frequency range from $3\,\text{kHz}$ to $100\,\text{GHz}$ [15], which can power a large number of devices. For example, when the transmit power is $4\,\text{W}$, the receiver can harvest $5.5\,\mu\text{W}$ at distance $15\,\text{m}$. And when the transmit power is $1.78\,\text{W}$, the receiver at $25\,\text{m}$ away can harvest $2.3\,\mu\text{W}$ energy.

Wireless energy harvesting can be from ambient RF signals or dedicated power transmitters. Urban areas are full of ambient RF sources such as WiFi networks, cellular base stations, TV stations and others. Ambient RF signals are thus free and abundantly available [26], [27]. However, in some places, ambient energy levels are too weak to be harvested. In that case, dedicated power transmitters can enable EH powered wireless devices [28].

Table 1.1 shows the experimental data of RF energy harvested from different sources. It can be observed that source power and the distance between the transmitter and the receiver greatly impact on the energy harvesting rate.

Table 1.1: Experimental RF Energy Harvester data

| Source | Source Power (W) | Frequency (MHz) | Distance (m) | EH Rate ($\mu$W) |
|---|---|---|---|---|
| Isotropic RF transmitter [29] | 1.78 | 868 | 27 | 2 |
| Isotropic RF transmitter [29] | 1.78 | 868 | 25 | 2.3 |
| Isotropic RF transmitter [30] | 4 | 906 | 15 | 5.5 |
| TX91501b Powercaster[31] | 3 | 915 | 6 | 9 |
| TX91501b Powercaster[31] | 1 | 915 | 4 | 1 |

## 1.6  Wireless Energy Transmit Schemes

In RF-based wireless EH networks, transmitting schemes can be distinguished into three protocols [28], and the prototypes are shown in Fig. 1.2:

- Wireless Power Transfer (WPT)

  In the WPT scheme, the power transmitter only transmits power to charge user nodes without any information exchange [32].

- Wireless Powered Communication Network (WPCN)

  In a WPCN protocol, users can be charged by the energy transmitted by an access point (AP) or a power station (PS) in the downlink (DL), and users use the harvested energy to transmit information in the uplink (UL). This protocol is called "harvest-then-transmit" [33].

- Simultaneous Wireless Information and Power Transfer (SWIPT)

  In the SWIPT protocol [34], the AP uses the same waveform to transmit energy and information to users. Due to circuit constraints, several structures are used in SWIPT implementations: time switching, power splitting, and antenna switching.

This thesis will study the performances of WPCNs, i.e., the user harvests energy in the DL and transmit information in the UL by using the harvested
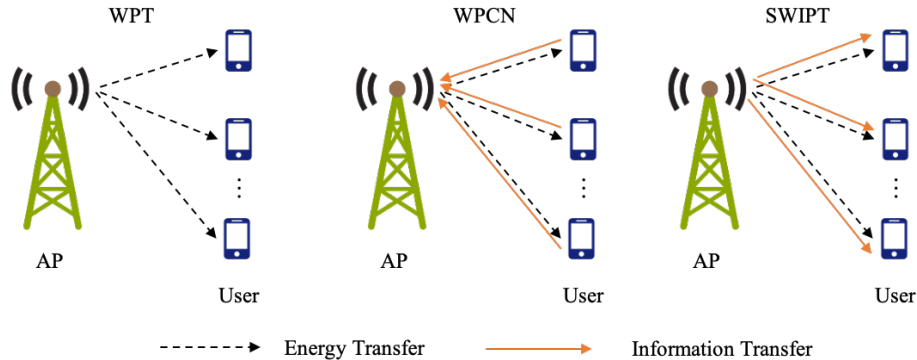
Figure 1.2: EH transmission schemes.

energy.

## 1.7 Motivation and Contributions

Channel state information (CSI) is estimated by at least two ways. First, the receiver estimates the CSI and feeds it back to the transmitter. Second, the transmitter can directly estimate CSI if the channel is reciprocal. But the first method is the most common. In any case, for CSI estimation purposes, pilot symbols are sent periodically [35]. However, many works assume perfect CSI [36]–[38]. However, in practical networks, perfect CSI estimation is difficult even if the channel is quasi-static and even when the interference is small [39]. Channel estimation errors can lead to performance losses, which can be quantified in terms of outage probability, ergodic capacity and diversity gain. Therefore, assuming perfect CSI may predict overoptimistic results. The performance of WPCNs with imperfect CSI has not been characterized widely in the literature. In order to reduce this knowledge gap, this thesis investigates several performance measures (the throughput and bit/symbol error rates) in detail.

In most existing EH papers [33], [37], [40], [41], the linear energy harvester model is assumed. This means that the output power of the energy harvester increases linearly with the input RF signal power. However, in practical EH wireless systems, energy harvesters are made up of nonlinear components including diodes, resistors, capacitors [42]. The experimental data also shows

8

that the output power is a nonlinear function of the input power [43], [44]; that is, a saturation plateau exhibits with high input powers. Clearly, the linear model cannot correctly represent this property. Therefore, a new nonlinear EH model is proposed to provide better characterize the EH system performance.

In this thesis, the performance of two practical scenarios in WPCNs will be evaluated. The contributions of this thesis are listed below:

- Channel estimation errors cause the performance loss. In order to evaluate the impact of channel estimation errors on the performance of a WPCN, this thesis considers a multi-antenna transmitter and a single antenna wireless device with imperfect CSI. The average throughput of delay-limited and delay-tolerant transmission modes are derived for this system. To gain more insight, the asymptotic throughput of both modes are also derived.

- Bit error rate (BER) and symbol error rate (SER) measures the reliability of data communication. In the thesis, the closed-form expressions of average BER and SER are obtained for several modulations to study the impact of imperfect CSI. Since the closed-form expressions are too complicated to observe the relationships between BER/SER and parameters, asymptotic expression for BER and SER are derived.

- The model of energy harvesters impact the level of energy harvested at users, but linear EH model cannot characterize the true value of harvested power in the high transmit power region. In the thesis, a new nonlinear EH model based on the error function is proposed. The parameters of this model can be determined by curve fitting. An asymptotic version of the EH model is also given. A rational model and a linear model are described for comparative purposes.

- To compare the four EH models, a WPCN with a multi-antenna power station, a single-antenna wireless device, and a multi-antenna information receiving station is considered. Average throughput and average

BER are derived for all the EH models. The large antenna regime at the power station is also considered and asymptotic results are obtained.

## 1.8 Outline

The thesis is organized as follows.

In Chapter 2, some background materials necessary for the thesis are presented. The EH models and the concept of high SNR analysis are also described.

In Chapter 3, the performance of a WPCN with imperfect CSI is studied. The system contains a multi-antenna hybrid AP and a single-antenna user. Average throughput, BER, and SER are evaluated in exact and asymptotic form. Numerical results are presented to validate the correctness of analytical expressions.

Chapter 4 studies a WPCN with nonlinear EH models. Average throughput of delay-limited and delay-tolerant mod as well as BER are evaluated. Finally, numerical results are presented for validating analytical results.

Chapter 5 concludes the thesis and shows the future directions.

# Chapter 2

# Background

## 2.1 Small Scale Fading

Small-scale fading refers to the rapid change of signals' amplitude, angle and phase due to the multipath propagation in short time duration or short distance. Therefore, the signal at the receiver may undergo severe fading after vector synthesis, which cannot be ignored. Small-scale fading can be characterized by several mathematical models, two of which are shown below.

**Rayleigh fading**

Rayleigh fading model works best when the transmit signal may be reflected and refracted by buildings or other obstacles during propagation. In this case, line-of-sight (LOS) links are not dominant between the transmitter and the receiver. Rayleigh fading model is especially suitable for urban environments.

According to this model, the magnitude of the signal received at the receiver follows the Rayleigh distribution, and the probability density function (PDF) of the signal power follows the exponential distribution [45]

$$f_\gamma(\gamma) = \frac{1}{\overline{\gamma}} \exp\left(-\frac{\gamma}{\overline{\gamma}}\right), \quad 0 \leq \gamma < \infty, \tag{2.1}$$

where $\overline{\gamma}$ is the average signal-to-noise ratio (SNR).

**Nakagami-$m$ fading**

Nakagami-$m$ fading is a general applicability model which can represent a variety of fadings. When $m = 1$, Rayleigh fading is recovered, and when

11

parameter $m \to \infty$ denotes no fading scenario. With Nakagami-$m$ fading, the PDF of the signal power is given as

$$f_\gamma\left(\gamma\right) = \left(\frac{m}{\bar{\gamma}}\right)^m \frac{\gamma^{m-1}}{\Gamma\left(m\right)} \exp\left(-\frac{m\gamma}{\bar{\gamma}}\right), \quad \gamma \geq 0, \tag{2.2}$$

where parameter $m$ describes the level of fading and covers several fading models.

## 2.2 Energy Harvesting Models

### 2.2.1 Linear Energy Harvesting Model

The linear energy harvesting (EH) model is the most commonly used one in the literature [33], [34], [37], [40], [41], [46], [47]. In this model, the output power of the energy harvester linearly increases as the input power increases as

$$P_L = \mu P_i, \tag{2.3}$$

where $P_i$ is the input power and $\mu$ is the parameter. However, empirical works [44], [48] demonstrate that practical energy harvesters have a saturation plateau when the input power is large enough. Thus, linear model is not accurate in the high input power regime.

### 2.2.2 Piece-wise Linear Model

This model is a simple nonlinear EH model which uses two linear functions in low and high input power region, respectively [49]. The function of input-output power is given as

$$P_{SW} = \begin{cases} \mu P_i, & P_i < P_{th}, \\ P_0, & P_i \geq P_{th}, \end{cases} \tag{2.4}$$

where $P_{th}$ denotes the saturation threshold and $P_0$ is the saturation power. This model captures the saturation behavior, but may not fully match experiment data.

### 2.2.3 Rational Model

Rational EH model was first proposed in [50]. It consists of seven parameters, which are determined by curve fitting with measured data. According to this model, the input-output power can be written as a rational function

$$P_R = \frac{p_2 P_i^3 + p_1 P_i^2 + p_0 P_i}{q_3 P_i^3 + q_2 P_i^2 + q_1 P_i + q_0}, \tag{2.5}$$

where $p_0, p_1, p_2, q_0, q_1, q_2,$ and $q_3$ are parameters. They are different for different harvesters. Although this nonlinear model captures the character of experiment data, due to the presence of seven parameters, this model is not analytically tractable. Due to this reason, a simpler rational model is given in [51]. The output power to this model is

$$P_{RS} = \frac{aP_i + b}{P_i + c} - \frac{b}{c}, \tag{2.6}$$

where $a, b,$ and $c$ are constants obtained by standard curve fitting.

### 2.2.4 Sigmoid Model

Reference [42] proposed the sigmoid model and verified its accuracy with measurement data. The relationship of input-output power is a sigmoid function as

$$P_S = P_{\max} \frac{1 - e^{-uP_i}}{1 + e^{-u(P_i - v)}}, \tag{2.7}$$

where $P_{\max}$ is the maximum harvested power, $P_{\max}, u,$ and $v$ are constant related to the EH circuit. However, this model does not satisfy the sensitivity property; namely, the EH output power drops to zero if the input RF power is below a minimum input power level. To fix this problem, it is modified by [52] as

$$P_{MS} = \left[ \frac{P_{\max}}{\exp(-uP_0 + v)} \left( \frac{1 + \exp(-uP_0 + v)}{1 + \exp(-uP_i + v)} - 1 \right) \right]^+, \tag{2.8}$$

where $P_0$ is a constant.

## 2.3 High SNR Analysis

Typically, closed-form expressions for the analysis of fading channels are complicated so the influence of different parameters on the system is implicit. A

more insightful method is to develop asymptotic or high SNR analysis. For a standard point-to-point communication link subject to small-scale fading, the SNR at the receiver may be represented as $\gamma = X\overline{\gamma}$, where $\overline{\gamma}$ is the unfaded SNR, a constant, and $X$ is a random variable with PDF $f(x)$. $X$ accounts for all the effects of small-scale fading [53]. Suppose the Taylor series of the PDF $f(x)$ near $x = 0$ to be $f(x) = a_0 x^t + a_1 x^{t+1} + \ldots$. It turns out that the asymptotic performance depends on just the first term of the Taylor series and the two parameters $a_0 > 0$ and $t \geq 0$ are critical. First developed in [53], the insight is that as $\overline{\gamma} \to \infty$, the asymptotic performance can be expressed as

$$P_e(\overline{\gamma}) = (G_c\overline{\gamma})^{-G_d}, \tag{2.9}$$

where $G_c$ and $G_d$, which are functions of $a$ and $t$, are called coding gain and diversity gain, respectively. These important, widely-used parameters enable the design and optimization of wireless systems. For instance, from (2.9), we observe that $\log\left[P_e(\overline{\gamma})\right]$ varies linearly with $\log\left[\overline{\gamma}\right]$, which provides direct insights in terms of diversity gain. From (2.9), we can readily see that [54]

$$G_d = \lim_{\overline{\gamma}\to\infty} \frac{-\log P_e(\overline{\gamma})}{\log \overline{\gamma}}.$$

$G_d$ is related to the number of independently fading signal copies between the transmitter and the receiver [55].

Coding gain $G_c$ is measured by the shift of the curve in SNR relative to a benchmark $P_e$ curve of $(\overline{\gamma}^{-G_d})$, which is defined as [53]

$$G_c = \lim_{\overline{\gamma}\to\infty} \left(\overline{\gamma}^{G_d} P_e\right)^{-\frac{1}{G_d}}.$$

This limiting process can be used with any outage or error rate expression to determine the diversity order.

Based on the seminal work in [53], several improvements have been found [56]–[58]. Instead of the single term expansion, [56] considers $f(\beta) = a_0 x^t + a_1 x^{t+1}$, which are the first two terms of the Taylor series, and approximate this as an exponential function. This approach leads to a very highly accurate asymptotic performance expressions, albeit more complicated than those derived based on [53]. A Mellin transform based approach over the asymptotic

expansion of the PDF, given in (2.9), derives a uniform approximation [57] that works for both low and high SNR regimes. Authors in [58] combined dual exponential sum with the asymptotic model in (2.9).

## 2.4 Summary

In this chapter, we briefly introduced the fading channels models, several models of energy harvesters. High SNR analysis is also described, which will be exploited in Chapter 2 for performance analysis.

# Chapter 3

# Wireless Powered Communication Networks with Channel Estimation Errors

## 3.1 Introduction

### 3.1.1 Background and Motivation

Wireless energy harvesting communications may alleviate excess energy use of wireless networks [15], [28], [59]. They exploit the principles of microwave wireless energy transfer and may improve the energy efficiency of battery-constrained wireless nodes. Energy harvesting (EH) is feasible from various sources such as mechanical, solar, and radio-frequency (RF) energy sources. However, solar irradiance is susceptible to weather conditions and time varying. Mechanical motion is hard to predict [60]. In contrast, RF sources not only avoid those issues, but also are ubiquitous. For example, EH amounts of $5.5\,\mu W$ and $2.3\,\mu W$ are feasible at distances $15\,m$ and $25\,m$ from an RF source of $4\,W$ and $1.78\,W$ [61]. Applications of wireless-powered communication networks (WPCNs) include active radio-frequency identification (RFID), real-time location system tags, wireless sensors, and data loggers [13]. Moreover, Powercast has developed commercial WPCNs [31]. They could simplify the charging, servicing and maintenance of battery-needed devices [13], [36], [37], [62].

A key WPCN protocol is called "harvest-then-transmit" [33], where users

harvest energy from the RF signals broadcast by an access-point (AP) in the downlink (DL) and then use the harvested energy to send information to the AP in the uplink (UL). An alternative implementation is to deploy multiple power beacons (PBs), which are dedicated RF power transmitters for the purpose of enabling EH. These concepts have increased the interest in WPCNs, and thus [28] has discussed three different EH modes. The first is pure wireless power transfer (WPT), where an AP or a PB transmits power only to a wireless EH receiver, without any information exchange. The second mode is the WPCN, as described before. The third mode is simultaneous wireless information and power transfer (SWIPT). In SWIPT, a hybrid AP transmits energy and information using the same signal, from which the EH receiver will harvest energy and extract information. This paper focuses on the second mode, namely the WPCN, a prototype of which is shown in Fig. 3.1. This prototype consists of a multiple-antenna hybrid AP and a single-antenna user. The AP can utilize its multiple antennas to focus energy in the direction of the user; energy beamforming is thus common place to increase both wireless power transfer efficiency and data transfer efficiency [28], [36], [37].

### 3.1.2   Performance with Perfect CSI

Before proceeding to the main issue of imperfect CSI, we briefly review a few works on WPCNs with perfect CSI [36], [37], [63]–[65]. The key paper, which is the starting point of our work, is [37]. This work analyzes the average throughput of the same WPCN (Fig. 1) for two transmission modes. It utilizes maximum ratio transmission (MRT) energy beamforming to extend coverage and to maximize the amount of harvested energy. This work also develops asymptotic analyses in the high signal-to-noise ratio (SNR) regime. While [63] derives the outage probability, ergodic capacity, achievable throughput and bit error rate (BER) using Meijer G-function for the generalized $\kappa - \mu$ fading channel. However, this study is limited to single-antenna AP and user. The focus of this paper is to derive unified expressions, which can handle the three classical fading models - namely Rayleigh, Rician and Nakagami-$m$. The

interplay between EH and user cooperation in a WPCN is the focus of [36], which optimizes the energy beamforming vector and time and power allocations. The time correlation between the DL and UL channels is investigated in terms of the BER and achievable rate [64]. In [66], the energy efficiency is maximized by jointly optimizing energy transfer time duration and transmit power. The average throughput of a multiple-input multiple-output (MIMO) WPCN has been studied in [65]. All these works assume the availability of perfect CSI, which is the critical difference from our paper.

### 3.1.3   Performance with Imperfect CSI

CSI is an absolutely critical component of wireless links. On the other hand, in practical systems, perfect CSI is not available and in fact imperfect CSI is the norm [11], [34], [67], [68]. Typically, training (pilot) symbols are sent periodically for CSI estimation purposes [35]. Alternatively, blind and semiblind techniques have also been developed. The impact of CSI estimation errors includes the loss of diversity and capacity gains. To understand this, we can consider a simple wireless link with one transmit antenna and say $N > 1$ receive antennas with maximal ratio combining (MRC) reception. The antenna separation is sufficient to ensure independent fading across them. Now if CSI is perfect, the diversity order of this link is $N$. In contrast, for imperfect CSI, the diversity order collapses to one [69], [70].

Although imperfect CSI for WPCNs is studied in several studies [71]–[80], these works focus on specific application scenarios and associated optimizations. For example, in [71] the EH process is optimized by considering beamforming design, power allocation, antenna selection and time division based on imperfect CSI. On the other hand, how secrecy performance and resource allocation issues are affected by imperfect CSI has also been investigated [72], [73]. The focus of [74] is the capacity of an EH link Rician fading channels for two cases: absence of CSI and partial CSI. Throughput optimization of a massive MIMO WPCN with estimated CSI has also been investigated [75]. The impact of CSI on wireless powered relaying (WPR) systems, a form of WPCNs, has also been studied [76], [77]. The paper [76] investigates the impact of CSI and

18

antenna correlation considering instantaneous or statistical CSI and derives outage probability and ergodic capacity. The focus of [77] is the effect of the non-linear EH process and imperfect CSI. Reference [78] analyzes an EH co-operative communication link for two cases: (a) a single-antenna source with perfect CSI and (b) a multiple-antenna source with imperfect CSI. The uplink scheduling problem for an AP with imperfect CSI has been investigated [79]. The result is a discrete optimization solution of the best transmission schedule. Secrecy throughput optimization of a WPCN with nonlinear EH has been studied in [80]. It considers both perfect and imperfect CSI cases.

Although the aforementioned works consider imperfect CSI, their primary perspective is not that of a comprehensive performance analysis (e.g., deriving outage, capacity and error rates). Instead, they focus on several application domains and optimization. Thus, an analysis of imperfect CSI on the performance of WPCNs has been missing. Thus, this topic is the focus of the present paper.

### 3.1.4 Problem Statement and Contributions

To the best of our knowledge, the performance degradation of the WPCN (Fig.3.1) due to imperfect CSI has thus far not been characterized. This gap in understanding is problematic because, as mentioned before, imperfect CSI can lead to performance losses. To characterize the impact of this problem, we investigate the throughput performances and bit/symbol error rates of several modulations, as well as their high SNR performance of this WPCN with energy beamforming and imperfect CSI. The throughput performance is analyzed for both delay-limited and delay-tolerant modes. These modes correspond to the length of the codewords transmitted by the user. In the delay-limited mode, multiple codewords fit the duration of each transmission block, and thus the AP decodes each codeword as it arrives. In this case, outage probability (OP), the probability that the short-term information transfer rate falls below the fixed transmission rate of the user, serves as a critical measure of the average throughput.

On the other hand, in the delay-tolerant mode, the user can tolerate more

delay and thus can use long codewords compared to the duration of the transmission block. In this case, it is best for the AP to store multiple signal blocks in a buffer and to decode them together. Consequently, the ergodic capacity (EC), which is the long-term average of the instantaneous information transfer rate, is the relevant measure of the system throughput.

The main contributions are summarized as follows:

1. In practical networks, perfect CSI is not available due to estimation errors, feedback delays and other issues [71]. Thus, it is important to include these effects in the analysis of performance. To this end, for a WPCN with imperfect CSI, we derive the PDF and CDF (cumulative distribution function) and moment generating function (MGF) of the received SNR at the AP and the exact close-form throughput expressions for both delay-limited and delay-tolerant modes.

2. BER and SER values quantify the reliability of the network. Thus, we also derive exact close-form expressions for binary phase shift keying (BPSK), binary differential phase shift keying (BDPSK), M-ary phase shift keying (M-PSK), and M-ary quadrature amplitude modulation (M-QAM).

3. As will be seen later, the PDF of the received SNR $f(x)$ contains Bessel functions, which lack a simple Taylor series expansion at $x = 0$. For this reason, the classical asymptotic approach [53] appears intractable here. Thus, we develop a two-step process, exploiting the fact that the received SNR is the product of two random variables (RVs). So we take the expectation over one RV first and simplify the result to yield asymptotic results. By using this general idea, we derive novel, asymptotic (i.e., high-SNR) expressions of throughput, BERs, and SERs. For the delay-tolerant mode, the asymptotic large antenna case and the throughput-optimal EH time in the high SNR regime are also derived.

4. Finally, numerical results and simulations are presented to validate the derived results and to investigate the interplay between the quality of
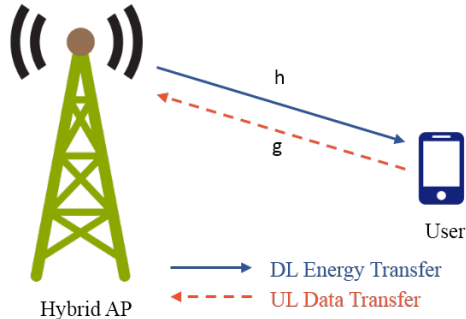
Figure 3.1: System model.

CSI and the EH process. We thus find the large number of antennas eliminates the effects of small-scale fading. We also find that the quality of CSI measured by $\rho$ has more impact on the system performance than the other factors.

In a nutshell, this chapter generalizes the work of [37] to the imperfect CSI case. As well, [37] does not consider the analysis of BER/SER, which is a main part of this chapter.

*Notation:* For random variable $X$, $f_X(\cdot)$ and $F_X(\cdot)$ denote PDF and CDF. Vector $\mathbf{x} \sim \mathcal{CN}(\boldsymbol{\mu}, \boldsymbol{\Sigma})$ denotes a circularly symmetric complex Gaussian vector with mean $\boldsymbol{\mu}$ and covariance matrix $\boldsymbol{\Sigma}$. The special case is the circularly symmetric complex Gaussian RV with mean $\mu$ and variance $\sigma^2$ denoted by $x \sim \mathcal{CN}(\mu, \sigma^2)$. The gamma function $\Gamma(a)$ is given in [81, Eq. (8.310.1)]; $K_\nu(\cdot)$ is the $\nu$-th order modified Bessel function of the second kind [81, Eq. (8.432)]; $G_{pq}^{mn}\left(z \mid \begin{smallmatrix} a_1 \cdots a_p \\ b_1 \cdots b_q \end{smallmatrix}\right)$ denotes the Meijer G-function [81, Eq. (9.301)]; $\psi(\cdot)$ is the Euler psi function [81, Eq. (8.36)]; $x^H$ denotes the transpose and conjugate of $x$; $W_{\lambda,\mu}(\cdot)$ is the Whittaker function, [81, Eq. (9.200)]; $\Psi(a, b; z)$ is the confluent hypergeometric function in [81, Eq. (9.211.4)].

## 3.2 System Model

We first describe the network model in Fig. 3.1, which consists of a single-antenna user and a multiple-antenna hybrid AP. These two are half-duplex nodes. The AP has $N \geq 1$ antennas and uses MRC for signal reception.

The user, without a battery, is powered via the harvest-then-transmit protocol [37]. Thus, the energy transfer channel, i.e., the AP-to-user channel, is denoted as $\mathbf{h} = [h_1, \ldots, h_k, \ldots, h_N]^T \in \mathbb{C}^{N \times 1}$, and the data transfer channel, i.e., user-to-AP channel, is denoted as $\mathbf{g} = [g_1, \ldots, g_k, \ldots, g_N]^T \in \mathbb{C}^{N \times 1}$. The channel coefficients $h_k, g_k \, \forall k \in [1, N]$ are independent and identically distributed (i.i.d.) circularly symmetric complex Gaussian random variables with zero-mean and unit-variance, i.e., $h_k, g_k \sim \mathcal{CN}(0, 1)$. Equivalently, the channel coefficient magnitudes $|h_k|$ and $|g_k|$ ($k = 1, \ldots, N$) are distributed with the Rayleigh PDF, i.e., $f(x) = 2xe^{-x^2}, 0 \leq x < \infty$.

Let channel estimates of the true channels $\mathbf{h}$ and $\mathbf{g}$ be denoted as $\hat{\mathbf{h}}$ and $\hat{\mathbf{g}}$, respectively. AP gets them via suitable pilot-assisted channel estimation techniques. Thus, these estimate will have both noise and correlative components. These are represented in the following model. For any true channel $\mathbf{x} \in \{\mathbf{h}, \mathbf{g}\}$, the channel estimate $\hat{\mathbf{x}} \in \{\hat{\mathbf{h}}, \hat{\mathbf{g}}\}$ is related as [34]

$$\hat{\mathbf{x}} = \rho \mathbf{x} + \sqrt{1 - \rho^2} \tilde{\mathbf{n}}, \tag{3.1}$$

where $0 \leq \rho \leq 1$ is the correlation coefficient between a true channel and its estimate, and $\tilde{\mathbf{n}} \in \mathbb{C}^{N \times 1}$ is an $N$-dimensional noise vector of i.i.d. $\mathcal{CN}(0, 1)$ entries. The quality of CSI is indicated by the value of $\rho$. While $\rho = 1$ and $\rho = 0$ cases indicate perfect and worst-case (noisy) channel estimation scenarios. The range $0 \leq \rho < 1$ will be the imperfect CSI case. The exact value of $\rho$ in practice is a function of pilot symbols and their power. For convenience, we assume both UL and DL estimations are characterized by the same value of $\rho$. It is worth mentioning that the model (3.1) also represents the case of outdated CSI as well. In this case, the well-known Jake's model suggests that $\rho = J_0(2\pi f_d \tau)$, where $J_0(x)$ denotes the zeroth order Bessel function of first kind and $f_d$ indicates the maximum Doppler frequency and $\tau$ is the time delay. Thus, all these factors can be investigated in conjunction with the EH process, a task that is left for future research.

Given these details of channel estimation, we next turn to specify the amount of harvested energy at the AP. Without loss of generality, we assume a unit transmission block ($T = 1$). Thus, for $\tau$ duration, where $\tau \in (0, 1)$, the

AP transmits RF power at level $P$ in the DL and the user harvests it. The user then transmits data in the UL for $(1 - \tau)$ duration. This cycle repeats again in the next block and so on. We assume that the AP processes the transmit power symbols with a linear precoder to achieve energy beamforming. Energy beamforming is the process of a highly directional transmission with high-gain antennas to focus energy beams toward the user. It thus maximizes the harvested energy at the user. To achieve this, the transmit signals at different antennas are carefully weighted (precoding) to achieve constructive superposition at the user. The precoding vector is computed by the AP, which requires accurate CSI. In this work, we assume MRT energy beamforming, which is optimal for the single-cell case[28]. Thus, the AP transmit signal is $\sqrt{P}\mathbf{f}$ where the precoding vector $\mathbf{f}$ is chosen subject to the constraint $||\mathbf{f}|| = 1$. The AP will utilize imperfect CSI to compute $\mathbf{f} = \frac{\hat{\mathbf{h}}}{|\hat{\mathbf{h}}|}$. Thus, the user's total harvested energy is $E_h = \eta\tau|\sqrt{P}\mathbf{f}^H\mathbf{h}|^2 = \eta\tau P\frac{||\hat{\mathbf{h}}^H\mathbf{h}||^2}{\hat{\mathbf{h}}^H\hat{\mathbf{h}}}$ [71, Eq. (2)], where $\eta$ is the energy conversion efficiency. In practice, the maximum conversion efficiency depends on the specific technologies; for example, it is about 48% with a Schottky diode and around 56% with CMOS (complementary metal-oxide-semiconductor) devices [82].

By using the harvested energy, the user transmits data signals to the AP in the UL with power $P_s$ that is given as

$$P_s = \frac{E_h}{1 - \tau} = \frac{\tau\eta P}{1 - \tau}\frac{||\hat{\mathbf{h}}^H\mathbf{h}||^2}{\hat{\mathbf{h}}^H\hat{\mathbf{h}}}. \tag{3.2}$$

Note that if perfect CSI is available, then $\hat{\mathbf{h}} = \mathbf{h}$. The transmit power of the user then becomes $P_s = \frac{\tau\eta P}{1-\tau}||\mathbf{h}||^2$, which is consistent with previous results [37]. The received signal at the AP is $y_A = \sqrt{P_s}\mathbf{g}s + \mathbf{n}$, where $s$ is the energy-normalized data symbol and $\mathbf{n}$ is the complex additive white Gaussian noise (AWGN) term, $\mathbf{n} \sim \mathcal{CN}(0, 1)$. The AP uses MRC type reception to maximize the received SNR; with MRC, the received signal is multiplied by $\hat{\mathbf{g}}^H$. This multiplication will affect both the signal term and noise term in $y_A$. But the ratio of the powers of these two terms gets scaled by $\frac{||\hat{\mathbf{g}}^H\mathbf{g}||^2}{\hat{\mathbf{g}}^H\hat{\mathbf{g}}}$. The SNR at the

AP can thus be derived as

$$\gamma_A = \frac{\tau \eta P}{1 - \tau} \frac{1}{\sigma^2} \frac{||\hat{\mathbf{h}}^H \mathbf{h}||^2}{\hat{\mathbf{h}}^H \hat{\mathbf{h}}} \frac{||\hat{\mathbf{g}}^H \mathbf{g}||^2}{\hat{\mathbf{g}}^H \hat{\mathbf{g}}} = c\overline{\gamma}XY, \qquad (3.3)$$

where $\sigma^2$ is the power of noise, $\overline{\gamma} = \frac{P}{\sigma^2}$, $c = \frac{\tau \eta}{1-\tau}$, $X = \frac{||\hat{\mathbf{h}}^H \mathbf{h}||^2}{\hat{\mathbf{h}}^H \hat{\mathbf{h}}}$, and $Y = \frac{||\hat{\mathbf{g}}^H \mathbf{g}||^2}{\hat{\mathbf{g}}^H \hat{\mathbf{g}}}$. It is clear that both $X$ and $Y$ have the identical statistical distribution. These ratios arise in the performance evaluation of MRC diversity reception with imperfect CSI, and their distribution was derived in a classical paper [69].

## 3.3 Statistical Distribution Results

This section provides necessary statistical distributions for the use in subsequent derivations throughout the paper.

### 3.3.1 The Distribution of Received SNR, $\gamma_A$

**Lemma 1.** *Since $\gamma_A = c\overline{\gamma}XY$, the PDF of $\gamma_A$ is the product of a constant and the RV $Z = XY$. Therefore, the PDF can be given by*

$$f_{\gamma_A}(z) = \sum_{n=1}^{N} \sum_{m=1}^{N} \frac{2B(m,n) \left(\frac{z}{c\overline{\gamma}}\right)^{\alpha(m,n)}}{c\overline{\gamma}} K_{n-m}\left(2\sqrt{\frac{z}{c\overline{\gamma}}}\right), \qquad (3.4)$$

*where $N$ is the number of antennas at the AP, $\alpha(m,n) = \frac{n+m-2}{2}$, $A(n) = \binom{N-1}{n-1}\frac{(1-\rho^2)^{N-n}}{\Gamma(n)}\rho^{2(n-1)}$ and $B(m,n) \triangleq A(n)A(m)$.*

*Proof.* The PDF of $X$ was derived in [69]

$$f_X(x) = \sum_{n=1}^{N} A(n)x^{n-1}e^{-x}, \quad 0 \le x < \infty. \qquad (3.5)$$

As channels are i.i.d., the PDF of $Y$, $f_Y(y)$, can also be given as (3.5).

Then the PDF of the product of two non-negative RVs $X$ and $Y$, denoted as $Z = XY$, can be derived as

$$
\begin{aligned}
f_Z(z) &\overset{(a)}{=} \int_0^\infty \frac{1}{\omega} f_X(\omega) f_Y\left(\frac{z}{\omega}\right) d\omega \\
&\overset{(b)}{=} \sum_{n=1}^{N} \sum_{m=1}^{N} \frac{B(m,n)}{z^{-(m-1)}} \int_0^\infty \omega^{n-m-1} e^{-\omega - \frac{z}{\omega}} d\omega \\
&\overset{(c)}{=} \sum_{n=1}^{N} \sum_{m=1}^{N} 2B(m,n) z^{\frac{n+m-2}{2}} K_{n-m}\left(2\sqrt{z}\right),
\end{aligned}
\qquad (3.6)
$$

24

where (a) is the formula to find the PDF of the product of two RVs; (b) is obtained by (3.5); (c) is due to [81, Eq. (3.471.9)].

Since $\gamma_A = c\overline{\gamma}Z$, the PDF of $\gamma_A$ can be derived as (3.4). ∎

**Corollary 1.** *The CDF of $\gamma_A$ is given by*

$$
F_{\gamma_A}(x) = \sum_{n=1}^{N}\sum_{m=1}^{N} \frac{B(m,n)}{(c\overline{\gamma})^{(\alpha(m,n)+1)}} x^{\alpha(m,n)+1} \tag{3.7}
$$
$$
\cdot G_{1,3}^{2,1}\left(\frac{x}{c\overline{\gamma}} \,\middle|\, \begin{array}{c} -\alpha(m,n) \\ \frac{n-m}{2}, -\frac{n-m}{2}, -\alpha(m,n)-1 \end{array}\right).
$$

*Proof.*

$$
F_{\gamma_A}(x) \overset{(a)}{=} \sum_{n=1}^{N}\sum_{m=1}^{N} \frac{2B(m,n)}{c\overline{\gamma}}
$$
$$
\cdot \int_0^x \left(\frac{z}{c\overline{\gamma}}\right)^{\alpha(m,n)} K_{n-m}\left(2\sqrt{\frac{z}{c\overline{\gamma}}}\right) dz
$$
$$
\overset{(b)}{=} \sum_{n=1}^{N}\sum_{m=1}^{N} \frac{B(m,n)}{(c\overline{\gamma})^{(\alpha(m,n)+1)}} x^{\alpha(m,n)+1} \tag{3.8}
$$
$$
\cdot G_{1,3}^{2,1}\left(\frac{x}{c\overline{\gamma}} \,\middle|\, \begin{array}{c} -\alpha(m,n) \\ \frac{n-m}{2}, \frac{m-n}{2}, -\alpha(m,n)-1 \end{array}\right),
$$

where (a) follows from the definition of CDF; (b) is obtained by using the equation which expresses $K_v(\cdot)$ in terms of $G_{p,q}^{m,n}[\cdot]$ in [37] and [81, Eq. (9.31.5)]. ∎

### 3.3.2 Moments-Generating Function

**Lemma 2.** *The MGF of $\gamma_A$ can be given by*

$$
M_{\gamma_A}(t) = \sum_{n=1}^{N}\sum_{m=1}^{N} B(m,n)\left(\frac{1}{c\overline{\gamma}}\right)^{\alpha(m,n)+\frac{1}{2}} \tag{3.9}
$$
$$
\cdot \Gamma(n)\Gamma(m) e^{\frac{1}{2tc\overline{\gamma}}} t^{-\frac{1}{2}-\alpha(m,n)} W_{-\frac{1}{2}-\alpha(m,n),\frac{n-m}{2}}\left(\frac{1}{tc\overline{\gamma}}\right).
$$

*Proof.* The MGF is defined as $M_{\gamma_A}(t) = \mathbb{E}\left[e^{-t\gamma_A}\right]$. By substituting (3.4) in

this definition, we find

$$
M_{\gamma_A}(t) = \int_0^\infty e^{-ty} f_{\gamma_A}(y)\, dy
$$

$$
\overset{(a)}{=} \sum_{n=1}^N \sum_{m=1}^N \frac{2B(m,n)}{c\overline{\gamma}} \left(\frac{1}{c\overline{\gamma}}\right)^{\alpha(m,n)} \tag{3.10}
$$

$$
\cdot \int_0^\infty e^{-ty} y^{\alpha(m,n)} K_{n-m}\left(2\sqrt{\frac{1}{c\overline{\gamma}}y}\right) dy,
$$

where (a) follows by using the PDF of $\gamma_A$; (10) is then obtained by applying [81, Eq. (6.643.3)]. ∎

**Corollary 2.** *Since the MGF in Lemma 2 is a complicated expression, the effect of different parameters on the MGF is hard to see directly. To alleviate this issue, we derive the asymptotic (e.g., $\overline{\gamma} \to \infty$) MGF as*

$$
M_{\gamma_A}^{asy}(t) \approx \sum_{m=1}^N \frac{B(m,1)}{tc\overline{\gamma}} \left[\sum_{k=1}^{m-1} \Gamma(k) \left(-\frac{1}{tc\overline{\gamma}}\right)^{m-1-k}\right.
$$

$$
\left. + (-1)^{m-2} e^{\frac{1}{tc\overline{\gamma}}} \left(\frac{1}{tc\overline{\gamma}}\right)^{m-1} E_i\left(-\frac{1}{tc\overline{\gamma}}\right)\right], \tag{3.11}
$$

*where $E_i(\cdot)$ is the exponential integral function [81, Eq. (8.211.1)].*

*Proof.* Let us revisit the definition of the MGF; $M_{\gamma_A}(t) = \mathbb{E}\left[e^{-t\gamma_A}\right]$. Since $\gamma_A$ is a product of $X$ and $Y$, we first take the expectation of MGF over $X$. Thus, the MGF conditional on $Y$, denoted as $M_{\gamma_A|Y}(t)$, is given by

$$
M_{\gamma_A|Y}(t) = \mathbb{E}\left[e^{-tc\overline{\gamma}XY}\right]
$$

$$
= \sum_{n=1}^N \frac{A(n)\Gamma(n)}{(1+tc\overline{\gamma}Y)^n}. \tag{3.12}
$$

This expression (13) is derived by taking the expectation over the PDF of $X$, which is given by (6).

The next step is to take the expectation over $Y$, which yields

$$
M_{\gamma_A}(t) = \sum_{n=1}^N \sum_{m=1}^N B(m,n)\Gamma(n) \int_0^\infty \frac{y^{m-1}e^{-y}}{(1+tc\overline{\gamma}y)^n}\, dy. \tag{3.13}
$$

We next note that (3.13) has the series sum over $n$ and $m$. If we expand the series over different $n$ values, when $\overline{\gamma} \to \infty$, the integrals for which $n \geq 2$

26

can be negligible compared to the one for $n = 1$. For this reason, (3.13) can be fairly accurately approximated as follows:

$$M_{\gamma_A}^{asy}(t) \approx \sum_{m=1}^{N} B(m,1) \int_0^\infty \frac{y^{m-1}e^{-y}}{1+tc\overline{\gamma}y}dy,$$

$$\overset{(a)}{=} \sum_{m=1}^{N} \frac{B(m,1)}{tc\overline{\gamma}} \left[ \sum_{k=1}^{m-1} \Gamma(k) \left( -\frac{1}{tc\overline{\gamma}} \right)^{m-1-k} \right. \tag{3.14}$$

$$\left. + (-1)^{m-2} e^{\frac{1}{tc\overline{\gamma}}} \left( \frac{1}{tc\overline{\gamma}} \right)^{m-1} E_i \left( -\frac{1}{tc\overline{\gamma}} \right) \right],$$

where (a) is derived by using [81, Eq. (3.353.5)]. ∎

While the asymptotic MGF of $\gamma_A$ given in (3.14) is fairly simplified compared to the exact one (3.9), even simper version is possible. There are two cases: imperfect CSI and perfect CSI. These are given in the next corollary.

**Corollary 3.** *The asymptotic result in (3.14) can be further simplified for the case of imperfect CSI as*

$$M_{\gamma_A}^{asy}(t) \approx \left( 1 - \rho^2 \right)^{2(N-1)} \frac{[\ln(ct\overline{\gamma}) - \gamma_{EM}]}{ct\overline{\gamma}}, 0 \le \rho < 1, \tag{3.15}$$

*where $\gamma_{EM}$ is the Euler-Mascheroni constant. If perfect CSI is available, then the MGF is approximately*

$$M_{\gamma_A}^{asy}(t) \approx (tc\overline{\gamma})^{-N} \Psi \left( N, 1; \frac{1}{tc\overline{\gamma}} \right), \quad \rho = 1, \tag{3.16}$$

*where $\Psi(a, b; z)$ is known as Tricomi's confluent hypergeometric function or the confluent hypergeometric function of the second kind [81, Eq. (9.211.4)].*

*Proof.* For the imperfect CSI case, when $0 \le \rho < 1$, in (3.13), the dominant part is the one with $n = 1$ and $m = 1$. Therefore, we can consider just that term of (3.13) as

$$M_{\gamma_A}^{asy}(t) = \left( 1 - \rho^2 \right)^{2(N-1)} \int_0^\infty \frac{e^{-y}}{1+xy}dy$$

$$\overset{(a)}{=} \left( 1 - \rho^2 \right)^{2(N-1)} \frac{e^{\frac{1}{x}}\Gamma\left(0, \frac{1}{x}\right)}{x}, \tag{3.17}$$

27

where $x = ct\overline{\gamma}$ and $\Gamma(s, x)$ is upper incomplete gamma function [81, Eq. (8.350.2)].
Let $U = \frac{1}{x} e^{\frac{1}{x}} \Gamma\left(0, \frac{1}{x}\right)$. By using the series expansion of $U$ at $x = \infty$, we can
show that

$$U = \frac{-\gamma_{EM} + \ln(x)}{x} + O\left(\frac{1}{x^2}\right).$$

When $\overline{\gamma} \to \infty$, we have $\frac{1}{x} \to 0$. Therefore, $U$ is approximated well by the first
term on the right. We thus find

$$M_{\gamma_A}^{asy}(t) = \frac{(1 - \rho^2)^{2(N-1)} \left[\ln(ct\overline{\gamma}) - \gamma_{EM}\right]}{(ct\overline{\gamma})} + O\left(\frac{1}{\overline{\gamma}^2}\right). \qquad (3.18)$$

For the case of perfect CSI , where $\rho = 1$, the coefficient $A(n)$ is zero for
all $n$, except for $n = N$. Therefore $B(m, n)$ exists only when $m = n = N$. So
when $\rho = 1$, the MGF may be expressed as

$$\begin{aligned} M_{\gamma_A}^{asy}(t) &= \frac{1}{\Gamma(N)} \int_0^\infty \frac{y^{N-1} e^{-y}}{(1 + tc\overline{\gamma}y)^N} dy \\ &\overset{(a)}{=} (tc\overline{\gamma})^{-N} \Psi\left(N, 1; \frac{1}{tc\overline{\gamma}}\right), \end{aligned} \qquad (3.19)$$

where (a) is obtained by [81, Eq. (9.211.4)]. ∎

Thus far, we have covered the basic distributional results. Next, we will
derive the SNR for the large antenna regime $(N \to \infty)$.

### 3.3.3   SNR for the Large Antenna Case

The following corollary finds the deterministic limit of the SNR as the number
of antennas becomes extremely large. This result is essential for the through-
put analysis of the delay-tolerant mode.

**Corollary 4.** *In this case, we consider the number of AP antenna increases
without limitation with a fixed $\overline{\gamma}$. Then $\gamma_A$ can be derived as*

$$\gamma_A \approx \frac{\tau\eta}{1 - \tau} \overline{\gamma} \rho^4 N^2. \qquad (3.20)$$

*It is observed from (3.20), the effect of small-scale fading has vanished when
the number of AP antenna is very large. This effect is known as channel hard-
ening due to the impact of large scale spatial diversity [83]. Note that $\gamma_A$ also
increases with the increment of energy conversion efficiency $\eta$, $\overline{\gamma}$, correlation
coefficient $\rho$ and the number AP of antennas.*

28

*Proof.* The channel coefficients are i.i.d. circularly symmetric complex Gaussian RVs with zero-mean and unit-variance, so $\hat{\mathbf{h}} \sim \mathcal{CN}(0, I)$.

$$
\begin{aligned}
\frac{\hat{\mathbf{h}}^H \mathbf{h}}{N} &\overset{(a)}{=} \frac{1}{N}\left(\rho\mathbf{h} + \sqrt{1-\rho^2}\tilde{\mathbf{n}}\right)^H \mathbf{h} \\
&\overset{(b)}{=} \frac{\rho\mathbf{h}^H\mathbf{h}}{N} + \frac{\sqrt{1-\rho^2}\tilde{\mathbf{n}}^H\mathbf{h}}{N} \\
&\overset{(c)}{\approx} \rho,
\end{aligned}
\tag{3.21}
$$

where in step (a), we substitute the definition of $\hat{\mathbf{h}}$ (3.1) in $\hat{\mathbf{h}}^H\mathbf{h}$. Step (c) follows from the law of large numbers, $\frac{\mathbf{h}^H\mathbf{h}}{N} \overset{a.s.}{\longrightarrow} 1$, as $N \to \infty$ [84, Eq. (7.14)], [84, Eq. (7.15)]. Similarly, $\frac{\hat{\mathbf{g}}^H\mathbf{g}}{N} \overset{a.s.}{\longrightarrow} \rho$, where $\overset{a.s.}{\longrightarrow}$ denotes the almost sure convergence.

So we can obtain $X = \frac{\|\hat{\mathbf{h}}^H\mathbf{h}\|^2}{\hat{\mathbf{h}}^H\hat{\mathbf{h}}} \overset{a.s.}{\longrightarrow} \rho^2 N$ and $Y = \frac{\|\hat{\mathbf{g}}^H\mathbf{g}\|^2}{\hat{\mathbf{g}}^H\hat{\mathbf{g}}} \overset{a.s.}{\longrightarrow} \rho^2 N$ . Therefore, $\gamma_A \overset{a.s.}{\longrightarrow} \frac{\tau\eta}{1-\tau}\overline{\gamma}\rho^4 N^2$. ∎

## 3.4 Average Throughput Analysis

In this section, we evaluate the average throughput performance of the system model (Section 4.3) We consider both delay-limited mode and delay-tolerant mode. The performance metrics OP and EC are analyzed for these modes. Moreover, we analyze the asymptotic performance at high SNR regime to gain more insights.

### 3.4.1 Delay-Limited Transmission Mode

**Exact Throughput Analysis**

In this section, we consider the delay-limited case, where the AP decodes the received signals one codeword at a time. Therefore, the throughput is now measured by the OP, which is the probability that the instantaneous channel capacity falls below the fixed rate $R$ bits/s/Hz, where $R$ is the fixed transmission rate of the user. The OP is thus given by

$$
P_{out} = \Pr\left(\log_2\left(1 + \gamma_A\right) < R\right) = F_{\gamma_A}\left(\gamma_{\text{th}}\right),
\tag{3.22}
$$

where $\gamma_{\text{th}} = 2^R - 1$ and $F_{\gamma_A}(y)$ is the CDF of $\gamma_A$ given in (3.7). The user transmits for an effective communication time fraction $(1 - \tau)$ during the each

harvest and transmit cycle. Therefore, the average throughput of the delay-limited transmission mode in bits/s/Hz is

$$
\begin{aligned}
R_{DL} &= \left(1 - P_{out}\right)\left(1 - \tau\right)R \\
&= R^* \left[ 1 - \sum_{n=1}^{N}\sum_{m=1}^{N} \frac{B\left(m,n\right)}{\left(c\overline{\gamma}\right)^{\left(\alpha(m,n)+1\right)}} \gamma_{\text{th}}{}^{\alpha(m,n)+1} \right. \\
&\quad \left. \cdot G_{1,3}^{2,1}\left( \frac{\gamma_{\text{th}}}{c\overline{\gamma}} \left| \begin{array}{c} -\alpha(m,n) \\ \frac{n-m}{2}, \frac{m-n}{2}, -\alpha(m,n)-1 \end{array} \right. \right) \right],
\end{aligned}
\tag{3.23}
$$

where $R^* = \left(1 - \tau\right)R$.

Although the throughput expression (3.23) is closed form, it consists of the Meijer G-function, which does not directly reveal specific relationships between the throughput and the parameters $\rho$, $\tau$, and $\overline{\gamma}$. That motivates the asymptotic analysis.

**Asymptotic Throughput Analysis**

In order to gain a simpler result, we derive the asymptotic throughput.

**Proposition 1.** *When $\overline{\gamma} \to \infty$, the asymptotic throughput in bits/s/Hz is given by*

$$
R_{DL} = R^* \left[ 1 - 2\sum_{n=1}^{N}\sum_{m=1}^{N} B\left(m,n\right) \Delta^{\frac{m+n}{2}} K_{n-m}\left(2\sqrt{\Delta}\right) \right],
\tag{3.24}
$$

*where $\Delta = \frac{\gamma_{th}(1-\tau)}{\tau\eta\overline{\gamma}}$. And $\Delta^{\frac{m+n}{2}} K_{n-m}\left(2\sqrt{\Delta}\right)$ is a monotonically increasing function with the increasing of $\Delta$. Therefore, the throughput is improved by increasing the SNR $\overline{\gamma}$, energy conversion efficiency $\eta$, correlation coefficient $\rho$ or decreasing the threshold $\gamma_{th}$.*

*Proof.* See Appendix A.1. ∎

However, the asymptotic throughput in Proposition 1 can be further simplified. To this end, we consider two cases: namely imperfect CSI ($0 \le \rho < 1$) and perfect CSI ($\rho = 1$).

**Proposition 2.** *The asymptotic throughput (3.24) can be further written as*

$$
R_{DL} \approx
\begin{cases}
R^* \left[ 1 - \left(1 - \rho^2\right)^{2(N-1)} \left( \ln\left(\frac{c\bar{\gamma}}{\gamma_{th}}\right) - 2\gamma_{EM} \right) \frac{\gamma_{th}}{c\bar{\gamma}} \right], \\
\qquad\qquad\qquad\qquad\qquad\qquad\qquad 0 \le \rho < 1, \\
R^* \left[ 1 - \frac{1}{\Gamma^2(N)} \left( \ln\left(\frac{c\bar{\gamma}}{\gamma_{th}}\right) - 2\gamma_{EM} \right) \left(\frac{\gamma_{th}}{c\bar{\gamma}}\right)^N \right], \\
\qquad\qquad\qquad\qquad\qquad\qquad\qquad \rho = 1.
\end{cases}
\tag{3.25}
$$

*From (3.25), we directly observe that the throughput may be increased by increasing energy conversion efficiency $\eta$ and SNR at the AP.*

*Proof.* See Appendix A.3. ■

**Remark 1.** *When $\rho = 0$, namely, the user and the AP cannot obtain CSI. The average throughput then is $R^* \left[ 1 - \left( \ln\left(\frac{c\bar{\gamma}}{\gamma_{th}}\right) - 2\gamma_{EM} \right) \frac{\gamma_{th}}{c\bar{\gamma}} \right]$. For the case of perfect CSI, the average throughput will converge to the ceiling value $R^*$ when either the number of AP antennas or the AP transmit power increases without limit. The effect of small-scale fading between the AP and the user vanishes under this scenario. Furthermore, from Section 2.3, the diversity order using OP can be obtained. For the case of imperfect CSI, the diversity order is given as $G_d = \lim_{\bar{\gamma} \to \infty} \frac{-\log P_{out}}{\log \bar{\gamma}} = 1$. In contrast, for the case of perfect CSI, the diversity order can be derived as $G_d = \lim_{\bar{\gamma} \to \infty} \frac{-\log P_{out}}{\log \bar{\gamma}} = N$.*

**Remark 2.** *Here we prove that the analytical results of [37] are special case of ours. The paper [37] studies the same system model as ours but assumes perfect CSI. Therefore, in our paper, when the correlation coefficient $\rho = 1$ (perfect CSI), $B(m, n) = 0$ for all $m$ and $n$ except for $B(N, N) = \frac{1}{\Gamma(N)\Gamma(N)}$. Step (a) of (A.3) is reduced to*

$$
\begin{aligned}
P_{out} &= \frac{1}{\Gamma(N)} \int_0^\infty \left[ 1 - e^{-\frac{\Delta}{y}} \sum_{l=0}^{n-1} \left(\frac{\Delta}{y}\right)^l \frac{1}{l!} \right] y^{m-1} e^{-y} dy \\
&= 1 - 2 \sum_{l=0}^{N-1} \frac{1}{l!\Gamma(N)} \Delta^{\frac{N+l}{2}} K_{N-l}\left(2\sqrt{\Delta}\right),
\end{aligned}
\tag{3.26}
$$

*which is equivalent to [37, Eq. (4)].*

*On the other hand, [65] investigates a MIMO WPCN system with perfect CSI. The SNR in [65, Eq. (8)] is a product of two independent Chi-square variables. In contrast, in our paper, the SNR (3.3) is the product of two weighted sums of Chi-square RVs if $\rho \neq 1$. But for $\rho = 1$, the SNR (3.3) is the product of two Chi-square RVs. Thus, the results in [65] for the case of $M = 1$ are equivalent to our results for $\rho = 1$.*

*The OP in [65, Eq. (12)] is given as*

$$
\begin{aligned}
F_\gamma\left(\gamma_{th}\right) = 1 - 2 \sum_{i=1}^{\min(N,M)} \sum_{j=|N-M|}^{(N+M)i-2i^2} \sum_{k=0}^{j} \frac{i^k d(i,j)}{k!} \left(\frac{\gamma_{th}}{D}\right)^k \\
\cdot \sum_{l=1}^{\min(N,M)} \sum_{m=|N-M|}^{(N+M)l-2l^2} \frac{l^k d(l,m)}{m!} \left(\frac{il\gamma_{th}}{D}\right)^{\frac{m-k+1}{2}} \\
\cdot K_{m-k+1}\left(2\sqrt{\frac{il\gamma_{th}}{D}}\right),
\end{aligned}
\tag{3.27}
$$

*where $N$ is the number of the AP antenna and $M$ is the number of the user terminal antenna. $d(i,j) = \frac{j!}{i^{j+1}\left[\prod_{i=1}^{M}(M-1)!(N-i)!\right]}$ and $D = \frac{\eta\tau\sigma^2}{(1-\tau)Pd_1^T}$. Here, we assume the distance between the AP and the user terminal $d_1^T = 1$.*

*Let $M = 1$, then we have $\min(N, M) = 1$, $j = m = N-1$, $(N+M)i-2i^2 = (N+M)l - 2l^2 = N - 1$, $d(i,j) = d(l,m) = d(1, N-1) = 1$. (3.27) then reduces to*

$$
F_\gamma\left(\gamma_{th}\right) = 1 - 2 \sum_{k=0}^{N-1} \frac{1}{k!\Gamma(N)} \left(\frac{\gamma_{th}}{D}\right)^{\frac{N+k}{2}} K_{N-k}\left(2\sqrt{\frac{\gamma_{th}}{D}}\right).
\tag{3.28}
$$

*The OP (3.27), is identical to OP given in (3.7) in our paper, which is (3.26) as well, when $\rho = 1$.*

*In our notation, $\Delta = \frac{\gamma_{th}(1-\tau)P}{\tau\eta\sigma^2}$, which is equivalent to $\Delta = \frac{\gamma_{th}}{D}$. Therefore, (3.28) is identical to (3.26).*

## 3.4.2 Delay-Tolerant Transmission Mode

### Exact Throughput Analysis

In this mode, as mentioned before, a large delay is tolerable for decoding the stored signals together. Thus, the throughput is related to the ergodic capacity.

However, the user transmits data for time fraction $(1 - \tau)$ only in each cycle. Therefore, the average throughput is the product of ergodic capacity and the effective data transmit time. Thus, we find the throughput in bits/s/Hz as

$$
\begin{aligned}
R_{DT} &= (1 - \tau) \int_0^\infty \log_2 (1 + z) \, f_{\gamma_A} (z) \, dz \\
&\overset{(a)}{=} (1 - \tau) \sum_{n=1}^N \sum_{m=1}^N \frac{2B(m,n)}{c\overline{\gamma}} \\
&\quad \cdot \int_0^\infty \frac{\ln(1+z)}{\ln 2} \left( \frac{z}{c\overline{\gamma}} \right)^{\alpha(m,n)} K_{n-m} \left( 2\sqrt{\frac{z}{c\overline{\gamma}}} \right) dz \\
&\overset{(b)}{=} (1 - \tau) \sum_{n=1}^N \sum_{m=1}^N \frac{B(m,n)}{c\overline{\gamma} \ln 2} \\
&\quad \cdot G_{2,4}^{4,1} \left( \frac{1}{c\overline{\gamma}} \, \middle| \, \begin{matrix} -1, 0 \\ -1, -1, \frac{n-m}{2} + \alpha(m,n), \frac{m-n}{2} + \alpha(m,n) \end{matrix} \right),
\end{aligned}
$$
(3.29)

where (a) follows by the use of PDF (3.4); to derive (b), we express the term $\ln(1+x)$ and $x^a K_v(x)$ in Meijer G-function [85] and then use [81, Eq. (7.811.1)].

**Remark 3.** *In our paper, when channel estimation is perfect , i.e. $\rho = 1$, $\alpha(M, N) = N - 1$ and $B(m,n) = 0$ for all $m$ and $n$ except for $B(N,N) = \frac{1}{\Gamma(N)\Gamma(N)}$. EC is then written as*

$$
C = \frac{(1 - \tau) P G_{2,4}^{4,1} \left( \frac{(1-\tau)P}{\eta\tau\sigma^2} \, \middle| \, \begin{matrix} -1, 0 \\ -1, -1, N-1, N-1 \end{matrix} \right)}{\Gamma(N)\Gamma(N)\eta\tau\sigma^2 \ln 2}.
$$
(3.30)

*(3.30) is thus equivalent to the EC in [37, Eq. (12)].*

*We next consider EC in [65, Eq. (15)], which is given as*

$$
\begin{aligned}
C &= \frac{1}{\ln 2} \sum_{i=1}^{\min(N,M)} \sum_{j=|N-M|}^{(N+M)i-2i^2} \frac{d(i,j)}{j!} \sum_{l=1}^{\min(N,M)} \sum_{m=|N-M|}^{(N+M)l-2l^2} \\
&\quad \frac{d(l,m)}{m!} \left( \frac{il}{D} \right) G_{2,4}^{4,1} \left( \frac{il}{D} \, \middle| \, \begin{matrix} -1, 0 \\ -1, -1, j, m \end{matrix} \right).
\end{aligned}
$$
(3.31)

*When $M = 1$, $\min(N, M) = 1$, $j = m = N - 1$, $(N + M)i - 2i^2 = (N + M)l - 2l^2 = N - 1$, $d(i, j) = d(l, m) = d(1, N - 1) = 1$. Therefore, (3.31)*

33

*is reduced to*

$$C = \frac{(1-\tau)PG_{2,4}^{4,1}\left(\frac{(1-\tau)P}{\eta\tau\sigma^2} \middle| \begin{matrix} -1,0 \\ -1,-1,N-1,N-1 \end{matrix}\right)}{\Gamma(N)\Gamma(N)\eta\tau\sigma^2 \ln 2}. \qquad (3.32)$$

*Obviously, (3.32) is equivalent to (3.30).*

**Asymptotic Throughput Analysis**

Asymptotic throughput is derived for two regimes; namely $\overline{\gamma} \to \infty$ and $N \to \infty$ to gain insights.

**Proposition 3.** *When $\overline{\gamma} \to \infty$, the asymptotic throughput of the delay tolerant transmission is given by*

$$R_{DT} = \frac{1-\tau}{\ln 2}\left[\xi + \ln \eta\overline{\gamma} - \ln \frac{1-\tau}{\tau}\right], \qquad (3.33)$$

*where $\xi = 2\sum_{n=1}^{N} A(n)\Gamma(n)\psi(n)$ and $\psi(x)$ is the Euler psi function [81, Eq. (8.360)].*

*Proof.* Let $R_{DT} = (1-\tau)C^*$ where

$$\begin{aligned} C^* &= \mathbb{E}\left[\log_2\left(1+\gamma_A\right)\right] \\ &\approx \left[\log_2 \frac{\tau\eta}{1-\tau}\overline{\gamma} + \mathbb{E}\left[\log_2(X)\right] + \mathbb{E}\left[\log_2(Y)\right]\right] \\ &= \frac{1}{\ln 2}\left[\xi + \ln \eta + \ln(\overline{\gamma}) - \ln \frac{1-\tau}{\tau}\right]. \end{aligned} \qquad (3.34)$$

We can readily show that for RV $Z$, $\mathbb{E}\left[\log(Z)\right] = \left.\frac{d\mathbb{E}\left[Z^{t-1}\right]}{dt}\right|_{t=1}$. Since both $X$ and $Y$ have the same PDF, $Z$ can be either $X$ or $Y$. We thus find that $\mathbb{E}\left[Z^{t-1}\right] = \sum_{i=1}^{N}\frac{A(i)}{\ln 2}\Gamma(i+t-1)\psi(i+t-1)$. We differentiate this and evaluate at $t=1$, which helps to compute the two $\mathbb{E}\left[\log_2(\cdot)\right]$ terms in (3.34). ∎

**Remark 4.** *From (3.33), for a given $\tau$, the system throughput depends on the logarithm of $\overline{\gamma}$ at high SNR. It can be observed that increasing the value of EH time $\tau$ will let the value outside the square brackets decrease but the value inside the square brackets rises. This means the EH time plays two conflicting roles in (3.33), and thus we can find an optimal value for $\tau$ to maximize the average throughput for delay-tolerant transmission mode.*

**Proposition 4.** *The optimal EH time $\tau^*$ for delay-tolerant mode at high SNR can be expressed as*

$$\tau^* \approx \frac{1}{1 + W\left(\eta\overline{\gamma}e^{\xi-1}\right)}, \tag{3.35}$$

*where $W(x)$ is the Lambert W function [86].*

*Proof.* First, we take the first-order derivative over $\tau$ of $C$ in (3.33) and equate it to zero as $\frac{dC}{d\tau} = 0$; We have $\xi + \ln\eta\overline{\gamma} - \frac{1}{\tau} = \ln\frac{1-\tau}{\tau}$; Then it can be written as $\eta\overline{\gamma}e^{\xi}e^{-\frac{1}{\tau}} = \frac{1-\tau}{\tau}$. Second, after some algebraic manipulations we have $\frac{1-\tau}{\tau} = W\left(\eta\overline{\gamma}e^{\xi-1}\right)$. The final result is given by using $W(\cdot)$ as $\tau = \frac{1}{1+W\left(\eta\overline{\gamma}e^{\xi-1}\right)}$. $W(x)$ is a monotonically increasing function for $x \geq 0$. From (3.35), we see that $\tau^*$ is inversely proportional to the parameters $\eta$, $\overline{\gamma}$ and $\xi$, where $\xi$ is a function that depends on the number of AP antenna. $\blacksquare$

**Proposition 5.** *When the number of antenna $N$ grows without limit, the delay-tolerant throughput can be expressed as*

$$\begin{aligned}
R_{DT} &= (1-\tau)\,\mathbb{E}\left[\log_2\left(1+\gamma_A\right)\right] \\
&\approx (1-\tau)\log_2\left(1 + \frac{\tau\eta}{1-\tau}\overline{\gamma}\rho^4 N^2\right) \\
&\approx (1-\tau)\left[\log_2\left(\frac{\tau\eta}{1-\tau}\rho^4 N^2\right) + \log_2\left(\overline{\gamma}\right)\right].
\end{aligned} \tag{3.36}$$

**Remark 5.** *This proposition follows from Corollary 4. The asymptotic throughput displays a logarithmic relation to the SNR, energy conversion efficiency $\eta$, the correlation coefficient and the number of AP antenna. For a given level of throughput, as $N \to \infty$, the transmit power requirements (i.e. represented by $\overline{\gamma}$) decrease. This is a beneficial trade off, resulting in less energy use. Moreover, the performance of energy and information transfer can be enhanced for long-distance transmission by adding antennas at the AP.*

**Remark 6.** *For massive MIMO systems, power scaling is an essential feature, which allows the deployment of large-scale antenna arrays to achieve the system target performance via scaling down transmit power [87], [88]. The transmit power can be scaled down as $P = \frac{\overline{P}}{N^r}$ for a fixed $\overline{P}$, and the average throughput becomes $R_{DT} \approx (1-\tau)\log_2\left(\frac{\tau\eta\rho^4\overline{P}}{(1-\tau)N^{2-r}}\right)$. When $r > 2$, the throughput grows without bound, which means the transmit power can be scaled down further.*

*However, when $r < 2$, the throughput converges to zero, which indicates that the transmit power has been reduced too much. When $r = 2$, the throughput converges to a constant $(1 - \tau) \log_2 \left( \frac{\tau \eta}{1 - \tau} \rho^4 \bar{P} \right)$.*

## 3.5    Average Symbol Error Rate Analysis

We next derive the error rates of our system for BPSK, BDPSK, coherent M-PSK and coherent square M-QAM. The average BER or average SER can be evaluated directly by averaging the conditional bit error rate, $P_{BER}(\cdot)$ or the conditional symbol error rate, $P_{SER}(\cdot)$ [89].

### 3.5.1    BPSK

**Exact Analysis**

BPSK is one of the most robust modulation schemes. Its conditional error probability is given as $P_{BER}(\gamma) = \lambda \operatorname{erfc}\left( \sqrt{\nu \gamma} \right)$, where $\operatorname{erfc}(\cdot)$ is the complementary error function [81, Eq. (8.250.1)] with $\lambda = \frac{1}{2}$ and $\nu = 1$. The average BER of BPSK is given as

$$
\begin{aligned}
\bar{P}_{BER} &= \int_0^\infty P_{BER}(\gamma) f_{\gamma_A}(\gamma) \, d\gamma \\
&\overset{(a)}{=} \int_0^\infty \lambda \operatorname{erfc}(\sqrt{\nu \gamma}) \sum_{n=1}^N \sum_{m=1}^N \frac{2B(m,n)}{c\bar{\gamma}} \\
&\quad \cdot \left( \frac{\gamma}{c\bar{\gamma}} \right)^{\alpha(m,n)} K_{n-m}\left( 2\sqrt{\frac{\gamma}{c\bar{\gamma}}} \right) d\gamma \\
&\overset{(b)}{=} \sum_{n=1}^N \sum_{m=1}^N \frac{B(m,n)\lambda}{c\bar{\gamma}\sqrt{\pi\nu}} \\
&\quad \cdot G_{2,3}^{2,2}\left( \frac{1}{\nu c\bar{\gamma}} \left| \begin{array}{c} 0, -\frac{1}{2} \\ \frac{n-m}{2} + \alpha(m,n), \frac{m-n}{2} + \alpha(m,n), -1 \end{array} \right. \right),
\end{aligned}
\tag{3.37}
$$

where (a) is due to submitting (3.4) and $P_{BER}(\gamma)$ in the equation of $\bar{P}_{BER}$; (b) is obtained by using the same integral as [89, eq. (8)] which expresses $\operatorname{erfc}(\cdot)$ in term of $G_{p,q}^{m,n}[\cdot]$ first, and then do the integral for Meijer G-function.

**Asymptotic Analysis**

Since the closed-form expression (3.37) is complicated with the Meijer G-function, the specific relationships between the parameters and the BER are not clearly visible. However, asymptotic BER expressions are simpler.

**Proposition 6.** *When $\bar{\gamma} \to \infty$, the asymptotic BER in this case is given as*

$$
\begin{aligned}
\bar{P}_{BER} = \sum_{m=1}^{N} \frac{B(m,1)}{4c\bar{\gamma}} &\left[ (-1)^{m-2} \left( \frac{1}{c\bar{\gamma}} \right)^{m-1} e^{\frac{1}{c\bar{\gamma}}} E_i \left( -\frac{1}{c\bar{\gamma}} \right) \right. \\
&\left. + \sum_{k=1}^{m-1} \Gamma(k) \left( -\frac{1}{c\bar{\gamma}} \right)^{m-k-1} \right].
\end{aligned}
\tag{3.38}
$$

*Proof.* See Appendix A.4. ∎

**Remark 7.** *In* (3.38)*, it is seen that $\bar{P}_{BER}$ decreases when SNR $\bar{\gamma}$ increases. Although the asymptotic BER is simpler than the closed-form expression* (3.37)*, it can be further simplified for two cases: imperfect CSI and perfect CSI.*

**Proposition 7.** (3.38) *is further simplified as*

$$
\bar{P}_{BER} \approx
\begin{cases}
\dfrac{(1-\rho^2)^{2(N-1)}}{4} (c\bar{\gamma})^{-1} \left[ \ln \bar{\gamma} + \ln(c) - \gamma_{EM} \right], \\
\hspace{6cm} 0 \le \rho < 1, \\
\dfrac{\Gamma\left(N+\frac{1}{2}\right)}{2N\sqrt{\pi}\Gamma(N)(tc\bar{\gamma})^N} \Psi\left(N,1;\dfrac{1}{c\bar{\gamma}}\right), \rho = 1.
\end{cases}
\tag{3.39}
$$

*Proof.* See Appendix A.5. ∎

### 3.5.2 BDPSK

**Exact Analysis**

For this modulation, the conditional error probability is given by $P_{BER}(\gamma) = \lambda e^{-\nu\gamma}$. In this case, the average of $P_{BER}(\gamma)$ is simply related to the MGF of $\gamma$. So the average BER can be derived by the MGF technique [90], [91]. It is

clear that the BER of BDPSK can be expressed as

$$\bar{P}_{BER} = \lambda M_{\gamma_A}(v)$$

$$= \sum_{n=1}^{N}\sum_{m=1}^{N} B(m,n)\lambda\left(\frac{1}{c\bar{\gamma}}\right)^{\alpha(m,n)+\frac{1}{2}}\Gamma(n)\Gamma(m) \tag{3.40}$$

$$\cdot e^{\frac{1}{2vc\bar{\gamma}}}\nu^{-\frac{1}{2}-\alpha(m,n)}W_{-\frac{1}{2}-\alpha(m,n),\frac{n-m}{2}}\left(\frac{1}{vc\bar{\gamma}}\right).$$

For BDPSK, the parameter values are $\lambda = \frac{1}{2}$ and $\nu = 1$. Although this result is exact, simpler yet accurate results are possible with the use of asymptotic MGF.

**Asymptotic Analysis**

To this end, we can use Corollary 2 to obtain the asymptotic performance of BDPSK. Thus, the asymptotic BER ($\bar{\gamma} \to \infty$) is given by

$$\bar{P}_{BER} = \lambda M_{\gamma_A}^{asy}(v)$$

$$= \sum_{m=1}^{N}\frac{B(m,1)}{vc\bar{\gamma}}\left[\sum_{k=1}^{m-1}\Gamma(k)\left(-\frac{1}{vc\bar{\gamma}}\right)^{m-1-k}\right. \tag{3.41}$$

$$\left. + (-1)^{m-2} e^{\frac{1}{vc\bar{\gamma}}}\left(\frac{1}{vc\bar{\gamma}}\right)^{m-1}E_i\left(-\frac{1}{vc\bar{\gamma}}\right)\right].$$

However, even further simplification is possible. By using Corollary 3, thus, asymptotic $\bar{P}_{BER}$ is obtained as follows;

$$\bar{P}_{BER} \approx \begin{cases} \lambda\left(1-\rho^2\right)^{2(N-1)}(cv\bar{\gamma})^{-1} \\ \quad \cdot\left[\ln\bar{\gamma} + \ln cv - \gamma_{EM}\right], & 0 \leq \rho < 1, \\ \dfrac{\lambda\left(vc\bar{\gamma}\right)^{-N}}{\Gamma(N)}\Psi\left(N,1;\dfrac{1}{vc\bar{\gamma}}\right), & \rho = 1. \end{cases} \tag{3.42}$$

### 3.5.3 For Coherent M-PSK

M-PSK modulation is widely used in advanced wireless networks such as LTE, WiMAX and others. For a given symbol rate, the information rate of M-PSK is significantly higher than that of BPSK. However, it needs more transmit power to keep the same error rates as BPSK.

**Exact Analysis**

The conditional SER for coherent M-PSK signals is given by [92]

$$P_{SER}\left(\gamma\right) = a \int_0^{\Lambda} e^{-b(\theta)\gamma} d\theta,$$

where $a = \frac{1}{\pi}$, $\Lambda = \frac{(M-1)\pi}{M}$, $b\left(\theta\right) = \frac{g_{PSK}}{\sin^2(\theta)}$ and $g_{PSK} = \sin^2\left(\frac{\pi}{M}\right)$. Since the SER expression is an integral of the exponential function, the expected value of this expression directly relates to the MGF.

Thus, the average SER, $\bar{P}_{SER}$, can be derived as

$$\begin{aligned}
\bar{P}_{SER} &= a \int_0^{\Lambda} M_{\gamma_A}\left(b\left(\theta\right)\right) d\theta \\
&= \sum_{n=1}^{N} \sum_{m=1}^{N} a B\left(m, n\right) \left(\frac{1}{c\overline{\gamma}}\right)^{\alpha(m,n)+\frac{1}{2}} \Gamma\left(n\right) \Gamma\left(m\right) \\
&\quad \cdot \int_0^{\Lambda} e^{\frac{1}{2b(\theta)c\overline{\gamma}}} b\left(\theta\right)^{-\frac{1}{2}-\alpha(m,n)} W_{-\frac{1}{2}-\alpha(m,n),\frac{n-m}{2}}\left(\frac{1}{b\left(\theta\right)c\overline{\gamma}}\right) d\theta,
\end{aligned} \tag{3.43}$$

where $\bar{P}_{SER}$ is obtained by Lemma 2. The finite integrals in (3.43) can be evaluated by mathematical software packages.

**Asymptotic Analysis**

We see that (3.43) has the Whittaker function, a complicated function. Thus, the relations between the parameters and the SER are not immediately evident. To alleviate this, similar to the BDPSK case, we derive the asymptotic results via Corollary 3 (Section 3.3)

$$\begin{aligned}
\bar{P}_{SER} &= a \int_0^{\Lambda} M_{\gamma_A}^{asy}\left(b\left(\theta\right)\right) d\theta \\
&= \sum_{m=1}^{N} \int_0^{\Lambda} \frac{B(m,1)}{b\left(\theta\right)c\overline{\gamma}} \left[ \sum_{k=1}^{m-1} \Gamma(k) \left(-\frac{1}{b\left(\theta\right)c\overline{\gamma}}\right)^{m-1-k} \right. \\
&\quad \left. + (-1)^{m-2} e^{\frac{1}{b(\theta)c\overline{\gamma}}} \left(\frac{1}{b\left(\theta\right)c\overline{\gamma}}\right)^{m-1} E_i\left(-\frac{1}{b\left(\theta\right)c\overline{\gamma}}\right) \right] d\theta,
\end{aligned} \tag{3.44}$$

where, the finite integrals in (3.44) can be evaluated by software.

We can simplify it further for imperfect CSI case ($0 \le \rho < 1$) and perfect

CSI case ($\rho = 1$), respectively as

$$
\bar{P}_{SER} \approx a \int_0^\Lambda \left(1 - \rho^2\right)^{2(N-1)} \left(cb\left(\theta\right)\bar{\gamma}\right)^{-1}
$$
$$
\cdot \left[\ln \bar{\gamma} + \ln \left(cb\left(\theta\right)\right) - \gamma_{EM}\right] d\theta
\tag{3.45}
$$

and

$$
\bar{P}_{SER} \approx a \int_0^\Lambda \frac{\lambda \left(b(\theta)c\bar{\gamma}\right)^{-N}}{\Gamma\left(N\right)} \Psi\left(N, 1; \frac{1}{b\left(\theta\right)c\bar{\gamma}}\right) d\theta.
\tag{3.46}
$$

### 3.5.4   M-QAM

M-QAM is widely used in digital communication networks. These include optical fiber networks, digital subscriber lines, IEEE 802.11, orthogonal frequency division mulitplexing (OFDM) based networks and more. By increasing constellation size $M$, it is possible achieve arbitrarily high spectral efficiencies.

**Exact Analysis**

The conditional SER for coherent square M-QAM signals is given by [93] [92]

$$
P_{SER}\left(\gamma\right) = \frac{4q}{\pi} \int_0^{\frac{\pi}{2}} e^{-h(\theta)\gamma} d\theta - \frac{4q^2}{\pi} \int_0^{\frac{\pi}{4}} e^{-h(\theta)\gamma} d\theta,
\tag{3.47}
$$

where $q = 1 - \frac{1}{\sqrt{M}}$, $h\left(\theta\right) = \frac{g_{QAM}}{\sin^2(\theta)}$ and $g_{QAM} = \frac{3}{2(M-1)}$. Then, SER of M-QAM can be derived as follow

$$
\bar{P}_{SER} = \int_0^\infty P_e\left(\gamma\right) f_{\gamma_A}\left(\gamma\right) d\gamma
$$
$$
= I_1 - I_2,
\tag{3.48}
$$

where $I_1$ and $I_2$ can be written as

$$
I_1 = \frac{4q}{\pi} \int_0^{\frac{\pi}{2}} M_{\gamma_A}\left(h\left(\theta\right)\right) d\theta
$$
$$
= \frac{4q}{\pi} \sum_{n=1}^N \sum_{m=1}^N B\left(m, n\right) \left(\frac{1}{c\bar{\gamma}}\right)^{\alpha(m,n)+\frac{1}{2}} \Gamma\left(n\right) \Gamma\left(m\right)
\tag{3.49}
$$
$$
\cdot \int_0^{\frac{\pi}{2}} e^{\frac{1}{2h(\theta)c\bar{\gamma}}} h\left(\theta\right)^{-\frac{1}{2}-\alpha(m,n)} W_{-\frac{1}{2}-\alpha(m,n),\frac{n-m}{2}}\left(\frac{1}{h\left(\theta\right)c\bar{\gamma}}\right) d\theta
$$

40

and

$$
\begin{aligned}
I_2 &= \frac{4q^2}{\pi} \int_0^{\frac{\pi}{4}} M_{\gamma_A}\left(h\left(\theta\right)\right) d\theta \\
&= \frac{4q^2}{\pi} \sum_{n=1}^{N} \sum_{m=1}^{N} B\left(m,n\right) \left(\frac{1}{c\overline{\gamma}}\right)^{\alpha(m,n)+\frac{1}{2}} \Gamma\left(n\right) \Gamma\left(m\right) \\
&\cdot \int_0^{\frac{\pi}{4}} e^{\frac{1}{2h(\theta)c\overline{\gamma}}} h\left(\theta\right)^{-\frac{1}{2}-\alpha(m,n)} W_{-\frac{1}{2}-\alpha(m,n),\frac{n-m}{2}}\left(\frac{1}{h\left(\theta\right)c\overline{\gamma}}\right) d\theta.
\end{aligned}
\tag{3.50}
$$

The finite integrals in (3.49) and (3.50) can be evaluated by software such as MATLAB.

**Asymptotic Analysis**

We can also find an asymptotic expression for (3.48). Similar to the case of BDPSK, we obtain the asymptotic result by using Corollary 2.

$$
\bar{P}_{SER} \approx P_1 - P_2,
\tag{3.51}
$$

where

$$
\begin{aligned}
P_1 &= \frac{4q}{\pi} \int_0^{\frac{\pi}{2}} M_{\gamma_A}^{asy}\left(h\left(\theta\right)\right) d\theta \\
&= \sum_{m=1}^{N} \frac{4q}{\pi} \int_0^{\frac{\pi}{2}} \frac{B(m,1)}{h\left(\theta\right)c\overline{\gamma}} \left[ \sum_{k=1}^{m-1} \Gamma(k) \left(-\frac{1}{h\left(\theta\right)c\overline{\gamma}}\right)^{m-1-k} \right. \\
&\quad \left. + (-1)^{m-2} e^{\frac{1}{h(\theta)c\overline{\gamma}}} \left(\frac{1}{h\left(\theta\right)c\overline{\gamma}}\right)^{m-1} E_i\left(-\frac{1}{h\left(\theta\right)c\overline{\gamma}}\right) \right] d\theta
\end{aligned}
\tag{3.52}
$$

and

$$
\begin{aligned}
P_2 &= \frac{4q^2}{\pi} \int_0^{\frac{\pi}{4}} M_{\gamma_A}^{asy}\left(h\left(\theta\right)\right) d\theta \\
&= \sum_{m=1}^{N} \frac{4q^2}{\pi} \int_0^{\frac{\pi}{4}} \frac{B(m,1)}{h\left(\theta\right)c\overline{\gamma}} \left[ \sum_{k=1}^{m-1} \Gamma(k) \left(-\frac{1}{h\left(\theta\right)c\overline{\gamma}}\right)^{m-1-k} \right. \\
&\quad \left. + (-1)^{m-2} e^{\frac{1}{h(\theta)c\overline{\gamma}}} \left(\frac{1}{h\left(\theta\right)c\overline{\gamma}}\right)^{m-1} E_i\left(-\frac{1}{h\left(\theta\right)c\overline{\gamma}}\right) \right] d\theta,
\end{aligned}
\tag{3.53}
$$

where the finite integrals in (3.52) and (3.53) can be readily evaluated by software such as MATLAB.

Using Corollary 3, for the imperfect case, when $0 \leq \rho < 1$ we can obtain

$$
\begin{aligned}
P_1 \approx \frac{4q}{\pi} \int_0^{\frac{\pi}{2}} \left(1 - \rho^2\right)^{2(N-1)} \left(ch\left(\theta\right)\overline{\gamma}\right)^{-1} \\
\cdot \left[\ln \overline{\gamma} + \ln \left(ch\left(\theta\right)\right) - \gamma_{EM}\right] d\theta
\end{aligned}
\tag{3.54}
$$

and

$$
\begin{aligned}
P_2 \approx \frac{4q^2}{\pi} \int_0^{\frac{\pi}{4}} \left(1 - \rho^2\right)^{2(N-1)} \left(ch\left(\theta\right)\overline{\gamma}\right)^{-1} \\
\cdot \left[\ln \overline{\gamma} + \ln \left(ch\left(\theta\right)\right) - \gamma_{EM}\right] d\theta.
\end{aligned}
\tag{3.55}
$$

For the perfect CSI case, where $\rho = 1$, we have

$$
P_1 \approx \frac{4q}{\pi} \int_0^{\frac{\pi}{2}} \frac{(h(\theta)c\overline{\gamma})^{-N}}{\Gamma(N)} \Psi\left(N, 1; \frac{1}{h\left(\theta\right)c\overline{\gamma}}\right) d\theta
\tag{3.56}
$$

and

$$
P_2 \approx \frac{4q^2}{\pi} \int_0^{\frac{\pi}{4}} \frac{(h(\theta)c\overline{\gamma})^{-N}}{\Gamma(N)} \Psi\left(N, 1; \frac{1}{h\left(\theta\right)c\overline{\gamma}}\right) d\theta.
\tag{3.57}
$$

**Remark 8.** *For BDPSK, M-PSK and M-QAM, the exact expressions are derived based on Lemma 2, and the asymptotic results are based on Corollary 2 and Corollary 3 (Section 3.3). For the imperfect CSI case, where $0 \leq \rho < 1$, it can be seen from (3.39), (3.42), (3.45), (3.54) and (3.55) that when the value of the product of $c\overline{\gamma}$ increases, the value of average BER/SER will converge to zero, which means either the energy conversion efficiency at the user or the AP transmit power rises, the BER/SER can be improved. For the perfect CSI case ($\rho = 1$), $\bar{P}_{BER}$ contains a confluent hypergeometric function and the impact of the parameters is not as explicit as the imperfect CSI case.*

## 3.6  Numerical and Simulation Results

This section provides Monte-Carlo simulations to validate analytical results and to evaluate the impacts of the key parameters, which are given in Table I.

### 3.6.1  Delay-Limited Mode

Fig. 3.2 plots the delay-limited throughput versus the average SNR with different numbers of AP antennas and the correlation coefficient $\rho$. As expected,

Table 3.1: Simulation Parameters

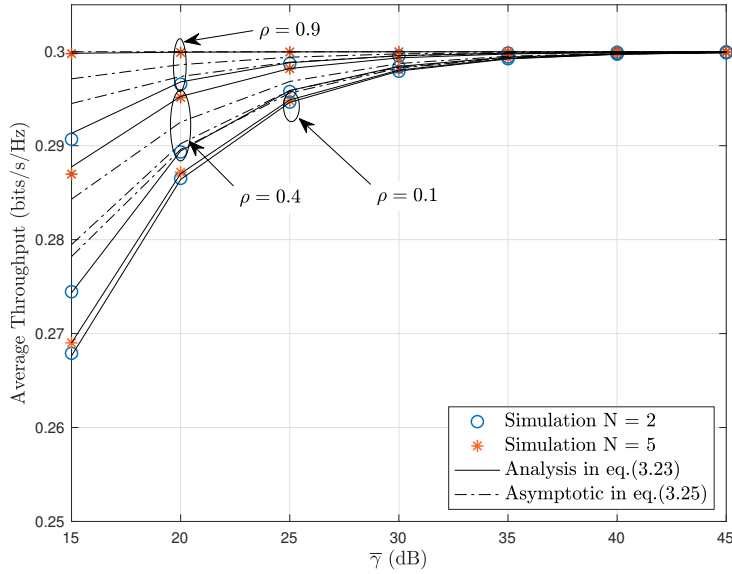| Notation | Parameter | Value |
|----------|-----------|-------|
| $T$ | Block duration | 1 |
| $\sigma^2$ | Noise variance | 0 dBm |
| $\bar{\gamma}$ | unfaded SNR | |
| $\rho$ | correlation | |



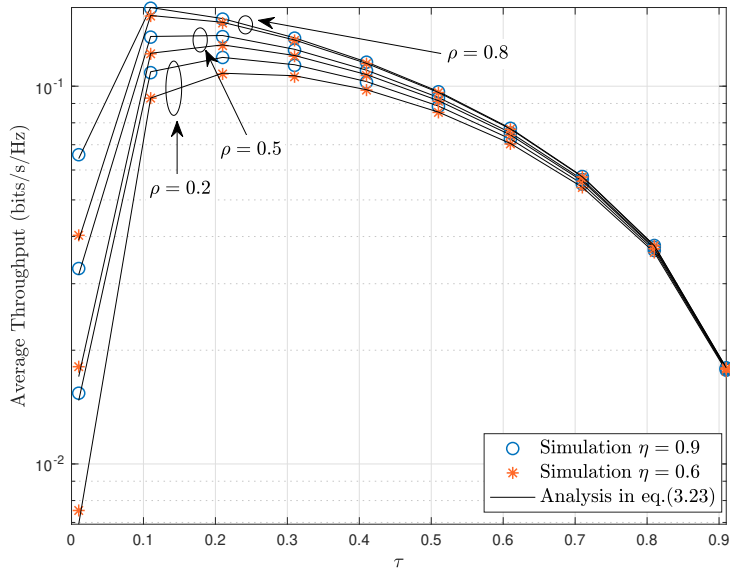Figure 3.2: Delay-limited throughput mode versus average SNR $\overline{\gamma}$ for $\tau = 0.4$, $\eta = 0.6$ and $R = 0.5\,\text{bits/s/Hz}$.

Figure 3.3: Delay-limited throughput versus EH time $\tau$ for $N = 3$ and $P = 10\,\mathrm{dBm}$.

when the transmit power or the number of AP antennas is increased, the average throughput improves. The simple reason is that more harvested energy is achieved as a result of higher energy beamforming gain and the AP transmit power. The throughput is also influenced by the quality of the CSI (e.g. correlation coefficient). When $\rho \approx 1$, the system has perfect CSI without noisy estimates. If $\rho \approx 0$, the poor performance results in poor throughput. The dotted lines represent the asymptotic throughput for $\overline{\gamma} \to \infty$ in (3.25), which improves when $\rho$ and the AP transmit power increase. When $\overline{\gamma}$ is large, all the curves converge to 0.3, which validates our analytical result that $R_{DL} = R^*$ as $\overline{\gamma} \to \infty$.

Fig. 3.3 plots the simulated and exact outage probability versus EH time $\tau$ with different correlation coefficients ($\rho$) and energy conversion efficiencies ($\eta$). We can observe that the throughput improves with increasing $\rho$. The figure also shows the relation between average throughput and energy conversion efficiency. Obviously, higher $\eta$ helps the user harvest more energy in the DL, so the user has more energy for UL data transmission. The curves are concave and they increase first and then decrease as the EH time increases. It is
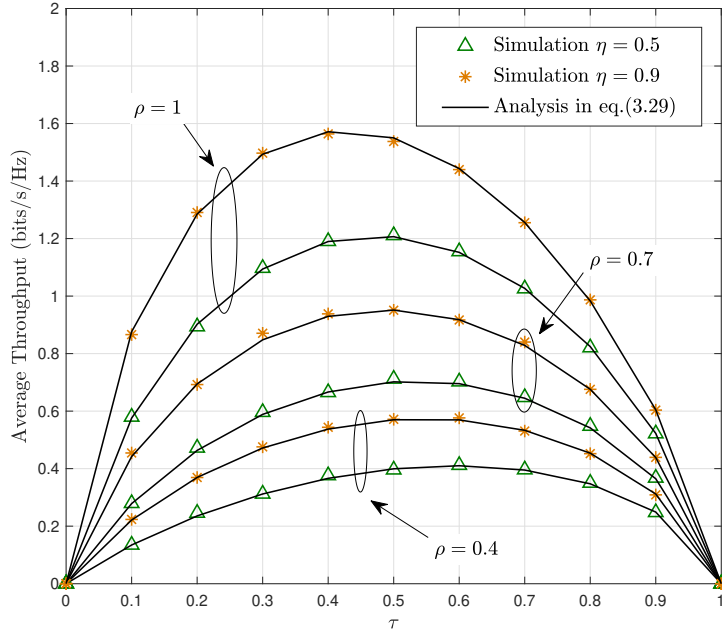
Figure 3.4: Delay-tolerant throughput versus EH time $\tau$ for $P = 1\,\text{dBm}$ and $N = 3$.

observed that the peak for the $\rho = 0.8$ curve is at $\tau = 0.1$, while the peaks for curves $\rho = 0.5$ and $\rho = 0.2$ are at $\tau = 0.2$. Thus, the optimal EH time is sensitive to the quality of channel estimations.

### 3.6.2 Delay-Tolerant Mode

Fig. 3.4 plots the delay-tolerant throughput versus EH time $\tau$ for several energy conversion efficiencies ($\eta$) and correlation coefficients ($\rho$). The figure shows a peak for each curve. This optimal EH time, $\tau^*$, balances EH time, $\tau$, and data transmission time, $(1 - \tau)$, perfectly. This coincides with our analytical results (3.29) and (3.35). Note that $\rho \approx 1$ is for perfect CSI and $\rho \approx 0$ is for totally noisy CSI. Thus, we can observe that larger $\rho$ and $\eta$ increase the throughput. Finally, we note that the simulation points (e.g. markers) lie exactly on the solid curves, which are the analytical results. Thus, this confirms that the derived theoretical results match with the simulations. This assures some confidence about the validity of the theoretical results.

Fig. 3.5 plots the delay-tolerant throughput versus the AP transmit power
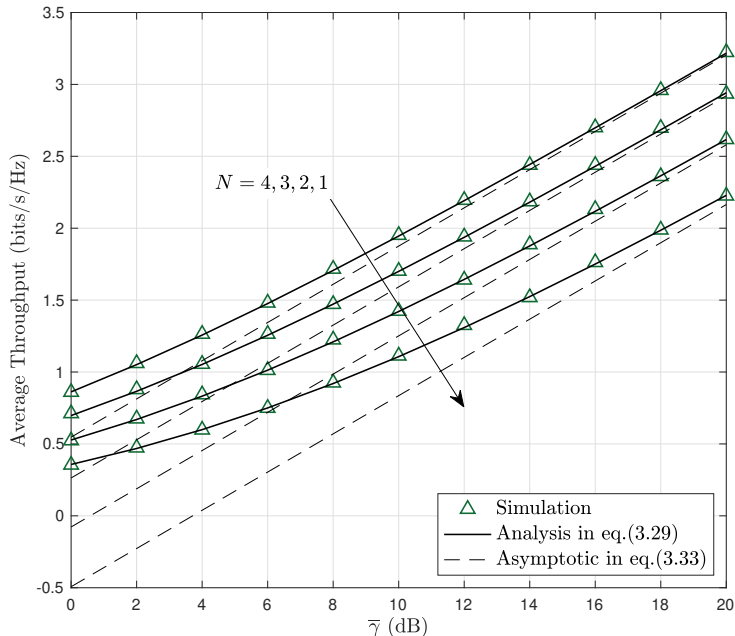
Figure 3.5: Delay-tolerant throughput versus $\overline{\gamma}$ for $\eta = 0.9$, $\tau = 0.6$ and $\rho = 0.6$.

with different numbers of AP antennas. Increasing both the transmit power and the number of antennas builds up the ergodic capacity. As well, the simulation result matches the analytical result in (3.29). Although the asymptotic curves (3.33) and the analytical curves (3.29) diverge for small values of the SNR ($\overline{\gamma}$), they converge as $\overline{\gamma}$ increases. Hence, the asymptotic expression is useful to correctly predict the characteristic of the delay-tolerant throughput performance in high SNR region.

Fig. 3.6 plots the delay-tolerant throughput versus the number of AP antennas, $N$. The solid lines and the circle markers represent the asymptotic analysis and simulations, respectively. The slopes of curves are large when $N$ is small, but increasing $N$ flattens out the curves. The asymptotic results converge to the simulations when either the number of antennas increase or $\rho$ increase. When $\rho \approx 1$, i.e., noise-free estimates, the simulation and asymptotic results coincide even for small $N$. However, with noisy estimates, more antennas are needed to obtain better performance. Finally, as before, increasing $\rho$ improves the throughput.
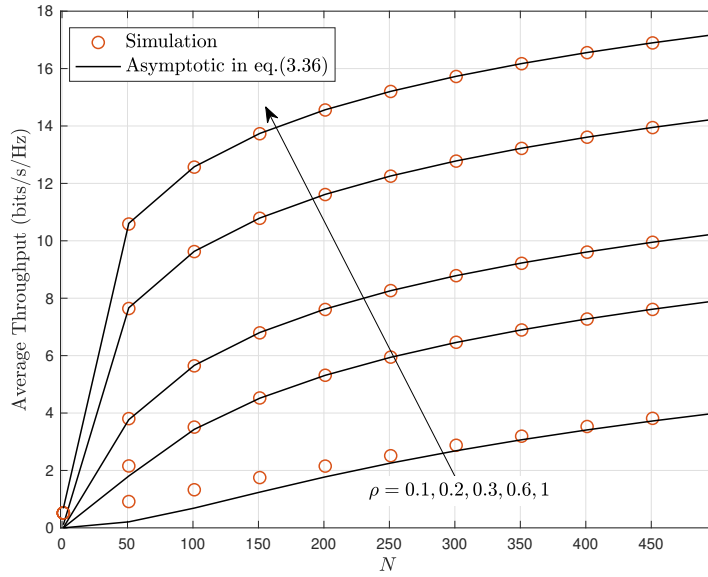
46

Figure 3.6: Delay-tolerant throughput versus $N$ for $\eta = 0.9$ and $\tau = 0.4$.
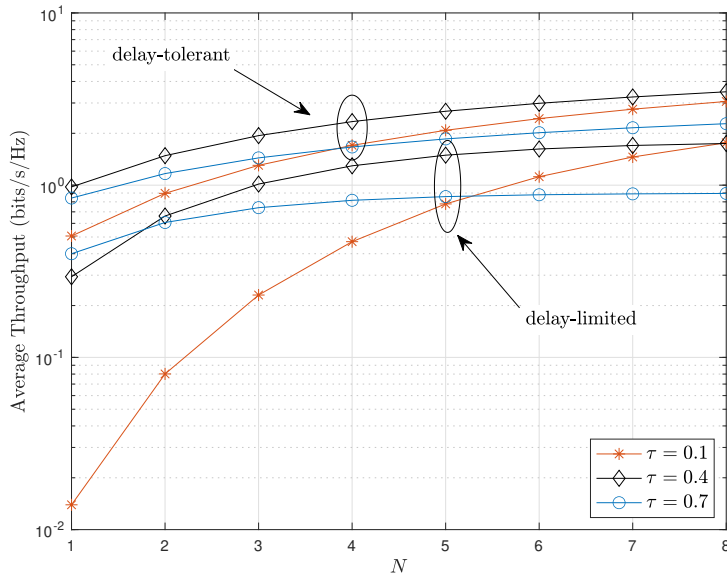


Figure 3.7: Average throughput versus the number of AP antennas for both delay-limited delay-tolerant modes with different EH time $\tau$, $P = 10\,\mathrm{dBm}$, and $\rho = 0.7$.
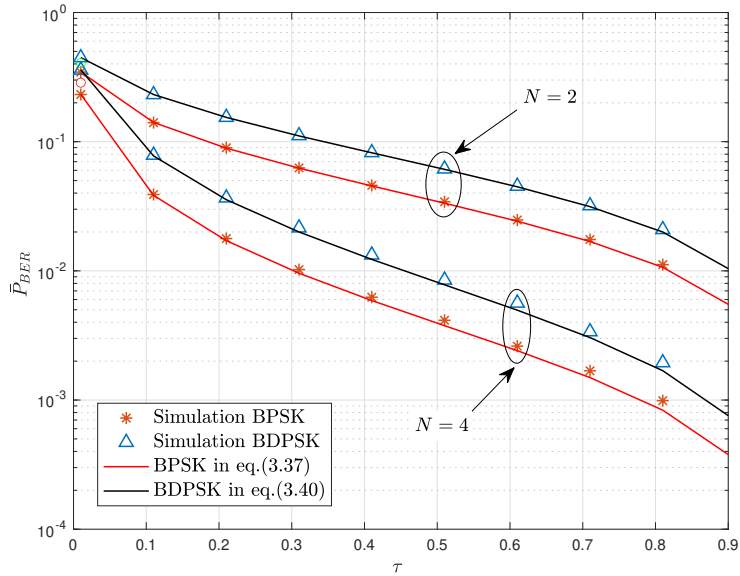
Figure 3.8: $\bar{P}_{BER}$ versus $\tau$ for $\rho = 0.8$, $\eta = 0.9$, $\nu = 1$ and $\lambda = 0.5$.

Fig. 3.7 shows average throughput of delay-limited and delay-tolerant modes versus the number of AP antennas, $N$ and different values of the EH time $\tau$. The throughput of the delay-tolerant mode increases with more AP antennas, and the slope of the curves gradually decreases. On the other hand, the throughput curves of the delay-limited mode first increases and then reach a ceiling when $N$ increases. This behaviour can be anticipated from (3.23) because the average throughput of the delay-limited mode is bounded by $R^*$. Moreover, it can be observed that the impact of $\tau$ for both throughput performances is unclear.

### 3.6.3 BER

Fig. 3.8 plots the BERs of BPSK in (3.37) and BDPSK in (3.40) versus EH time $\tau$ with different numbers of AP antennas. Solid lines represent the analytical results, while the markers (triangle and star) represent the simulation points. Thus, we clearly see a tight fit between simulation and the analytical results. BPSK has better performance than BDPSK for same parameters. It is observed that the deployment of more AP antennas improves the BER of both BPSK and BDPSK. Unlike the average throughput, where certain $\tau$ re-
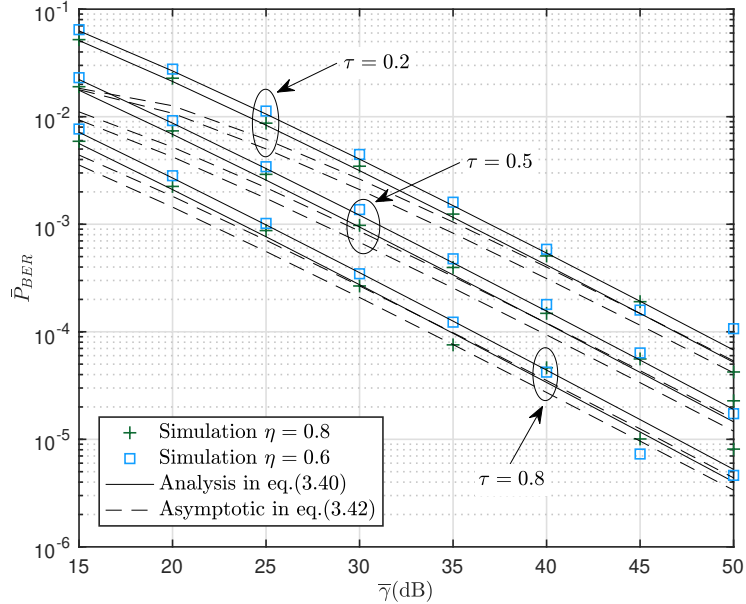
Figure 3.9: $\bar{P}_{BER}$ of BDPSK versus $\overline{\gamma}$ for $N = 4$, $\rho = 0.5$, $\nu = 1$ and $\lambda = 0.5$.

sults in the peak, the BER decreases when $\tau$ increases. We thus observe that the minimum BER is obtained when $\tau = 0.9$. This trend can be clearly seen from the asymptotic results (3.39) and (3.42). Of course, such large values of $\tau$ are not helpful in terms of throughput maximization.

Fig. 3.9 plots the average BER of BDPSK versus SNR for different EH conversion efficiencies ($\eta = 0.6, 0.8$) and EH times ($\tau = 0.2, 0.4, 0.8$). We see that the asymptotic results (dashed lines) approach the exact (solid lines) and simulation ones (markers) when SNR increases. As well, increasing SNR improves the BER performance. The BER decreases when the EH conversion efficiency or the EH time increases. It is observed that gaps between asymptotic and analysis depends on the EH time. $\tau$. It also can be observed that increasing EH time clearly improves the BER performance.

Fig. 3.10 plots analytical, simulated and asymptotic BERs of BPSK versus SNR. The number of AP antennas ($N$) is assumed as either 2 or 4, and the correlation coefficient ($\rho$) is 0.2, 0.4 or 0.8. Similar to the BDPSK case, increasing SNR improves the BER performance. In addition, Fig. 3.10shows that either adding more antennas at the AP or increasing the correlation coefficient
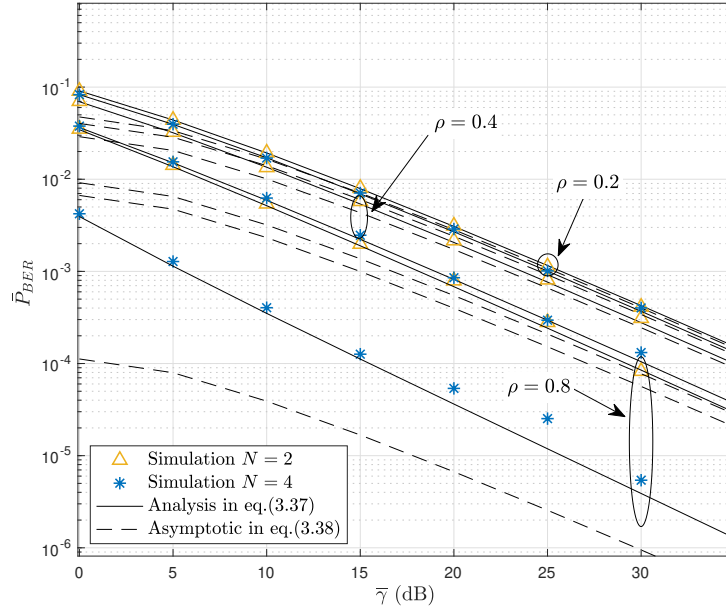
Figure 3.10: $\bar{P}_{BER}$ of BPSK versus $\bar{\gamma}$ for $\tau = 0.8$, $\eta = 0.5$, $\nu = 1$ and $\lambda = 0.5$.

can decrease BER. We can also see the analytical (solid lines) and asymptotic (dashed lines) results diverge for $(N = 4, \rho = 0.8)$, but when $N$ decreases, the gaps between analytical and asymptotic results are reduced quickly.

## 3.7   Summary

Although there has been a flurry of works on WPCNs, the impact of channel estimation errors on their performance has received scant attention. Thus, this chapter investigated this topic in detail. Specifically, we analyzed the distributions of the received SNR, the average throughput of delay-tolerant, delay-limit modes, and the BER/SER performances. Exact closed-form expressions as well as the high-SNR asymptotic results were derived. The correctness and effectiveness of these theoretical analysis were verified by Monte-Carlo simulation results. Our results show that in the high SNR region, the performance of one transmit and receive antenna coincides with that of multiple antennas at the AP. Due to energy beamforming at the DL, when the AP transmit power is large enough, the energy user harvests from one path is sufficient for the UL

information transmission. Numerical results showed that optimal EH times for delay-tolerant and delay-limit modes are different.

Our main findings from the derivations and the numerical results can be summarized as follows:

1. Unsurprisingly, the throughput and BER/SER performances can be improved by increasing the transmit power $P$, the number of antennas at the AP, correlation coefficient and EH conversion efficiency.

2. The optimal EH time fraction $\tau$ which maximizes the EH and data transmission rate can be derived for the delay-tolerant mode.

3. In the conventional analysis of non-EH wireless [53], [94], the asymptotic performance (e.g. BER, SER and outage) can be expressed in terms of diversity gain and coding gain (see (2.9)). But we have shown that this breaks down in the case of EH links. Instead, most asymptotic expressions tend to be of the form $\frac{\ln(\bar{\gamma})+c}{\bar{\gamma}^d}$ where $c$ and $d$ are some constants.

4. When the number of AP antennas becomes very large, the effect of small-scale fading vanishes. This is the well-known channel hardening effect in the massive MIMO literature.

# Chapter 4

# Performance Analysis for a WPCN with a New Nonlinear Energy Harvesting Model

## 4.1 Introduction

### 4.1.1 Background and Motivation

Internet of Things (IoT) has become a prevalent system to connect people, processes, data, and things connect. Globally, IoT connections will grow 2.4-fold, from 6.1 billion in 2018 to 14.7 billion by 2023 [95]. Mixed devices and connections are enabling myriad IoT apps. Connected-home, video-surveillance, connected appliances, and tracking apps will make up 48% of IoT connections by 2023. Energy used by these devices is increasing. Charging or replacing their batteries regularly adds additional cost and complexity of the networks. A solution is harvesting energy from ambient radio frequency (RF) or other energy sources[16], [96]. For example, access points (APs) may enable energy harvesting (EH) in the downlink in [37], [97], and both desired and interfering RF signals can be harvested for energy [98].

Thus, EH nodes use the harvest-then-transmit protocol [33] in wireless powered communication networks (WPCNs). That is, a power station (PS) or hybrid AP transfers energy to a wireless user in the downlink, who harvests energy and transmits information in the uplink to the data receiver. Consequently, the EH paradigm has been heavily researched [40], [46], [62], [74], [99].

While many works focus on EH performance for various wireless applications, the characteristics of the energy harvester are fundamental issues [100], [101]. These characteristics in fact determine the amount of harvested energy [51].

### 4.1.2 Energy Harvester Models

The linear EH model is the de facto standard for most works [33], [34], [37], [40], [41], [46], [47]. This model assumes that the output power of the energy harvester increases linearly with the input RF signal power. It thus suffers from two limitations. First, empirical works [43], [44], [48], [102] demonstrate that practical EH circuits display highly nonlinear characteristics, exhibiting a saturation plateau with high input powers as EH circuits employ nonlinear elements such as diodes and transistors [48], [103]. Thus, the unbounded increase predicted by the linear model is empirically wrong [104], [105]. Second, the output of the EH circuit drops to zero if the input RF is below a minimum input power level, which is known as the sensitivity level of the circuit. For example, it is $-25$ dBm at $1.3$ GHz for an EH circuit of 130-nm CMOS (complementary metal-oxide-semiconductor) [101] and $-22$ dBm at $915$ MHz for a 180-nm CMOS [106]. Most energy harvesters have an activation level due to the diode turn-on voltage, and if the received energy is below the level, the input energy is too small to be harvested [17]. Clearly, the two key properties of practical EH circuits are not correctly represented by the standard linear EH model.

Thus, to model practical EH circuits more accurately, several nonlinear models have been developed. Specifically, they include a piece-wise linear function [49], a rational function [50], a polynomial function [107], a sigmoid function [42], or an improved sigmoid function [52]. We briefly discuss their applications next.

Although the model [49] captures the saturation effect of practical EH circuits, it assumes a linear response up to the saturation level. Thus, this model may not fully match measured data. Nevertheless, this model offers a degree of analytical tractability and has thus been employed for outage performance analysis of relays [108], [109], secrecy analysis of relays [110], throughput anal-

ysis of WPCNs [111], and resource allocation of a WPCN [104]. Since the rational EH model [50] is not analytically tractable, it has been modified to a simpler form [51]. Both the models correctly exhibit the saturation characteristic. The polynomial model [107] is obtained by truncating the Taylor expansion of the diode output and it has been used for signal optimization. The sigmoid model [42] posits a logistic transfer function between the input and output powers. It captures the saturation characteristic of practical circuits but assumes zero sensitivity. It has been used to study resource allocation for non-orthogonal multiple access (NOMA) cognitive radio networks in [112], [113], outage probability and throughput [114] and many more. The sigmoid model has been modified in [52] to incorporate non-zero sensitivity levels. This modified model has been applied for energy beamforming optimization [115]. The non-linear models of [42] and [52] have been studied in [116]. We hasten to add that this overview is by no means complete.

### 4.1.3   Problem Statement and Contributions

The above review makes it clear that the non-linearity of practical EH circuits will clearly affect the performance and design of WPCNs and that the mismatch between the linear EH model and measured data can lead to bad design choices. For example, performance analysis based upon the linear model predicts overoptimistic results in terms of the common performance measures such as outage, ergodic capacity, error rate and so on. Additionally, the use of the linear EH model could be misleading for the uplink sum rate maximization problems. For these reasons, we need more accurate EH models.

In this chapter, we first propose two new nonlinear EH models. The first model has three parameters, which can be determined via a best-fit search of measured data [30], [102], [103]. The second is a simplified version of the first. We also develop a detailed performance analysis for a WPCN.

The main contributions are summarized as follows:

1. We suggest a new nonlinear EH model (NLEH), based on the error function. This model consists of three parameters, which can be estimated

54

by simple best-fit search with measured data. We also develop a new asymptotic model (AM). These two are then compared against the standard linear model (LM) and the rational model (RM) due to [51].

2. To further evaluate these four models, we investigate the throughput of the WPCN (Fig. 4.3) and bit error rates (BER) of binary phase shift keying (BPSK), binary differential phase shift keying (BDPSK) modulations. In particular, we derive the throughput of delay limited or tolerant modes.

3. We also consider the large antenna regime at the power station. In this case, the received power at the wireless device tends to the normal distribution. By exploiting this fact, we find the asymptotic throughput and BER expressions for new the EH model. Asymptotic results of other models can be derived similarly. The impact of transmit power control is also analyzed.

Furthermore, we assess the impact of the transmit power of the power station, the EH time, power amplifier efficiency at WD, the number of PS antennas and the number of IRS antennas via numerical simulations. From numerical results, we show that NLEH, AM, and RM models accurately reach the saturation state of practical EH circuits, but the LM model does not.

*Notation:* For random variable (RV) $X$, $f_X(\cdot)$ and $F_X(\cdot)$ denote the probability density function (PDF) and cumulative distribution function (CDF). A circularly symmetric complex Gaussian vector with mean $\mu$ and correlation matrix $\mathbf{B}$ is $\mathcal{CN}(\mu, \mathbf{B})$. The gamma function $\Gamma(a)$ is given in [81, Eq. (8.310.1)]; $\Gamma(a, x)$ is upper incomplete Gamma function given in [81, Eq. (8.350.2)]; $\Psi(a, b; z)$ is the confluent hypergeometric function given in [81, Eq. (9.211.4)]; $\gamma(n, x)$ is the lower incomplete gamma function [81, Eq. (8.350)]; $K_\nu(\cdot)$ is the $\nu$-th order modified Bessel function of the second kind [81, Eq. (8.432)]; $G_{pq}^{mn}\left(z \mid \begin{smallmatrix} a_1 \cdots a_p \\ b_1 \cdots b_q \end{smallmatrix}\right)$ denotes the Meijer G-function [81, Eq. (9.301)].

## 4.2 EH models

### 4.2.1 New Energy Harvesting Model

Here, we suggest a nonlinear EH model that captures the saturation character of practical circuits. The model posits that the harvested power at the output of the EH circuit can be expressed as

$$P_h = P_{\max} \left[ \frac{\mathrm{erf}(a(P_r + b)) - \mathrm{erf}(ab)}{1 - \mathrm{erf}(ab)} \right] \triangleq q(P_r), \qquad (4.1)$$

where $P_{\max}$ is the maximum harvested power level, and $P_r$ is the received RF power input, $a > 0$ and $b > 0$ are two parameters, and $\mathrm{erf}(x) = \frac{2}{\sqrt{\pi}} \int_0^x e^{-t^2} dt$ is the well-known error function. For large $x$, $\mathrm{erf}(x)$ tends to one; thus, in (4.1), as $P_r \to \infty$, $P_h \to P_{\max}$. The parameters $a, b$ and $P_{\max}$ can be determined via a best-fit match with experimental data.

The model (4.1) is general enough for a wide variety of applications. However, perhaps the simplest way to compare it against others is to compute the average of $P_h$. This depends on fading and other details of the EH link. In this chapter, we consider a specific WPCN (Fig. 3), which consists of a PS with $N \geq 1$ antennas and a wireless device (WD), which harvests RF energy. Suppose that the PS transmits at power level $P_t$. Let the large-scale path-loss between PS and WD be $\Omega_1$ and the small-scale channel be $\mathbf{h}$. Further details of these can be found in Section 4.3. The received RF signal power with maximum ratio transmission (MRT) beamforming at the PS, i.e., $\mathbf{w} = \frac{\mathbf{h}}{||\mathbf{h}||}$ [117], becomes $P_r = P_t \Omega_1 ||\mathbf{h}||^2 G_{\mathrm{PS}} G_{\mathrm{WD}} = \bar{P}_t ||\mathbf{h}||^2$ where $G_{\mathrm{PS}}$ and $G_{\mathrm{WD}}$ are the antenna gains of PS and WD, and $\bar{P}_t = P_t \Omega_1 G_{\mathrm{PS}} G_{\mathrm{WD}}$ is the transmit power corrected by the antenna gains and the path-loss. Thus, assuming the distance remains fixed, the average harvested power by the WD under this EH model is given by

$$\mathbb{E}[P_h] = \int_0^\infty q(x) f_{P_r}(x) dx. \qquad (4.2)$$

However, we need to compare this model with others in order to achieve a better assessment of the impact of EH models. Thus, we consider the following three models.

## 4.2.2 Asymptotic Model

To find a simpler model, we consider the region where the transmit power of the PS grows extremely large: e.g. $P_t \to \infty$. Ignoring the effect of fading, we can see that as $P_t$ becomes extremely large, the RF input power at the EH circuit also becomes very large: $P_r \to \infty$. The new nonlinear model (4.1) then predicts the harvested power level will be $P_{\max}$. Based on this fact, we suggest the following simple asymptotic model:

$$P_a = P_{\max}(1 - e^{-\kappa P_r}) \triangleq q_{as}(P_r), \tag{4.3}$$

where $\kappa$ is a constant. This model is simpler than (4.1) and may be more analytically tractable. Clearly, this model is very consistent with (4.1) in the asymptotic region. But we can choose $\kappa$ to make this model as accurate as possible for the entire input power range. So there may be several ways to find an optimal value of $\kappa$. A simple option is to make sure that both (4.1) and (4.3) have the same gradient at the input zero ($P_r = 0$). Thus, by matching the first derivatives of (4.1) and (4.3) at $P_r = 0$ point, we find

$$\kappa = 2 \frac{e^{-a^2 b^2} a}{\sqrt{\pi} \left(1 - \mathrm{erf}\,(ab)\right)}.$$

To recap, once we have measured data, the parameters of both of these models, (4.1) and (4.3), can be estimated readily.

As before, for comparative evaluations, we must compute the average of $P_a$. We consider the same WPCN (Fig. 4.3). With the same details given before, the average harvested power at the WD is given by

$$
\begin{aligned}
\mathbb{E}[P_a] &= \int_0^\infty q_{as}(x) f_{P_r}(x) dx \\
&= \frac{P_{\max}}{\bar{P}_t^N \Gamma\,(N)} \int_0^\infty (1 - e^{-\kappa x}) x^{N-1} e^{-\frac{x}{\bar{P}_t}} dx \\
&= P_{\max} \left[ 1 - \frac{1}{\left(1 + \kappa \bar{P}_t\right)^N} \right].
\end{aligned}
\tag{4.4}
$$

## 4.2.3 Linear Model

For completeness and for comparative evaluation purposes, we also consider the linear EH model, the most commonly used one in the literature. According

to this model, the harvested power at the output of the EH circuit is given by

$$P_l = \mu P_r \triangleq q_l(P_r). \qquad (4.5)$$

This model has only one parameter, namely $\mu$. It can be found by curve fitting with the measured input-output data of practical EH circuits.

However, in this case, we must compare this model with our NLEH model (4.1). To do so, we simply match the gradient of (4.1) at input zero with the constant $\mu$. Thus it is given by

$$\mu = 2P_{\max} \frac{\mathrm{e}^{-a^2 b^2} a}{\sqrt{\pi}\left(1 - \mathrm{erf}\left(ab\right)\right)}.$$

Once again, this constant is derived by matching the first derivatives of (4.1) and (4.5) at $P_r = 0$ point.

As before, we would like to compute the average of $P_l$. We consider the specific WPCN (Fig. 4.3). With the same details given before, the average harvested power at the WD is given by

$$\begin{aligned}
\mathbb{E}[P_l] &= \mu E[P_r] \\
&= \frac{\mu}{\left(\bar{P}_t\right)^N \Gamma(N)} \int_0^\infty x^N e^{-\frac{x}{\bar{P}_t}} dx \qquad (4.6) \\
&= \mu N \bar{P}_t.
\end{aligned}$$

Unsurprisingly, this models predicts a linear increase of the average harvested power with the transmit power. This however does not match with the behaviour of practical EH circuits.

### 4.2.4 Rational Model

There have been several rational EH models. For example, [50] examines a large number of energy harvesters and develops a ratio of two polynomials as the EH input-output characteristics. But this model ends up with seven parameters. Thus, a simplified rational EH model proposed in [51], which is equivalent to the following:

$$P_{rat} = \frac{P_{\max} P_r}{P_r + \beta} \triangleq q_{rat}(P_r). \qquad (4.7)$$
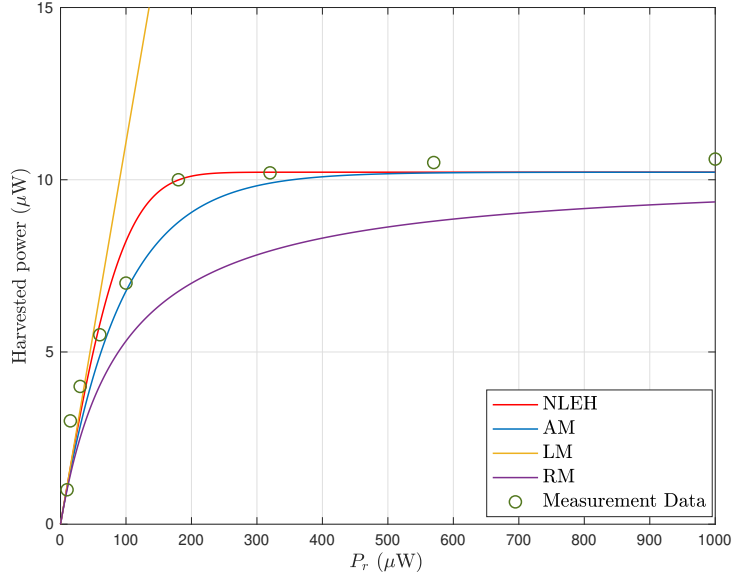
Figure 4.1: Harvested power for the four EH models and the measurement data [48, Fig. (17.d)].

This model has only two parameters, namely $P_{\max}$ and $\beta$. They can be found by curve fitting with measured data.

However, in this case, we want to compare this model with our NLEH model (4.1). To do so, constant $\beta$ is derived by matching the first derivatives of (4.1) and (4.7) at $P_r = 0$ point. Thus, we find

$$\beta = \frac{\sqrt{\pi}\,(1 - \text{erf}\,(ab))}{2\mathrm{e}^{-a^2 b^2} a}.$$

As before, we would like to compute the average of $P_{rat}$. We consider the specific WPCN (Fig. 4.3). With the same details given before, Under this model, the average harvested power at the WD is given by

$$
\begin{aligned}
\mathbb{E}[P_{rat}] &= \int_0^\infty q_{rat}(x) f_{P_r}(x) dx \\
&= P_{\max} \bar{P}_t^{-N} N \beta^N e^{\frac{\beta}{\bar{P}_t}} \Gamma\left(-N, \frac{\beta}{\bar{P}_t}\right),
\end{aligned}
\tag{4.8}
$$

where $\Gamma(a, x)$ is upper incomplete Gamma function given in [81, Eq. (8.350.2)] and the integral is obtained from [81, Eq. (3.383.10)].

Fig. 4.1 illustrates that the proposed new NLEH (4.1) tightly matches measurement data given in [48, Fig. (17.d)] for the load resistance $5.6\,\mathrm{M}\Omega$.

59

Table 4.1: RMSE Comparison

| Model | NLEH | [42] | [49] | AM | RM | LM |
|-------|------|------|------|------|------|------|
| RMSE | 0.70 | 0.92 | 1.67 | 0.80 | 1.82 | 38.8 |

The fitted parameters of the NLEH model are $a = 0.0086$, $b = 11.8689\,\mu$W and $P_{\max} = 10.219\,\mu$W with a root mean square error (RMSE) of 0.6963. In Table 4.1, we compared the RMSE values for several models. It is interesting to note that both AM and RM models achieve fairly small RMSE deviations. In contrast, the linear model is extremely poor in terms of matching with the measured data, a fact clearly evidenced by the extremely large RMSE value. Thus, we may expect that the use of the LM model will be overly optimistic compared to the measured data based models.

On the other hand, the LM model may be improved by adding a saturation effect. This gives rise to the so-called piece-wise linear model [49]. The RMSE of this model for this data set is found to be 1.72. Thus, we see that our proposed NLEH and AM models achieve better accuracy than the model of [49].

Compared with the sigmoid model of [42], we see that our proposed error function model is more accurate in terms of the RMSE. We have observed the same situation with another data set in [103, Fig. (5)]. Based on this limited comparison, using the measured data provided in [48, Fig. (17.d)], we can say that the new NLEH model provides a better approximation to the measured data than the sigmoid EH model. Of course, this situation may reverse for other measured data.

Fig. 4.2 compares the four models, (4.1), (4.3), (4.7) and (4.5) in terms of the average harvested power at the WD. We assume the EH circuit is part of the WD in the communication system (Fig. 4.3). The PS has $N = 3$ antennas and the WD has one. All the three nonlinear EH models show the saturation plateau, which coincides with measured data in Fig. 4.3. Clearly, RM and AM models approximate the NLEH model well for high input powers. However, the LM is inaccurate in modelling of practical EH circuits as the transmit
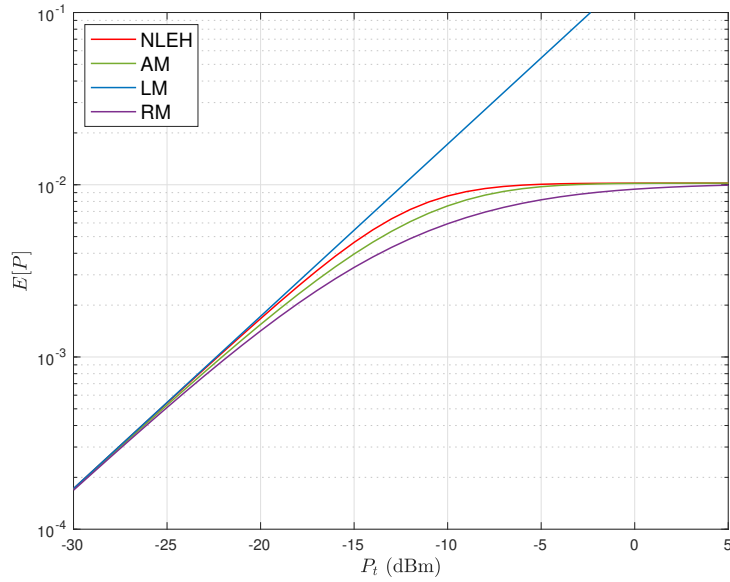
Figure 4.2: $E[P]$ of four EH models versus $P_t$ (dBm). Parameters $a = 0.0086$, $b = 11.8689\,\mu\mathrm{W}$ and $P_{\max} = 10.219\,\mu\mathrm{W}$, $N = 3$, $G_{\mathrm{PS}} = 11\,\mathrm{dBi}$, $G_{\mathrm{WD}} = 3\,\mathrm{dBi}$, and the distance between PS and WD is $4\,\mathrm{m}$.
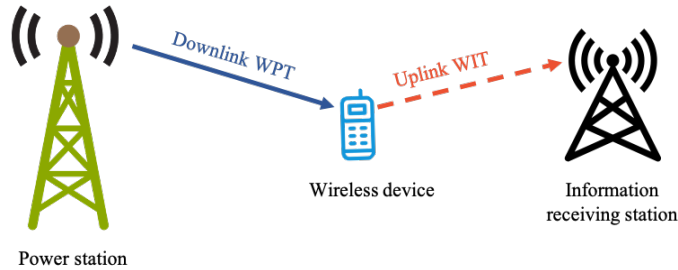


Figure 4.3: System model

power increases. Despite that, it can approximate the practical EH circuit for low transmit powers ($< -18$ dBm). Overall, the use of the LM model yields optimistic upper bounds on performance.

These four EH models will next be used for a system performance analysis. To set the scene for that, we next describe the communication system model.

## 4.3 Communication System Model

We consider a multiple-antenna WPCN with downlink wireless power transfer (WPT) and uplink wireless data transmission (WDT) (Fig. 4.3). We assume

energy beamforming in the downlink. Energy beamforming is a technology that the PS utilizes its multiple antennas to focus energy beams toward the WD. It thus maximizes the harvested energy at the WD [37], [82], [114]. MRT is thus assumed here for the transmit signals weighting at different PS antennas, since MRT is optimal for the single-user case [82]. The beamforming vector in the downlink WPT is $\mathbf{w} = \frac{\mathbf{h}}{||\mathbf{h}||}$. Besides, IRS uses maximum ratio combining (MRC) reception of uplink signals with a combining weight vector $\mathbf{u} = \frac{\mathbf{g}}{||\mathbf{g}||}$ [37] where $\mathbf{g}$ is the uplink channel between the WD and the IRS. Following [37], [118], we assume the availability of perfect channel state information (CSI) at the WD and IRS. For a duration of one transmission block $T$, $\tau T$ duration is used for downlink WPT, where $\tau \in (0, 1)$. The WD harvests energy in $\tau T$ and then transmits data in the uplink WDT for $(1 - \tau)T$ duration. Without loss of generality, we assume a normalized unit transmission block time (i.e., $T = 1$).

## 4.3.1 Channel Models

The small-scale mutipath fading part of the WPT channel is denoted as $\mathbf{h} \in \mathbb{C}^{N \times 1}$, which is distributed as $\mathbf{h} \sim \mathcal{CN}(0, I_N)$. Similarly, the WDT channel, i.e., WD-IRS is denoted as $\mathbf{g} \in \mathbb{C}^{M \times 1}$, which is distributed as $\mathbf{g} \sim \mathcal{CN}(0, I_M)$. Clearly, all the channel coefficients $h_k, g_k \, \forall k \in [1, N]$ are independent and identically distributed (i.i.d.) $\mathcal{CN}(0, 1)$ RVs. Consider $||\mathbf{h}||^2 = \sum_{i=1}^{N} |h_i|^2$ and $||\mathbf{g}||^2 = \sum_{j=1}^{M} |g_j|^2$. Thus, both $||\mathbf{h}||^2$ and $||\mathbf{g}||^2$ are scaled central Chi-square random variables distributed with $2N$ and $2M$ degrees of freedom. Thus, the PDF of both of them are special cases as following

$$f(x) = \frac{1}{\Gamma(L)} x^{L-1} e^{-x}, \quad 0 \le x < \infty, \tag{4.9}$$

where $L = N$ or $L = M$. The moment generating function (MGF) for this PDF is given by

$$M(t) = \mathbb{E}[e^{-tX}] = \frac{1}{(1+t)^L}, \quad \Re(t) > -1. \tag{4.10}$$

Although this MGF is well known, we list it here because the essential role it plays in our performance analysis. The role arises due to the fact that the

received signal power at the WD contains a factor $||\mathbf{g}||^2$, which is Gamma distributed. Thus, this MGF will help the overall averaging process, which can actually be done in two stages. The first stage can be the averaging over the distribution of $||\mathbf{g}||^2$, which requires the MGF in (4.10).

The PS-WD and WD-IRS distances are $d_1$ and $d_2$ respectively. The large-scale pathlosses of the WPT and WDT channels are $\Omega_k = d_k^{-s}$ ($k = 1, 2$) [119] where $s$ is the path loss factor and $d_k$ is the distance between the transmitter and the receiver, usually measured in meters [48].

## 4.3.2 Signal-to-Noise Ratio

In the downlink WPT, $P$ represents the power harvested at the WD via four different EH models described in Section 4.2, i.e., $P = P_h$ for NLEH, $P = P_a$ for AM, $P = P_l$ for LM, and $P = P_{rat}$ for RM. And for all these models, the input RF power is given by $P_r = \bar{P}_t ||\mathbf{h}||^2$. The WD harvests energy for duration $\tau$. Thus, the amount of energy harvested by the WD is $E_h = P\tau$. The WD transmits signals to the IRS for a duration of $(1 - \tau)$. Suppose that the WD uses a power amplifier with efficiency $0 < \eta < 1$. Out of the harvested energy, $\eta E_h$ is used for data transmission in the WD-IRS link and the remainder is consumed by the power amplifier [114]. Hence, during the data transfer phase, the transmit power of the WD is $P_{WD} = \frac{\eta E_h G_{\text{WD}}}{(1-\tau)}$. The signal-to-noise ratio (SNR) at the IRS can be written as

$$\gamma = \frac{\tau \eta P \Omega_2 G_{\text{WD}} G_{\text{IRS}} ||\mathbf{g}||^2}{(1 - \tau)\sigma^2} = cP||\mathbf{g}||^2, \tag{4.11}$$

where $G_{\text{IRS}}$ is the antenna gain of IRS and $c = \frac{\tau \eta \Omega_2 G_{\text{WD}} G_{\text{IRS}}}{(1-\tau)\sigma^2}$.

In the next section, we analyze the average throughput of delay-limited and delay-tolerant modes [37]. These modes are determined based upon the length of the codewords transmitted by the user. If codeword is short , and thus the receiver decodes each codeword without waiting to process several of them together, we have the delay limited mode. Consequently, in this case, outage probability (OP), the probability that the transfer rate below a given threshold, is the relevant measure of the system throughput. In contrast, in the delay-tolerant mode, the receiver may store multiple codewords and decode

them in one shot. The throughput in this case is measured by the long-term statistical average of the wireless channel capacity, i.e., ergodic capacity (EC).

## 4.4 Performance Analysis with Different EH Models

Herein, we derive the average throughput of the delay-limited and delay-tolerant transmission modes as well as the average BER of BPSK and BDPSK modulations. We analyze based on the four EH models. We derive integral expression for these performance metrics, and we suggest a very efficient and simple numerical evaluation method via the generalized Gauss-Laguerre quadrature (Appendix B.1.)

### 4.4.1 New Energy Harvesting Model

**Delay-Limited Transmission Mode**

In this mode, the IRS decodes each codeword, without waiting for a set of them. So in this case, short-term rise and fall of SNR mediates the success of each decoding operation. Therefore, OP is appropriate measure for the throughput of this mode. OP is the probability that the instantaneous throughput, $\log_2(1 + \gamma_A)$, falls below a fixed rate $R$ bits/s/Hz. Since the WD only transmits during the time fraction $(1 - \tau)$ with a fixed transmit rate $R$, the average throughput in bits/s/Hz can be expressed as

$$R_{DL} = (1 - P_{out}) R^*, \tag{4.12}$$

where $R^* = (1 - \tau) R$ and $P_{out}$ is the OP. In the following proposition, we derive the delay-limited throughput.

**Proposition 8.** *The average throughput of delay-limited mode of the WD-IRS link with the NLEH model* (4.1) *is given by*

$$R_{DL} = R^* \left[ 1 - \frac{\int_0^\infty \gamma \left( M, \frac{\gamma_{th}}{cq(\bar{P}_t x)} \right) x^{N-1} e^{-x} dx}{\Gamma(N) \Gamma(M)} \right], \tag{4.13}$$

64

where $\gamma_{th} = 2^R - 1$ is a predetermined threshold. In (4.13), $\gamma(n, x)$ is the lower incomplete gamma function [81, Eq. (8.350)] and $\Gamma(a)$ is gamma function [81, Eq. (8.310.1)].

*Proof.* The proof is given in Appendix B.3. ∎

**Remark 9.** *The $q(x)$ function in (4.13) is the nonlinear EH model given in (4.1). Since $q(x)$ contains an error function, and if we submit $q(x)$ into (4.13), the integral function is too complicated, so the closed-form expression does not exit. However, (4.13) can be approximated by generalized Gauss-Laguerre quadrature given in Appendix B.1. The impact of parameters is not clear in (4.13), but it can be observed from Section 4.5.*

**Delay-Tolerant Transmission Mode**

Delay-tolerant transmission mode is applied when the codeword length is large compared to the block time, so the IRS should tolerant a delay for decoding the stored signals together. Thus, the average throughput of this mode is the product of ergodic capacity and the effective data transmit time, which can be shown in bits/s/Hz as

$$R_{DT} = (1 - \tau) C_e, \tag{4.14}$$

where $C_e$ is the ergodic capacity. In the following proposition, we derive the delay-tolerant throughput.

**Proposition 9.** *The delay-tolerant throughput of the WDT link with the non-linear EH model (4.1) is given by*

$$R_{DT} = \frac{(1 - \tau)}{\Gamma(N)\Gamma(M)} \int_0^\infty I_{M-1}\left(\frac{1}{cq\left(\bar{P}_t x\right)}\right) \frac{x^{N-1}e^{-x}}{\left(cq\left(\bar{P}_t x\right)\right)^M} dx, \tag{4.15}$$

*where $I_n(a)$ is the function given in Lemma 3 in Appendix B.2.*

*Proof.* See the Appendix B.4. ∎

**Remark 10.** *The (4.15) can be evaluated by generalized Gauss-Laguerre quadrature via mathematical software, such as MATLAB. According to (B.2), the*

65

*number of summation terms n can be obtained by the following strategy. We write $W_i = \sum_{i=1}^{n} w_i f(x_i)$, $W_1 = w_1 f(x_1)$, and $W_i = W_{i-1} + w_i f(x_i)$. When $\frac{w_i f(x_i)}{W_i} \leq 0.01$, the series computation stops, and choose $n = i$.*

## Average BER of BPSK

BPSK is a simple digital modulation that uses two phases, say, 0 and $\pi$ to represent binary 0 and 1. Consequently, it can tolerate highest noise level or distortion than other higher-order modulations. Thus, BPSK is robust against thermal noise and other forms of noise as well as widely used in the standard IEEE 802.15.4 which is used by ZigBee [120]. In the following, we derive its BER as a simple integral.

**Proposition 10.** *The BER expression of the WD-IRS link with the nonlinear EH model (4.1) and BPSK modulation is given by*

$$
\begin{aligned}
\bar{P}_{BER} = \frac{1}{\Gamma(N)} \int_0^\infty x^{N-1} e^{-x} & \left[ \frac{1}{2} \left( 1 - \sqrt{\frac{cq(\bar{P}_t x)}{1 + cq(\bar{P}_t x)}} \right) \right]^M \\
\cdot \sum_{k=0}^{M-1} \binom{M-1+k}{k} & \left[ \frac{1}{2} \left( 1 + \sqrt{\frac{cq(\bar{P}_t x)}{1 + cq(\bar{P}_t x)}} \right) \right]^k dx.
\end{aligned}
\tag{4.16}
$$

*Proof.* See Appendix B.5. ∎

**Remark 11.** *Computationally, the BER expression (4.16) can be easily evaluated by the generalized Gauss-Laguerre quadrature rule given in Appendix B.1. It is observed that the specific relationship between parameters and the BER are not clearly visible. However, the relationship can be obtained through the numerical and simulation figures in Section 4.5.*

## Average BER of BDPSK

In BDPSK modulation, the phase of the modulated signal is shifted relative to the previous carrier's phase. BDPSK is used by wireless LAN (local area network) standard, IEEE 802.11b-1999 as the basic rate of 1 Mbit/s [121].

**Proposition 11.** *The BER expression of the WDT link with the nonlinear EH model (4.1) and BDPSK modulation is given by*

$$\bar{P}_{BER} = \frac{1}{2\Gamma(N)} \int_0^\infty \frac{x^{N-1}e^{-x}}{\left[1 + cq\left(\bar{P}_t x\right)\right]^M} dx. \tag{4.17}$$

*Proof.* The proof is given in Appendix B.6. ∎

**Remark 12.** *The expressions of BPSK and BDPSK above are complicated and cannot be derived closed form. But we can easily evaluate them via the generalized Gauss–Laguerre quadrature described in Appendix B.1.*

## 4.4.2 Asymptotic Model

In order to compare with the NLEH, we analyze the same performance metrics in the previous subsection. The function $q_{as}(\cdot)$ for the AM case is given in (4.3).

**Delay-Limited Transmission Mode**

According to Proposition 8, the delay-limited throughput of the WD-IRS link with the nonlinear EH model (4.3) can be given by

$$R_{DL} = R^* \left[ 1 - \frac{\int_0^\infty \gamma\left(M, \frac{\gamma_{\text{th}}}{cq_{as}\left(\bar{P}_t x\right)}\right) x^{N-1}e^{-x}dx}{\Gamma(N)\Gamma(M)} \right]. \tag{4.18}$$

The relationships of the throughput and parameters like $N$ and $M$ are not directly visible, but it can be observed in the Section 4.5.1.

**Delay-Tolerant Transmission Mode**

Using Proposition 9, the delay-tolerant throughput of the WDT link with the nonlinear EH model (4.3) is derived as

$$R_{DT} = (1 - \tau)\,\mathbb{E}\left[\log_2\left(1 + cP_a||\mathbf{g}||^2\right)\right]$$
$$\overset{(a)}{=} \frac{(1 - \tau)}{\Gamma(N)\Gamma(M)} \int_0^\infty I_{M-1}\left(\frac{1}{cq_{as}\left(\bar{P}_t x\right)}\right) \frac{x^{N-1}e^{-x}}{\left(cq_{as}\left(\bar{P}_t x\right)\right)^M} dx. \tag{4.19}$$

The $I_n(a)$ is a function of integral and it can be calculated as the finite summation in Lemma 3. Similar to Proposition 9, the integral can be evaluated by generalized Gauss-Laguerre quadrature.

**Average BER of BPSK**

The BER expression of the WD-IRS link with the nonlinear EH model (4.3) and BPSK modulation can be given as

$$\bar{P}_{BER} = \frac{1}{\Gamma(N)} \int_0^\infty x^{N-1} e^{-x} \left[ \frac{1}{2} \left( 1 - \sqrt{\frac{cq_{as}(\bar{P}_t x)}{1 + cq_{as}(\bar{P}_t x)}} \right) \right]^M$$
$$\cdot \sum_{k=0}^{M-1} \binom{M-1+k}{k} \left[ \frac{1}{2} \left( 1 + \sqrt{\frac{cq_{as}(\bar{P}_t x)}{1 + cq_{as}(\bar{P}_t x)}} \right) \right]^k dx. \tag{4.20}$$

This equation (4.20) can be obtained from Proposition 10 by replacing $q(\cdot)$ with $q_{as}(\cdot)$.

**Average BER of BDPSK**

The BER expression of the WDT link with the nonlinear EH model (4.3) and BDPSK modulation can be given as

$$\bar{P}_{BER} = \frac{1}{2\Gamma(N)} \int_0^\infty \frac{x^{N-1} e^{-x}}{\left[ 1 + cq_{as}(\bar{P}_t x) \right]^M} dx. \tag{4.21}$$

This equation (4.21) is derived similar to Proposition 11. Thus, the proof is omitted. In the next subsection, we will derive the performance of the mostly used linear EH model.

## 4.4.3 Linear EH Model

Since this is the default one used for a variety of networks, several results are already available. We list them here for completeness.

**Delay-Limited Transmission Mode**

According to Proposition 8, the average throughput linear EH model (4.5) is derived as follows.

$$
\begin{aligned}
R_{DL} &\overset{(a)}{=} R^* \left[ 1 - \frac{\int_0^\infty \gamma\left(M, \frac{\gamma_{\text{th}}}{c\mu\bar{P}_t x}\right) x^{N-1} e^{-x} dx}{\Gamma(N)\Gamma(M)} \right] \\
&\overset{(b)}{=} R^* \left[ 1 - \int_0^\infty \frac{\left(1 - e^{-\frac{\gamma_{\text{th}}}{c\mu\bar{P}_t x}} \sum_{m=0}^{M-1} \left(\frac{\gamma_{\text{th}}}{c\mu\bar{P}_t x}\right)^m \frac{1}{m!}\right) x^{N-1} e^{-x} dx}{\Gamma(N)} \right] \\
&\overset{(c)}{=} \frac{2R^*}{\Gamma(N)} \sum_{m=0}^{M-1} \left(\frac{\gamma_{\text{th}}}{c\mu\bar{P}_t}\right)^{\frac{N+m}{2}} \frac{1}{m!} K_{N-m}\left(2\sqrt{\frac{\gamma_{\text{th}}}{c\mu\bar{P}_t}}\right),
\end{aligned}
\tag{4.22}
$$

where (a) is from Proposition 8; (b) is because of [81, Eq. (8.352.6)]; (c) is obtained from [81, Eq. (3.471)]. $K_\nu(\cdot)$ is the $\nu$-th order modified Bessel function of the second kind [81, Eq. (8.432)].The special case $N = M$ has been studied in [37, Eq. (5)]. The average throughput $R_{DL}$ depends on $\tau$, $N$, $M$, $\gamma_{\text{th}}$, $P_t$ and $\mu$. It does not offer explicit relationships of the above parameters. However, we can find the impact of parameters in Section 4.5.

**Delay-Tolerant Transmission Mode**

The average throughput of delay-tolerant mode for the linear EH model (4.5) can be derived as

$$
R_{DT} = \frac{\frac{(1-\tau)}{c\mu\bar{P}_t} G_{2,4}^{4,1}\left(\frac{1}{c\mu\bar{P}_t} \left| \begin{array}{c} -1, 0 \\ -1, -1, M-1, N-1 \end{array}\right.\right)}{\Gamma(N)\Gamma(M)\ln 2},
\tag{4.23}
$$

where $G_{pq}^{mn}\left(z \mid \begin{array}{c} a_1 \cdots a_p \\ b_1 \cdots b_q \end{array}\right)$ denotes the Meijer G-function [81, Eq. (9.301)].and The special case $M = N$ of (4.23) has been derived in [37, Eq. (12)]. That same derivation can be used to prove (4.23). Thus, the details are omitted here. The average throughput $R_{DT}$ depends on parameters $\tau$, $N$, $M$, $P_t$ and $\mu$. However, insights can be derived from numerical evalution of (23).

**Average BER of BPSK**

The BER expression of the WD-IRS link with the linear EH model (4.5) and BPSK modulation is given by

$$\bar{P}_{BER} = \frac{1}{\Gamma(N)} \int_0^\infty x^{N-1} e^{-x} \left[ \frac{1}{2} \left( 1 - \sqrt{\frac{c\mu\bar{P}_t x}{1 + c\mu\bar{P}_t x}} \right) \right]^M$$

$$\cdot \sum_{k=0}^{M-1} \binom{M-1+k}{k} \left[ \frac{1}{2} \left( 1 + \sqrt{\frac{c\mu\bar{P}_t x}{1 + c\mu\bar{P}_t x}} \right) \right]^k dx. \tag{4.24}$$

This is result is similar to Proposition 10. Thus, the proof is omitted.

This integral (4.24) can be very efficiently and simply calculated by the generalized Gauss-Laguerre quadrature described in Appendix B.1.

**Average BER of BDPSK**

The BER expression of the WD-IRS link with the linear EH model (4.5) and BDPSK modulation is given by

$$\bar{P}_{BER} \overset{(a)}{=} \frac{1}{2\Gamma(N)} \int_0^\infty \frac{x^{N-1} e^{-x}}{\left[ 1 + c\mu\bar{P}_t x \right]^M} dx$$

$$\overset{(b)}{=} \frac{1}{2 \left( c\mu\bar{P}_t \right)^N} \Psi\left( N, N - M + 1; \frac{1}{c\mu\bar{P}_t} \right), \tag{4.25}$$

where (a) is obtained from Proposition 4; Step (b) is obtained from [81, Eq. (9.211.4)] and $\Psi(a, b; z)$ is the confluent hypergeometric function in [81, Eq. (9.211.4)].

In the next subsection, we derive the performances for the rational EH model.

## 4.4.4 Rational EH Model

### Delay-Limited Transmission Mode

Similar to Proposition 8, the delay-limited throughput of the WDT link with the rational EH model (4.7) can be given by

$$R_{DL} = R^* \left[ 1 - \frac{\int_0^\infty \gamma\left( M, \frac{\gamma_{\text{th}}}{cq_{rat}(\bar{P}_t x)} \right) x^{N-1} e^{-x} dx}{\Gamma(N)\Gamma(M)} \right]. \tag{4.26}$$

Since (4.26) is not closed-form, the relationships between $R_{DL}$ and the parameters, for example, $\gamma_{\text{th}}$, $N$, and $M$ from (4.26) are not directly visible. However, (4.26) is extremely easy to compute. Thus, insights can be obtained – see Section 4.5.

**Delay-Tolerant Transmission Mode**

The throughput of the WD-IRS link in this case with nonlinear EH model (4.7) can be given as

$$
\begin{aligned}
R_{DT} &= (1-\tau)\,\mathbb{E}\left[\log_2\left(1 + cP_{rat}||\mathbf{g}||^2\right)\right] \\
&\overset{(a)}{=} \frac{(1-\tau)}{\Gamma(N)\,\Gamma(M)} \\
&\quad \cdot \int_0^\infty I_{M-1}\left(\frac{1}{cq_{rat}\left(\bar{P}_t x\right)}\right) \frac{x^{N-1}e^{-x}}{\left(cq_{rat}\left(\bar{P}_t x\right)\right)^M}\,dx.
\end{aligned}
\tag{4.27}
$$

By replacing $q(\cdot)$ in Proposition 9 to $q_{rat}(\cdot)$, we obtain (4.27). The integral in (4.27) can be readily calculated by using Lemma 3 and the Gaussian-Laguerre quadrature (Appendix B.1.)

**Average BER of BPSK**

The BER of the WD-IRS link and the nonlinear EH model (4.7) and BPSK modulation can be obtained by

$$
\begin{aligned}
\bar{P}_{BER} &= \frac{1}{\Gamma(N)}\int_0^\infty x^{N-1}e^{-x}\left[\frac{1}{2}\left(1 - \sqrt{\frac{cq_{rat}\left(\bar{P}_t x\right)}{1 + cq_{rat}\left(\bar{P}_t x\right)}}\right)\right]^M \\
&\quad \cdot \sum_{k=0}^{M-1}\binom{M-1+k}{k}\left[\frac{1}{2}\left(1 + \sqrt{\frac{cq_{rat}\left(\bar{P}_t x\right)}{1 + cq_{rat}\left(\bar{P}_t x\right)}}\right)\right]^k\,dx.
\end{aligned}
\tag{4.28}
$$

By replacing $q(\cdot)$ in Proposition 10 with $q_{rat}(\cdot)$, we can obtain (4.28).

**Average BER of BDPSK**

**Proposition 12.** *The BER of the WD-IRS link with the rational EH model (4.7) and BDPSK modulation can be expressed as*

$$
\begin{aligned}
\bar{P}_{BER} &= \frac{\sum_{k=0}^M \binom{M}{k}\left(\frac{M\bar{P}_t}{\beta}\right)^k\left(\frac{\beta}{A}\right)^{N+k}\Gamma(N+k)}{2\Gamma(N)} \\
&\quad \cdot \Psi\left(N+k, N-M+k+1; \frac{\beta}{A}\right).
\end{aligned}
\tag{4.29}
$$

*Proof.* By using Proposition 11, we write the BER as Step (a) in the following:

$$
\begin{aligned}
\bar{P}_{BER} &\overset{(a)}{=} \frac{1}{2\Gamma(N)} \int_0^\infty \frac{x^{N-1}e^{-x}}{\left[1 + cq_{rat}\left(\bar{P}_t x\right)\right]^M} dx \\
&\overset{(b)}{=} \frac{1}{\Gamma(N)} \int_0^\infty \frac{x^{N-1}e^{-x}}{\left(1 + c\frac{M\bar{P}_t x}{M\bar{P}_t x + \beta}\right)^M} dx \\
&\overset{(c)}{=} \frac{1}{2\Gamma(N)} \int_0^\infty \frac{x^{N-1}e^{-x}\left(M\bar{P}_t x + \beta\right)^M}{\left[Ax + \beta\right]^M} dx \qquad (4.30)\\
&\overset{(d)}{=} \frac{\sum_{k=0}^M \binom{M}{k} \left(\frac{M\bar{P}_t}{\beta}\right)^k \left(\frac{\beta}{A}\right)^{N+k} \Gamma(N+k)}{\Gamma(N)} \\
&\quad \cdot \Psi\left(N+k, N-M+k+1; \frac{\beta}{A}\right),
\end{aligned}
$$

where $A = (1+c)M\bar{P}_t$; Step (b) follows from the rational model in (4.7); Let $u = \frac{Ax}{\beta}$ in (c), and with the help of [81, Eq. (9.211.4)], (d) is obtained after some algebraic manipulations. ∎

**Remark 13.** *Although* (4.30) *gives exact value of the average BER of BPSK, it does not show the direct relationships between the parameters $N$, $M$, $\beta$, and $P_t$ because it contains a confluent hypergeometric function. However, by considering the large antenna case ($N \to \infty$), we can obtain simpler but accurate performance expressions.*

## 4.4.5 Large Antenna Case

Wireless systems with an especially high number of antennas, e.g., tens or even hundreds of antennas, are called massive MIMO. Systems with as many as 96 to 128 antennas have been demonstrated. MIMO network can multiply the capacity of a wireless connection without requiring more spectrum. Thus, large capacity improvements are possible. More antennas translate into more possible signal paths, which improves and data rate and link reliability [122], [123].

In the following, we consider the PS to be massive MIMO, e.g., $N \to \infty$. In this case, we will see a channel hardening effect.

Let the WPT channel gain be $X = ||\mathbf{h}||^2$ and in this case, $X \xrightarrow{d} \mathcal{N}(N, N)$. Recall the received power at the WD is $P_r = \bar{P}_t ||\mathbf{h}||^2$. Thus $P_r \xrightarrow{d} \mathcal{N}\left(\bar{P}_t N, \bar{P}_t^2 N\right)$. In the previous section, we dealt with the problem of computing average throughput and BER in the format $\mathbb{E}[Y]$, where $Y$ is a function of $P_r$, i.e. $Y = g(P_r)$. But evaluating $\mathbb{E}[Y]$ is not direct. To avoid this issue, we can expand $Y$ around the mean of $P_r$, which is $\theta = \bar{P}_t N$. The quantity $Y$ is expanded as

$$Y = g(\theta) + g'(\theta)(P_r - \theta) + \frac{1}{2}g''(\theta)(P_r - \theta)^2 + \cdots \tag{4.31}$$

By taking the expected value of both sides, we find

$$\mathbb{E}[Y] = g(\theta) + \frac{1}{2}g''(\theta)\mathbb{E}\left[(X - \theta)^2\right] + \cdots \tag{4.32}$$

The right side can be approximated as

$$\mathbb{E}[Y] \approx g(\theta) + E, \tag{4.33}$$

where the error term is given by

$$E = \frac{1}{2}g''(\theta)\bar{P}_t^2 N. \tag{4.34}$$

In general, it is difficult to estimate the magnitude of this error term. But in order to get at least some sense of this error term, we can evaluate it for the linear model in (4.25). In this case, we find $g(x) = \frac{1}{(1+tx)^M}$ where $t = c\mu\bar{P}_t$. By evaluating, this term for (4.34), we find that

$$E \approx \frac{M(M+1)}{t^M \bar{P}_t^M N^{M+1}} = O\left(\frac{1}{N^{M+1}}\right). \tag{4.35}$$

Thus, this error term vanishes rapidly when the number of PS antennas is large enough. Therefore, we expect (4.33) to be highly accurate in this case.

The asymptotic performance for large antenna case with the new EH model (4.1) can be derived by following the approximated results obtained in (4.33) as following propositions:

**Proposition 13.** *When the number of PS antennas increases without bound, i.e. $N \to \infty$, the asymptotic average throughput of delay-limited mode for the*

*WD-IRS link with the NLEH (4.1) is given by*

$$R_{DL} = R^* \left[ 1 - \frac{1}{\Gamma(M)} \gamma \left( M, \frac{\gamma_{th}}{cq(\bar{P}_t N)} \right) \right].$$

(4.36)

*Compared to the exact result in (4.13), the asymptotic result (4.36) is closed-form and simpler.*

**Proposition 14.** *When the PS antenna increases, $N \to \infty$, the asymptotic average throughput of delay-tolerant mode for the WD-IRS link with the NLEH (4.1) is given by*

$$R_{DT} = \frac{(1 - \tau)}{\Gamma(M) \left( cq(\bar{P}_t N) \right)^M} I_{M-1} \left( \frac{1}{cq(\bar{P}_t N)} \right).$$

(4.37)

**Proposition 15.** *When the energy harvesting at the WD is modeled according to the NLEH model (4.1), the asymptotic average BER of BPSK over WD-IRS link for large $N$ is given by*

$$\bar{P}_{BER} = \left[ \frac{1}{2} \left( 1 - \sqrt{\frac{cq(\bar{P}_t N)}{1 + cq(\bar{P}_t N)}} \right) \right]^M$$
$$\cdot \sum_{k=0}^{M-1} \binom{M-1+k}{k} \left[ \frac{1}{2} \left( 1 + \sqrt{\frac{cq(\bar{P}_t N)}{1 + cq(\bar{P}_t N)}} \right) \right]^k.$$

(4.38)

*In the large antenna case, we can simply (4.38) as*

$$\bar{P}_{BER} \approx \left[ \frac{1}{2} \left( 1 - \sqrt{\frac{cP_{\max}}{1 + cP_{\max}}} \right) \right]^M$$
$$\cdot \sum_{k=0}^{M-1} \binom{M-1+k}{k} \left[ \frac{1}{2} \left( 1 + \sqrt{\frac{cP_{\max}}{1 + cP_{\max}}} \right) \right]^k$$

(4.39)

*where $N \to \infty$.*

**Proposition 16.** *When the WD utilizes NLEH (4.1) model to harvest energy, the asymptotic average BER of BDPSK over WD-IRS link for large $N$ is obtained by using (4.17) as*

$$\bar{P}_{BER} = \frac{1}{2 \left[ 1 + cq(\bar{P}_t N) \right]^M}.$$

(4.40)

74

(4.40) *can be further simplified as*

$$\bar{P}_{BER} = \frac{1}{2 \sum_{k=0}^{M} (cP_{\max})^k}. \tag{4.41}$$

The asymptotic expressions for the AM, LM, and RM models are easily derived similarly. We omit the details for brevity.

### 4.4.6   Impact of Transmit Power Control

In massive MIMO systems, power scaling laws describe how fast the transmission power can decrease with the increasing of the number of antennas while maintaining certain performance levels [124]. For example, [88] investigates massive MIMO relay networks with imperfect channel state information, co-channel interference. Overall, energy savings are possible. The following proposition describes the achievable throughput of our system when transmit power control is implemented.

**Proposition 17.** *When the number of PS antennas increases without a bound* $(N \to \infty)$, *for transmit power control* $P_t = \frac{P_0}{N}$, *the average throughput of the delay-tolerant mode for the NLEH model is given as*

$$R_{DT} = \frac{(1 - \tau)}{\Gamma(M)(cz)^M} I_{M-1}\left(\frac{1}{cz}\right), \tag{4.42}$$

*where* $z = P_{\max}\left[\frac{\text{erf}(a(\bar{P}_0+b))-\text{erf}(ab)}{1-\text{erf}(ab)}\right]$ *and* $\bar{P}_0 = P_0\Omega_1 G_{PS}G_{WD}$.

*Proof.* Recall that $\mathbf{h} \sim \mathcal{CN}(0, I_N)$. When the number of PS antennas increases without a bound, the law of large numbers suggests that $\frac{\mathbf{h}^H\mathbf{h}}{N} \xrightarrow{a.s.} 1$, where $\xrightarrow{a.s.}$ denotes almost sure convergence.

Recall $\gamma = \frac{\tau\eta P\Omega_2 G_{\text{WD}}G_{\text{IRS}}||\mathbf{g}||^2}{(1-\tau)\sigma^2}$. For the NLEH model, the harvested energy at the WD is $P = P_{\max}\left[\frac{\text{erf}(a(\bar{P}_t||\mathbf{h}||^2+b))-\text{erf}(ab)}{1-\text{erf}(ab)}\right]$ and SNR can be written as $\gamma = cP_{\max}\left[\frac{\text{erf}(a(\bar{P}_t||\mathbf{h}||^2+b))-\text{erf}(ab)}{1-\text{erf}(ab)}\right]||\mathbf{g}||^2$. Assume $P_t = \frac{P_0}{N}$, where $P_0$ is a fixed value and $\bar{P}_t = \frac{\bar{P}_0}{N}$. When the number of PS antennas increases $(N \to \infty)$, the SNR is given as $\lim_{N\to\infty} \gamma = cP_{\max}\left[\frac{\text{erf}(a(\bar{P}_0+b))-\text{erf}(ab)}{1-\text{erf}(ab)}\right]||\mathbf{g}||^2 = cz||\mathbf{g}||^2$. Therefor,

Table 4.2: Simulation Parameters

| Parameter | Description | Value |
|-----------|-------------|-------|
| $T$ | Block duration | 1 |
| $d_1$ | PS-WD distance | $4\,\mathrm{m}$ |
| $d_2$ | WD-IRS distance | $10\,\mathrm{m}$ |
| $s$ | Path loss exponent | 2.8 |
| $\sigma^2$ | Noise variance | $-60\,\mathrm{dBm}$ |
| $a$ | Best fit [21] | 0.0086 |
| $b$ | Best fit [21] | $11.8689\,\mu\mathrm{W}$ |
| $P_{\max}$ | Maximum harvested power | $10.219\,\mu\mathrm{W}$ |
| $G_{\mathrm{PS}}$ | Antenna gain at PS | $11\,\mathrm{dBi}$ |
| $G_{\mathrm{WD}}$ | Antenna gain at WD | $3\,\mathrm{dBi}$ |
| $G_{\mathrm{IRS}}$ | Antenna gain at IRS | $11\,\mathrm{dBi}$ |

the throughput of the delay-tolerant mode is

$$
\begin{aligned}
R_{DT} &= \mathbb{E}\left[\log_2\left(1+\gamma\right)\right] \\
&= \mathbb{E}\left[\log_2\left(1+cz||\mathbf{g}||^2\right)\right] \\
&= \frac{(1-\tau)}{\Gamma\left(M\right)\left(cz\right)^M} I_{M-1}\left(\frac{1}{cz}\right).
\end{aligned}
\tag{4.43}
$$

∎

**Remark 14.** *Note that (4.42) is a constant limit independent of the number of antennas. It shows that when the PS antennas $N$ grows without a bound, the transmit power can be scaled down proportionally to $\frac{1}{N}$ to maintain the same capacity.*

## 4.5   Numerical Results

Herein, we provide extensive numerical results based on our analytical derivations and simulation results based upon Monte-Carlo simulations. The latter helps us to validate the former. Table 4.2 provides the key parameters. The NLEH model (4.1) parameters are obtained by standard curve fitting using the data set [48, Fig. (17.d)]. The parameters of the other three models are then computed based upon Section 4.2.
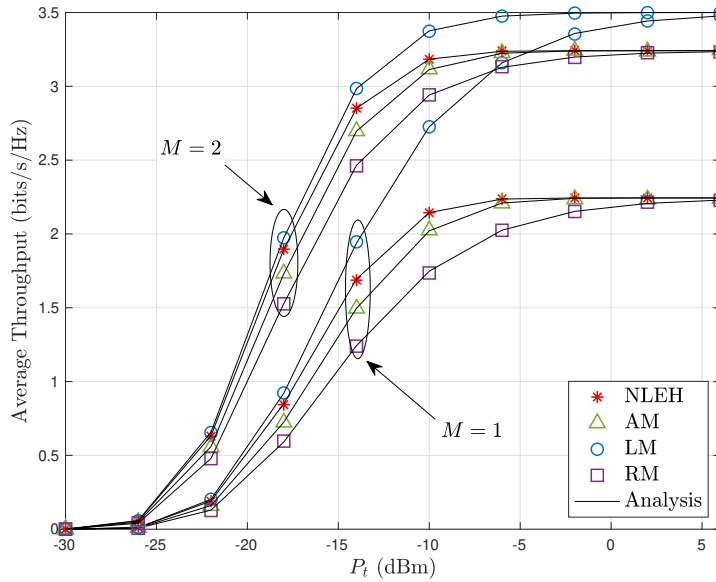
Figure 4.4: Average throughput of delay-limited transmission mode versus $P_t$ for $\tau = 0.3$, $R = 5$ bits/s/Hz, $N = 4$, and $\eta = 0.4$. The markers represent simulation points.

## 4.5.1 Throughput of the Delay-Limited Mode

Fig. 4.4 plots the average throughput of delay-limited mode versus the PS transmit power $(P_t)$ for different numbers of IRS antennas $(M)$. Fig. 4.4. yields several observations. First, the throughput for the four EH models increases first and then converges to a plateau as $P_t$ increases. This coincides with the delay-limited throughput analytical results obtained in Section 4.4, for example, (4.13), (4.18), (4.22) and (4.26). Second, among these models, The LM model suggests the largest throughput, which indicates the overoptimistic nature of LM. Finally, one sees that increases $M$ can improve the delay-limited throughput; for instance, with $P_t = -14$ dBm and NLEH model, average throughput increases from 1.6 bits/s/Hz for $M = 1$ to 2.7 bits/s/Hz for $M = 2$. The reason is that the IRS uses MRC to receive signals, more antennas can improve the performance.

Fig. 4.5 shows the effect of transmit rate $(R)$ on the average throughput of delay-limited transmission mode for four different EH models. Obviously, the values of average throughput rise first and then drop to 0. According to
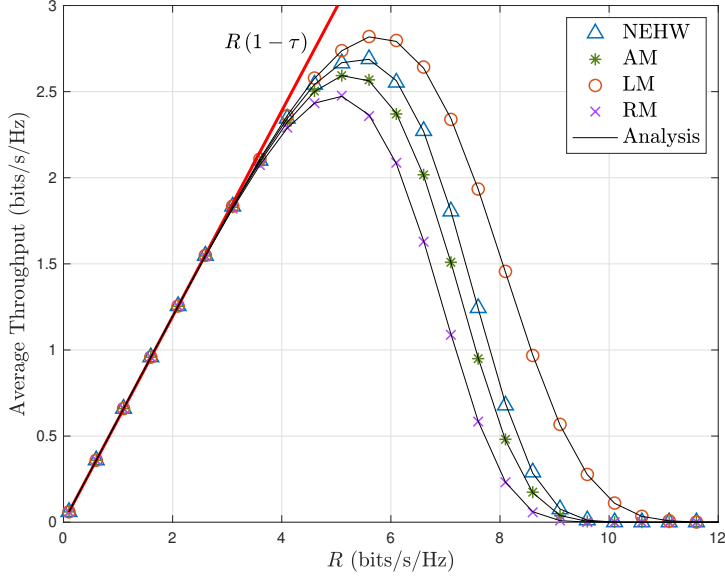
Figure 4.5: Average throughput of delay-limited transmission mode versus $R$ for $P_t = -10\,\text{dBm}$, $\tau = 0.4$ and $\eta = 0.4$, $N = 2$, and $M = 2$.

(4.12) and (B.10), the average throughput of delay-limited mode is given as $R_{DL} = R(1 - \tau)\left[1 - \Pr\left(\gamma < 2^R - 1\right)\right]$. From this equation, we can obtain that $R_{DL} \to 0$ when $R \to 0$ or $R \to \infty$, which matches the results shown in Fig. 4.5. Besides, the upper bound on the average throughput is $R(1 - \tau)$. In order to achieve highest average throughput of delay-limited mode, we choose the values of $R$ as $R = 5.5\,\text{bits/s/Hz}$ for LM and NLEH mode, $R = 5\,\text{bits/s/Hz}$ for AM and RM.

### 4.5.2 Throughput of the Delay-Tolerant Mode

Fig. 4.6 shows the average throughput of delay-tolerant mode versus the transmit power $(P_t)$ at the PS for EH time fraction $\tau = 0.6$, number of PS antennas $N = 2$, number of IRS antennas $M = 2$, and power amplifier efficiency at WD $\eta = 0.8$ or $\eta = 0.4$. The throughput improves with increasing $\eta$ since more harvested energy is used for information transmitted in the WD-IRS link. The average throughput is also improved by increasing the transmit power at the PS. However, the trends of the increment are different for the linear EH model and nonlinear EH models. Specifically, the throughput with nonlinear mod-
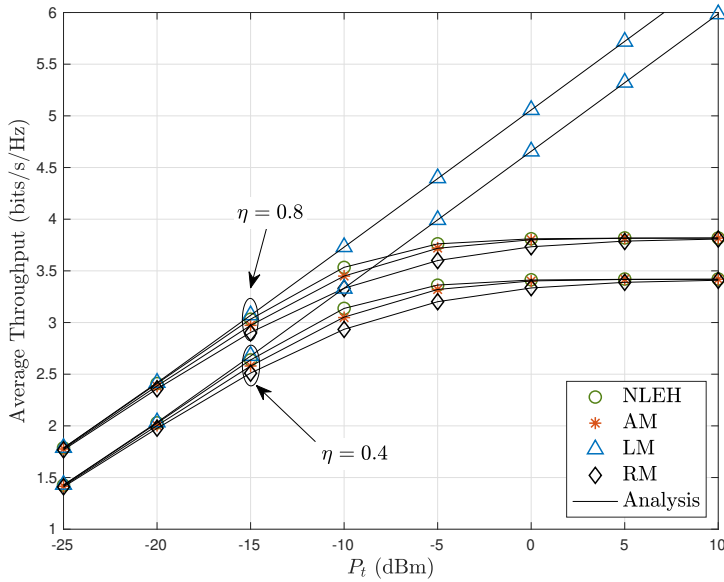
78

Figure 4.6: Average throughput of the delay-tolerant mode versus $P_t$ for $\tau = 0.6$, $N = 2$, and $M = 2$. The markers represent simulation points.

els tends to be saturated to maximum values (3.8 bits/s/Hz for $\eta = 0.8$ and 3.3 bits/s/Hz for $\eta = 0.4$) when the transmit power of the PS is high enough. However, the average throughput of the LM model grows monotonically as the PS transmit power increases. Clearly, this model fails to match the saturation property of practical EH circuits.

Fig. 4.7 plots the average throughput of delay-tolerant transmission mode versus the number of PS antennas ($N$) for transmit power $P_t = -15\,\mathrm{dBm}$, energy harvest time fraction $\tau = 0.7$, and power amplifier efficiency at WD $\eta = 0.6$. The number of IRS antennas ($M$) is either 2 or 4. It is seen that the value of average throughput for $M = 4$ is larger than that $M = 2$ which indicates adding more antennas at the IRS improves the throughput. We see that the asymptotic results (dashed lines) quickly approach the exact (solid lines) and simulation curves as the number of AP antennas increases. Besides, increasing the number of PS antennas boosts the average throughput of delay-tolerant mode when $N \leq 7$ and for $N > 7$, the saturation status is shown in nonlinear models whereas the curves of LM increasing without bound. Thus, LM is not appropriate for modeling the practical EH system. Especially when

79

Figure 4.7: Average throughput of delay-tolerant mode versus $N$ for $P_t = -15\,\mathrm{dBm}$, $\tau = 0.7$ and $\eta = 0.6$. The markers represent simulation points.
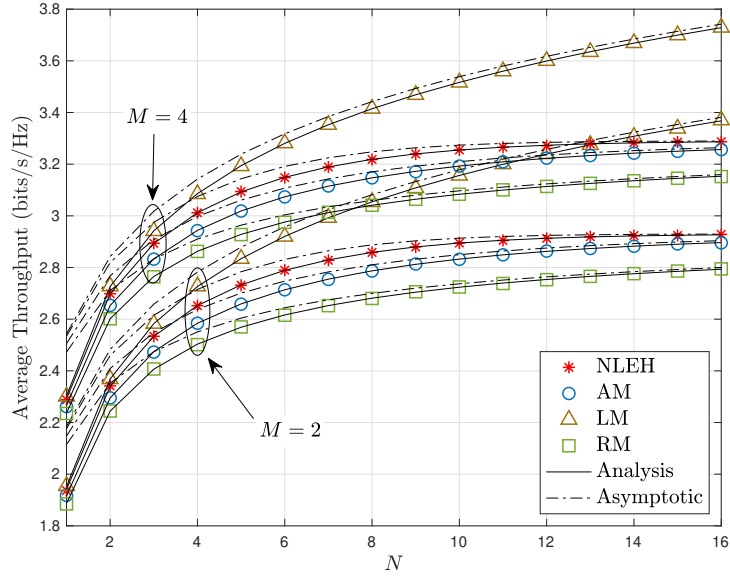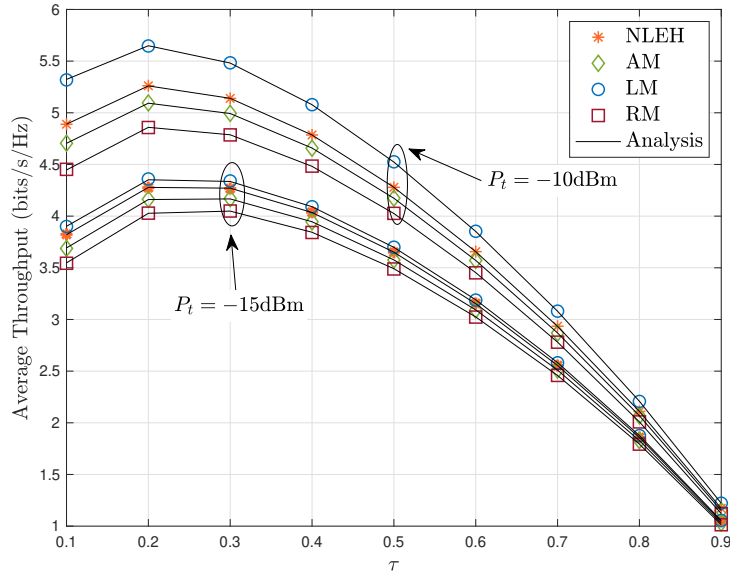


Figure 4.8: Average throughput of delay-tolerant mode versus $\tau$ for $N = 2$, $M = 3$, and $\eta = 0.6$. The markers represent simulation points.
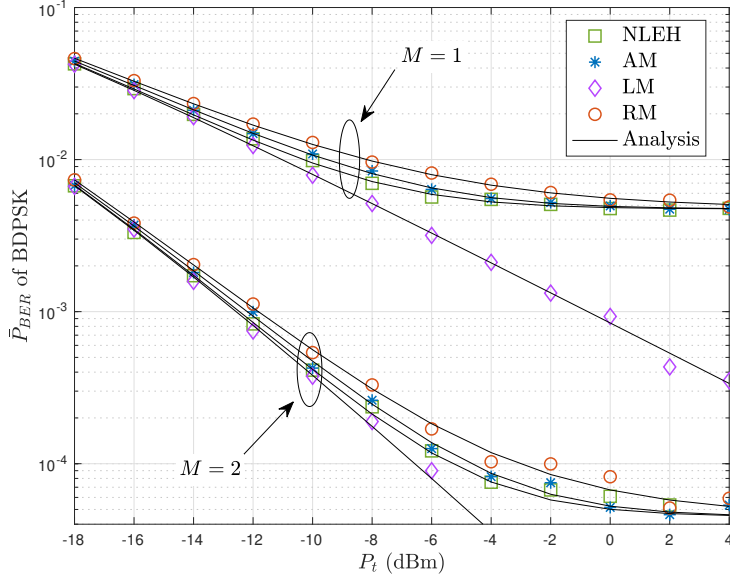
Figure 4.9: $\bar{P}_{BER}$ versus $P_t$ for $\tau = 0.4$, $N = 2$, $\tau = 0.3$ and $\eta = 0.6$. The markers represent simulation points.

the transmit power is large. Fig. 4.8 plots the average throughput of delay-tolerant mode versus EH time fraction $\tau$ to demonstrate the impact of $\tau$ to this mode. It can be seen that a throughput-optimal EH time exists for four EH models. The optimal EH time for four EH models are around $\tau = 0.2$, which balances the downlink EH, and uplink information transfer, perfectly. Moreover, average throughput can be improved by increasing the transmit power at the PS.

### 4.5.3  BER Performance

In Fig. 4.9, the average BER of BDPSK versus transmit power $(P_t)$ at the PS is investigated. The BERs of nonlinear EH models, i.e., NLEH, AM and RM models, first decrease and then flatten as the transmit power of the PS increases. In contrast, the LM model suggests that the BER decreases arbitrarily as $P_t$ increases. These coincide with the characteristics of four EH models shown in Fig. 4.9. Therefore, using the LM in WPCN system design may result in misleading and wrong conclusions. However, nonlinear EH models show more practical performances. Moreover, Fig. 4.9 also shows adding
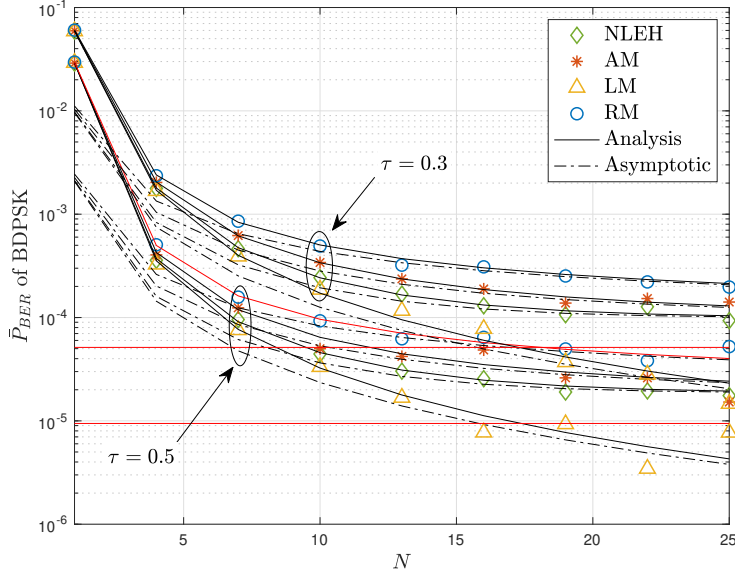
81

Figure 4.10: $\bar{P}_{BER}$ versus $N$ for $P_t = -18\,\text{dBm}$, $M = 2$, and $\eta = 0.4$. The markers represent simulation points.

more antennas at the PS reduces BER of the system significantly.

Fig. 4.10 shows the BER of BDPSK versus the number of PS antennas $(N)$ for transmit power $P_t = -18\,\text{dBm}$, power amplifier efficiency at WD $\eta = 0.4$, and number of IRS antenna $M = 2$. Fig. 4.11 plots the BER of BPSK versus $N$ for $P_t = -20\,\text{dBm}$, $\tau = 0.5$, and $M = 2$. The red horizontal lines in both figures are asymptotic results derived from (4.41) and (4.39), respectively. It can be seen that red lines are lower bound for nonlinear EH models whereas LM does not have lower bound. Increasing the number of PS transmit antennas decreases the BER in both figures. Dashed lines are asymptotic results which gradually tend to the exact values (solid lines) as $N$ increases in both figures. It is also observed that LM has smallest BER values of BDPSK and BPSK but this only works for small transmit power region. In Fig. 4.10, BER of BDPSK for $\tau = 0.5$ outperforms the one for $\tau = 0.3$ and in Fig. 4.11, we see that BER is improved by increasing $\eta$.
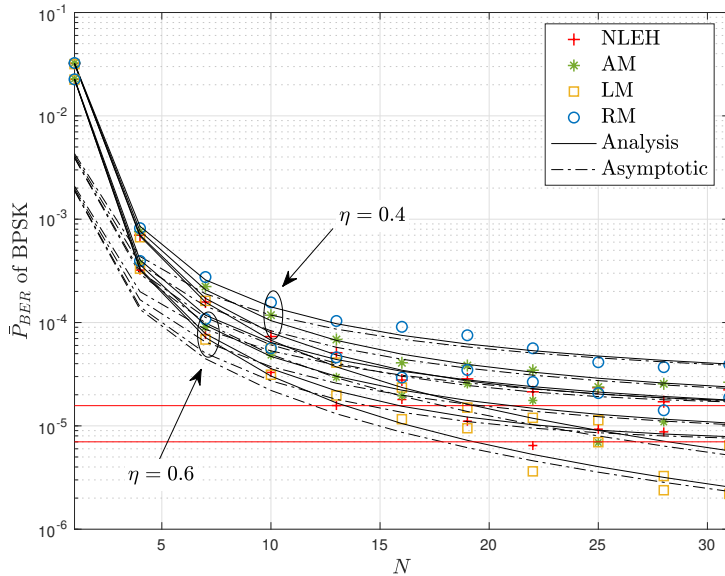
82

Figure 4.11: $\bar{P}_{BER}$ versus $N$ for $P_t = -20\,\mathrm{dBm}$, $M = 2$, and $\tau = 0.5$. The markers represent simulation points.

## 4.6  Summary

Many studies on wireless powered networks assume the linear EH model for performance analysis and resource allocation. In contrast, we proposed a new nonlinear EH model to incorporate the saturation region of practical EH circuits. It is based on the error function and has three parameters, which can be determined by a best-fit search of an experiment data set. For comparative evaluation purposes, we suggested an asymptotic model for the high transmit power regime and also described the linear as well as rational EH models.

To evaluate these models, we studied the average throughput of delay-limited and delay-tolerant transmission modes of the single-user network (Fig. 4.3) as well as average BER of BPSK and BDPSK. We also investigated the impact of large number of antennas at the PS and the impact of power control. Moreover, we investigated resource allocation for the WPCN to maximize the rate fairness under the proposed EH models. The results were validated via Monte-Carlo simulations and the four models were compared in Section 4.5.

Our main findings can be summarized as follows:

1. The newly proposed NLEH and AM models reach the saturation state, which coincides with the practical EH circuits character. The rational EH is also moderately accurate. However, the standard linear model is too optimistic in the high transmit power regime. Thus, the use of this model for design and analysis purposes should be made with abundant caution.

2. The throughput and BER performances can be improved by increasing the number of antennas at the PS, the number of antennas at the IRS and power amplifier efficiency at WD. However, for nonlinear EH models, the performance saturation will happen for large transmit powers.

# Chapter 5

# Conclusion

This thesis explored performances of wireless powered communication networks with energy harvesting. Two practical scenarios: imperfect channel state information and nonlinear energy harvesting models were considered.

In Chapter 2, the models of small-scale fading were presented. As well, existing energy harvesting models were described. The concept of high SNR analysis was also explained.

Chapter 3 investigated the impact of channel estimation errors on a multi-antenna hybrid AP and single-antenna user WPCN. We first analyzed the exact and asymptotic expressions of average throughput for delay-tolerant and delay-limit modes. Then, the closed-form and asymptotic expressions of BER/SER were derived. The results showed that in the high SNR region, the performance of one transmit and receive antenna coincided with that of multiple antennas at the AP. Since in the downlink, when the transmit power at the AP is large enough, the harvested energy at the user from one path is sufficient for the uplink data transmission.

Chapter 4 proposed a new nonlinear EH model. This model has three parameters, which can be determined by simple curve fitting with measured data. This model captures the saturation behavior of practical circuits and tightly matches with the measurement data. A simpler asymptotic version of the new nonlinear EH model was also developed. For comparative evaluation purposes, the linear and rational EH models were also described. We first compared the character of four EH models and then evaluated their perfor-

mances in a WPCN. We studied the average throughput of delay-limited mode and delay-tolerant mode as well as the average BER. The impact of a large number of antennas on the power station was also considered. The performances of nonlinear EH models had saturation states in high transmit power region. However, the linear model increased without bound as the transmit power increased.

## 5.1 Future Research Directions

Although the effect of imperfect CSI on a WPCN has been the focus of Chapter 3, several interesting future directions suggest by themselves. Firstly, our work may also be extended for non-orthogonal multiple access (NOMA) assisted WPCNs. For example, the exact and asymptotic performances of imperfect CSI can be evaluated in NOMA WPCNs. Secondly, we have assumed independent fading across the multiple AP antennas. Although this assumption roughly holds for the most practical operating conditions, correlated fading can occur sometimes. So analytical tools for the correlated fading case are important to be developed. Finally, our work can also be extended to MIMO systems.

In Chapter 4, the study of performance analysis and resource allocation for WPCNs with nonlinear/linear EH models points to several interesting future directions. Firstly, the new nonlinear and asymptotic EH models can be used to study simultaneous wireless information and power transfer systems [125]. Secondly, these new models may also be extended for EH applications of secure cooperative communications networks, secrecy performance [62], resource allocations, and full-duplex systems [7] as well. Thirdly, our system may be studied over other channel models, i.e., Nakagami-$m$, Rician, and others.

# Bibliography

[1] G. L. Stüber and G. L. Stèuber, *Principles of mobile communication*. Springer, 2017, vol. 2.

[2] M. Meraj and S. Kumar, "Evolution of mobile wireless technology from 0G to 5G," *International Journal of Computer Science and Information Technologies*, vol. 6, no. 3, pp. 2545–2551, 2015.

[3] 5Gwiki. (2020). 5g, [Online]. Available: `https://en.wikipedia.org/wiki/5G` (visited on 2020).

[4] GSMA. (2020). GSMA, [Online]. Available: `https://www.gsma.com/mobileeconomy/` (visited on 2020).

[5] comparision. (2020). Comparision, [Online]. Available: `https://its-wiki.no/images/c/c8/From_1G_to_5G_Simon.pdf` (visited on 2020).

[6] Ericsson. (2020). Ericsson Mobility Report, [Online]. Available: `https://www.ericsson.com/49da93/assets/local/mobility-report/documents/2020/june2020-ericsson-mobility-report.pdf`.

[7] M. Mohammadi, H. A. Suraweera, Y. Cao, I. Krikidis, and C. Tellambura, "Full-duplex radio for uplink/downlink wireless access with spatially random nodes," *IEEE Trans. Commun.*, vol. 63, no. 12, pp. 5250–5266, Dec. 2015.

[8] S. Atapattu, C. Tellambura, and H. Jiang, "Energy detection of primary signals over $\eta$-$\mu$ fading channels," in *Proc. 2009 International Conference on Industrial and Information Systems (ICIIS)*, IEEE, 2009, pp. 118–122.

[9] T. M. Hoang, T. Q. Duong, H. A. Suraweera, C. Tellambura, and H. V. Poor, "Cooperative beamforming and user selection for improving the security of relay-aided systems," *IEEE Trans. Commun.*, vol. 63, no. 12, pp. 5039–5051, Dec. 2015.

[10] S. P. Herath, N. Rajatheva, and C. Tellambura, "Unified approach for energy detection of unknown deterministic signal in cognitive radio over fading channels," in *Proc. 2009 IEEE International Conference on Communications Workshops*, IEEE, 2009, pp. 1–5.

[11] G. Wang, Q. Liu, R. He, F. Gao, and C. Tellambura, "Acquisition of channel state information in heterogeneous cloud radio access networks: Challenges and research directions," *IEEE Wireless Commun.*, vol. 22, no. 3, pp. 100–107, Jul. 2015.

[12] M.-L. Ku, W. Li, Y. Chen, and K. R. Liu, "Advances in energy harvesting communications: Past, present, and future challenges," *IEEE Commun. Surveys Tuts.*, vol. 18, no. 2, pp. 1384–1412, Nov. 2015.

[13] D. Niyato, D. I. Kim, M. Maso, and Z. Han, "Wireless powered communication networks: Research directions and technological approaches," *IEEE Wireless Commun.*, vol. 24, no. 6, pp. 88–97, Dec. 2017.

[14] R. Atallah, M. Khabbaz, and C. Assi, "Energy harvesting in vehicular networks: A contemporary survey," *IEEE Wireless Commun.*, vol. 23, no. 2, pp. 70–77, May 2016.

[15] X. Lu, P. Wang, D. Niyato, D. I. Kim, and Z. Han, "Wireless networks with RF energy harvesting: A contemporary survey," *IEEE Commun. Surveys Tuts.*, vol. 17, no. 2, pp. 757–789, Dec. 2014.

[16] S. Sudevalayam and P. Kulkarni, "Energy harvesting sensor nodes: Survey and implications," *IEEE Commun.Surveys Tuts.*, vol. 13, no. 3, pp. 443–461, Jul. 2010.

[17] Y. Chen, *Energy Harvesting Communications: Principles and Theories.* John Wiley & Sons, 2019.

[18] R. V. Prasad, S. Devasenapathy, V. S. Rao, and J. Vazifehdan, "Reincarnation in the ambiance: Devices and networks with energy harvesting," *IEEE Commun. Surveys Tuts.*, vol. 16, no. 1, pp. 195–213, Jul. 2013.

[19] R. Moghe, Y. Yang, F. Lambert, and D. Divan, "A scoping study of electric and magnetic field energy harvesting for wireless sensor networks in power system applications," in *Proc. 2009 IEEE Energy Conversion Congress and Exposition*, IEEE, 2009, pp. 3550–3557.

[20] V. Leonov, "Thermoelectric energy harvesting of human body heat for wearable sensors," *IEEE Sensors J.*, vol. 13, no. 6, pp. 2284–2291, Jun. 2013.

[21] M.-L. Ku, Y. Chen, and K. R. Liu, "Data-driven stochastic models and policies for energy harvesting sensor communications," *IEEE J. Sel. Areas Commun.*, vol. 33, no. 8, pp. 1505–1520, Aug. 2015.

[22] Y. He, X. Cheng, W. Peng, and G. L. Stuber, "A survey of energy harvesting communications: Models and offline optimal policies," *IEEE Commun. Mag.*, vol. 53, no. 6, pp. 79–85, Jun. 2015.

[23] T. D. P. Perera, D. N. K. Jayakody, S. K. Sharma, S. Chatzinotas, and J. Li, "Simultaneous wireless information and power transfer (SWIPT): Recent advances and future challenges," *IEEE Commun.Surveys Tuts.*, vol. 20, no. 1, pp. 264–302, Dec. 2017.

[24] R. E. Hamam, A. Karalis, J. Joannopoulos, and M. Soljačić, "Efficient weakly-radiative wireless energy transfer: An EIT-like approach," *Annals of Physics*, vol. 324, no. 8, pp. 1783–1795, May 2009.

[25] A. Kurs, A. Karalis, R. Moffatt, J. D. Joannopoulos, P. Fisher, and M. Soljačić, "Wireless power transfer via strongly coupled magnetic resonances," *science*, vol. 317, no. 5834, pp. 83–86, Aug. 2007.

[26] A. Obaid and X. Fernando, "Wireless energy harvesting from ambient sources for cognitive networks in rural communities," in *Proc. 2017 IEEE Canada International Humanitarian Technology Conference (IHTC)*, IEEE, 2017, pp. 139–143.

[27] A. S. Andrenko, X. Lin, and M. Zeng, "Outdoor rf spectral survey: A roadmap for ambient rf energy harvesting," in *Proc. TENCON 2015-2015 IEEE Region 10 Conference*, IEEE, 2015, pp. 1–4.

[28] Y. Alsaba, S. K. A. Rahim, and C. Y. Leow, "Beamforming in wireless energy harvesting communications systems: A survey," *IEEE Commun. Surveys Tuts.*, vol. 20, no. 2, pp. 1329–1360, Jan. 2018.

[29] M. Stoopman, S. Keyrouz, H. J. Visser, K. Philips, and W. A. Serdijn, "Co-design of a CMOS rectifier and small loop antenna for highly sensitive RF energy harvesters," *IEEE J. Solid-State Circuits*, vol. 49, no. 3, pp. 622–634, Mar. 2014.

[30] M. Stoopman, S. Keyrouz, H. Visser, K. Philips, and W. Serdijn, "A self-calibrating rf energy harvester generating 1V at- 26.3 dBm," in *Proc. 2013 Symposium on VLSI Circuits*, IEEE, 2013, pp. C226–C227.

[31] Powercast. (2020). Powercast product, [Online]. Available: `https://www.powercastco.com/documentation/`.

[32] P. Grover and A. Sahai, "Shannon meets tesla: Wireless information and power transfer," in *Proc. 2010 IEEE international symposium on information theory*, IEEE, 2010, pp. 2363–2367.

[33] H. Ju and R. Zhang, "Throughput maximization in wireless powered communication networks," *IEEE Trans. Wireless Commun.*, vol. 13, no. 1, pp. 418–428, Dec. 2013.

[34] G. Pan, H. Lei, and Y. Deng, "On secrecy performance of MISO SWIPT systems with TAS and imperfect CSI," *IEEE Wireless Commun.*, vol. 64, no. 3, pp. 3831–3843, Sep. 2016.

[35] K. S. Ahn, S.-W. Choi, and J.-M. Ahn, "Secrecy performance of maximum ratio diversity with channel estimation error," *IEEE Signal Process. Lett.*, vol. 22, no. 11, pp. 2167–2171, Nov. 2015.

[36] Z. Chu, F. Zhou, Z. Zhu, M. Sun, and N. Al-Dhahir, "Energy beam-forming design and user cooperation for wireless powered communication networks," *IEEE Wireless Commun. Lett.*, vol. 6, no. 6, pp. 750–753, Dec. 2017.

[37] W. Huang, H. Chen, Y. Li, and B. Vucetic, "On the performance of multi-antenna wireless-powered communications with energy beam-forming," *IEEE Trans. Veh. Technol.*, vol. 65, no. 3, pp. 1801–1808, Mar. 2016. DOI: `10.1109/tvt.2015.2412532`.

[38] S. Atapattu, C. Tellambura, and H. Jiang, "A mixture gamma distribution to model the SNR of wireless channels," *IEEE Trans. Wireless Commun.*, vol. 10, no. 12, pp. 4193–4203, Oct. 2011.

[39] P. Piantanida, G. Matz, and P. Duhamel, "Outage behavior of discrete memoryless channels under channel estimation errors," *IEEE Trans. Inf. Theory*, vol. 55, no. 9, pp. 4221–4239, Sep. 2009.

[40] L. Liu, R. Zhang, and K.-C. Chua, "Multi-antenna wireless powered communication with energy beamforming," *IEEE Trans. Commun.*, vol. 62, no. 12, pp. 4349–4361, Dec. 2014.

[41] Y. Ma, H. Chen, Z. Lin, Y. Li, and B. Vucetic, "Distributed and optimal resource allocation for power beacon-assisted wireless-powered communications," *IEEE Trans. Wireless Commun.*, vol. 63, no. 10, pp. 3569–3583, Oct. 2015.

[42] E. Boshkovska, D. W. K. Ng, N. Zlatanov, and R. Schober, "Practical non-linear energy harvesting model and resource allocation for SWIPT systems," *IEEE Wireless Commun. Lett.*, vol. 19, no. 12, pp. 2082–2085, Dec. 2015.

[43] D. Khan, S. J. Oh, K. Shehzad, M. Basim, D. Verma, Y. G. Pu, M. Lee, K. C. Hwang, Y. Yang, and K.-Y. Lee, "An efficient reconfigurable RF-DC converter with wide input power range for RF energy harvesting," *IEEE Access*, Apr. 2020.

[44] Z. Hameed and K. Moez, "Hybrid forward and backward threshold-compensated RF-DC power converter for RF energy harvesting," *IEEE Trans. Emerg. Sel. Topics Circuits Syst.*, vol. 4, no. 3, pp. 335–343, Sep. 2014.

[45] J. G. Proakis and M. Salehi, *Digital communications*. McGraw-hill New York, 2001, vol. 4.

[46] B. Lyu, T. Qi, H. Guo, and Z. Yang, "Throughput maximization in full-duplex dual-hop wireless powered communication networks," *IEEE Access*, vol. 7, pp. 158 584–158 593, Oct. 2019.

[47] Y. Liu, "Wireless information and power transfer for multirelay-assisted cooperative communication," *IEEE Communications Letters*, vol. 20, no. 4, pp. 784–787, Apr. 2016.

[48] T. Le, K. Mayaram, and T. Fiez, "Efficient far-field radio frequency energy harvesting for passively powered sensor networks," *IEEE J. Solid-State Circuits*, vol. 43, no. 5, pp. 1287–1302, Apr. 2008.

[49] Y. Dong, M. J. Hossain, and J. Cheng, "Performance of wireless powered amplify and forward relaying over Nakagami-$m$ fading channels with nonlinear energy harvester," *IEEE Commun. Lett.*, vol. 20, no. 4, pp. 672–675, Feb. 2016.

[50] Y. Chen, K. T. Sabnis, and R. A. Abd-Alhameed, "New formula for conversion efficiency of RF EH and its wireless applications," *IEEE Trans. Veh. Technol.*, vol. 65, no. 11, pp. 9410–9414, Jan. 2016.

[51] Y. Chen, N. Zhao, and M.-S. Alouini, "Wireless energy harvesting using signals from multiple fading channels," *IEEE Trans. Wireless Commun.*, vol. 65, no. 11, pp. 5027–5039, Nov. 2017. DOI: `10.1109/tcomm.2017.2734665`.

[52] S. Wang, M. Xia, K. Huang, and Y.-C. Wu, "Wirelessly powered two-way communication with nonlinear energy harvesting model: Rate regions under fixed and mobile relay," *IEEE Trans. Wireless Commun.*, vol. 16, no. 12, pp. 8190–8204, Apr. 2017.

[53] Z. Wang and G. Giannakis, "A simple and general parameterization quantifying performance in fading channels," *IEEE Trans. Wireless Commun.*, vol. 51, no. 8, pp. 1389–1398, Aug. 2003.

[54] L. Zheng and D. N. C. Tse, "Diversity and multiplexing: A fundamental tradeoff in multiple-antenna channels," *IEEE Trans. Inf. Theory*, vol. 49, no. 5, pp. 1073–1096, 2003.

[55] D. Tse and P. Viswanath, *Fundamentals of wireless communication.* Cambridge university press, 2005.

[56] Y. Dhungana and C. Tellambura, "New simple approximations for error probability and outage in fading," *IEEE Trans. Wireless Commun.*, vol. 16, no. 11, pp. 1760–1763, Oct. 2012.

[57] ——, "Uniform approximations for wireless performance in fading channels," *IEEE Trans. Wireless Commun.*, vol. 61, no. 11, pp. 4768–4779, Nov. 2013.

[58] V. R. S. Banjade, C. Tellambura, and H. Jiang, "Asymptotic performance of energy detector in fading and diversity reception," *IEEE Trans. Wireless Commun.*, vol. 63, no. 6, pp. 2031–2043, Jun. 2015.

[59] S. Ulukus, A. Yener, E. Erkip, O. Simeone, M. Zorzi, P. Grover, and K. Huang, "Energy harvesting wireless communications: A review of recent advances," *IEEE J. Sel. Areas Commun.*, vol. 33, no. 3, pp. 360–381, Jan. 2015.

[60] S. Bi, Y. Zeng, and R. Zhang, "Wireless powered communication networks: An overview," *IEEE Wireless Commun.*, vol. 23, no. 2, pp. 10–18, May 2016.

[61] M. A. Hossain, R. M. Noor, K.-L. A. Yau, *et al.*, "A survey on simultaneous wireless information and power transfer with cooperative relay and future challenges," *IEEE Access*, vol. 7, pp. 19 166–19 198, Feb. 2019.

[62] Z. Mobini, M. Mohammadi, and C. Tellambura, "Wireless-powered full-duplex relay and friendly jamming for secure cooperative communications," *IEEE Trans. Inf. Forensics Security*, vol. 14, no. 3, pp. 621–634, Jul. 2018.

[63] N. Deepan and B. Rebekka, "On the performance of wireless powered communication networks over generalized $\kappa$ - $\mu$ fading channels," *Physical Communication*, vol. 36, p. 100 759, Oct. 2019.

[64] Y. Gao, Y. Chen, Y. Zhou, and N. Cao, "BER and achievable rate analysis of wireless powered communications with correlated uplink and downlink," *IET Commun.*, vol. 12, no. 3, pp. 310–316, Feb. 2017.

[65] A. Almradi, "Information and energy beamforming in MIMO wireless powered systems," in *Proc. IEEE Global Commun. Conf. (GLOBECOM)*, 2016, pp. 1–7.

[66] X. Chen, X. Wang, and X. Chen, "Energy-efficient optimization for wireless information and power transfer in large-scale MIMO systems employing energy beamforming," *IEEE Commun. Lett.*, vol. 2, no. 6, pp. 667–670, Oct. 2013.

[67] G. Wang, F. Gao, Y.-C. Wu, and C. Tellambura, "Joint CFO and channel estimation for OFDM-based two-way relay networks," *IEEE Trans. Wireless Commun.*, vol. 10, no. 2, pp. 456–465, Dec. 2010.

[68] S. Schiessl, H. Al-Zubaidy, M. Skoglund, and J. Gross, "Delay performance of wireless communications with imperfect CSI and finite-length coding," *IEEE Trans. Wireless Commun.*, vol. 66, no. 12, pp. 6527–6541, Jul. 2018.

[69] M. J. Gans, "The effect of Gaussian error in maximal ratio combiners," *IEEE Wireless Commun.*, vol. 19, no. 4, pp. 492–500, Aug. 1971.

[70] B. R. Tomiuk, N. C. Beaulieu, and A. A. Abu-Dayya, "General forms for maximal ratio diversity with weighting errors," *IEEE Trans. Commun.*, vol. 47, no. 4, pp. 488–492, Apr. 1999.

[71] Z. Chang, Z. Wang, X. Guo, Z. Han, and T. Ristaniemi, "Energy-efficient resource allocation for wireless powered massive MIMO system with imperfect CSI," *IEEE Trans. Green Commun. Netw.*, vol. 1, no. 2, pp. 121–130, Apr. 2017.

[72] Y. Huang, P. Zhang, Q. Wu, and J. Wang, "Secrecy performance of wireless powered communication networks with multiple eavesdroppers and outdated CSI," *IEEE Access*, vol. 6, pp. 33 774–33 788, May 2018.

[73] Y. Wu, X. Chen, C. Yuen, and C. Zhong, "Robust resource allocation for secrecy wireless powered communication networks," *IEEE Commun. Lett.*, vol. 20, no. 12, pp. 2430–2433, Sep. 2016.

[74] F. Zhao, H. Lin, C. Zhong, Z. Hadzi-Velkov, G. K. Karagiannidis, and Z. Zhang, "On the capacity of wireless powered communication systems over Rician fading channels," *IEEE Trans. Commun.*, vol. 66, no. 1, pp. 404–417, Sep. 2017.

[75] G. Yang, C. K. Ho, R. Zhang, and Y. L. Guan, "Throughput optimization for massive MIMO systems powered by wireless energy transfer," *IEEE J. Sel. Areas Commun.*, vol. 33, no. 8, pp. 1640–1650, Jan. 2015.

[76] H. Liang, C. Zhong, X. Chen, H. A. Suraweera, and Z. Zhang, "Wireless powered dual-hop multi-antenna relaying systems: Impact of CSI and antenna correlation," *IEEE Trans. Wireless Commun.*, vol. 16, no. 4, pp. 2505–2519, Mar. 2017.

[77] J. Zhang and G. Pan, "Outage analysis of wireless-powered relaying MIMO systems with non-linear energy harvesters and imperfect CSI," *IEEE Access*, vol. 4, pp. 7046–7053, Oct. 2016.

[78] J. Ye, H. Lei, and Y. Liu, "Cooperative communications with wireless energy harvesting over Nakagami-m fading channels," *IEEE Trans. Wireless Commun.*, vol. 65, no. 12, pp. 5149–5164, Aug. 2017.

[79] Y. Liu, K.-W. Chin, and C. Yang, "Uplinks schedulers for RF-energy harvesting networks with imperfect CSI," *IEEE Trans. Veh. Technol.*, vol. 69, no. 4, pp. 4233–4245, Jan. 2020.

[80] X. Liu, Y. Gao, M. Guo, and N. Sha, "Secrecy throughput optimization for the WPCNs with non-linear EH model," *IEEE Access*, vol. 7, pp. 59 477–59 490, May 2019.

[81] I. S. Gradshteyn and I. M. Ryzhik, *Table of Integrals, Series, and Products, 7th edition*. Academic Press, 2007.

[82] M. Taghadosi, L. Albasha, N. A. Quadir, Y. A. Rahama, and N. Qaddoumi, "High efficiency energy harvesters in 65nm CMOS process for autonomous IoT sensor applications," *IEEE Access*, vol. 6, pp. 2397–2409, Dec. 2017.

[83] B. M. Hochwald, T. L. Marzetta, and V. Tarokh, "Multiple-antenna channel hardening and its implications for rate feedback and scheduling," *IEEE Trans. Inf. Theory*, vol. 50, no. 9, pp. 1893–1909, Aug. 2004.

[84] T. L. Marzetta, *Fundamentals of massive MIMO*. Cambridge University Press, 2016.

[85]  K. Huang and V. K. N. Lau, "Enabling wireless power transfer in cellular networks: Architecture, modeling and deployment," *IEEE Trans. Wireless Commun.*, vol. 13, no. 2, pp. 902–912, Feb. 2014. DOI: `10.1109/twc.2013.122313.130727`.

[86]  I. Chatzigeorgiou, "Bounds on the Lambert function and their application to the outage analysis of user cooperation," *IEEE Wireless Commun. Lett.*, vol. 17, no. 8, pp. 1505–1508, Aug. 2013.

[87]  S.-N. Jin, D.-W. Yue, and H. H. Nguyen, "Power scaling laws of massive MIMO full-duplex relaying with hardware impairments," *IEEE Access*, vol. 6, pp. 40 860–40 882, Jul. 2018.

[88]  S. Silva, G. A. A. Baduge, M. Ardakani, and C. Tellambura, "Performance analysis of massive MIMO two-way relay networks with pilot contamination, imperfect CSI, and antenna correlation," *IEEE Trans. Veh. Technol.*, vol. 67, no. 6, pp. 4831–4842, Mar. 2018.

[89]  P. S. Bithas, N. C. Sagias, and P. T. Mathiopoulos, "On the performance analysis of digital communications over generalized-K fading channels," *IEEE Wireless Commun. Lett.*, vol. 10, no. 5, pp. 353–355, May 2006. DOI: `10.1109/lcomm.2006.1633320`.

[90]  C. Tellambura, "Evaluation of the exact union bound for trellis-coded modulations over fading channels," *IEEE Trans. Commun.*, vol. 44, no. 12, pp. 1693–1699, Dec. 1996.

[91]  C. Tellambura and A. J. Mueller and V. K. Bhargava, "Analysis of M-ary phase-shift keying with diversity reception for land-mobile satellite channels," *IEEE Trans. Veh. Technol.*, vol. 46, pp. 910–922, Nov. 1997.

[92]  H. Shin and J. H. Lee, "Performance analysis of space–time block codes over keyhole Nakagami-$m$ fading channels," *IEEE Trans. Veh. Technol.*, vol. 53, no. 2, pp. 351–362, Mar. 2004.

[93]  Y. Chen and C. Tellambura, "Distribution functions of selection combiner output in equally correlated Rayleigh, Rician, and Nakagami-$m$ fading channels," *IEEE Trans. Commun.*, vol. 52, no. 11, pp. 1948–1956, Nov. 2004. DOI: `10.1109/tcomm.2004.836596`.

[94]  H. Lei, Y. Zhang, K.-H. Park, I. S. Ansari, G. Pan, and M.-S. Alouini, "Performance analysis of dual-hop RF-UWOC systems," *IEEE Photon. J.*, vol. 12, no. 2, pp. 1–15, Mar. 2020.

[95]  Cisco. (2020). Cisco annual report 2018-2023, [Online]. Available: `https://www.cisco.com/c/en/us/solutions/collateral/executive-perspectives/annual-internet-report/white-paper-c11-741490.html`.

[96]   P. D. Diamantoulakis, K. N. Pappi, G. K. Karagiannidis, H. Xing, and A. Nallanathan, "Joint downlink/uplink design for wireless powered networks with interference," *IEEE Access*, vol. 5, pp. 1534–1547, Sep. 2017.

[97]   I. Pehlivan and S. C. Ergen, "Scheduling of energy harvesting for MIMO wireless powered communication networks," *IEEE Commun. Lett.*, vol. 23, no. 1, pp. 152–155, Nov. 2018.

[98]   Y. Chen, "Energy-harvesting AF relaying in the presence of interference and Nakagami-*m* fading," *IEEE Trans. Wireless Commun.*, vol. 15, no. 2, pp. 1008–1017, Sep. 2015.

[99]   C. Guo, B. Liao, L. Huang, Q. Li, and X. Lin, "Convexity of fairness-aware resource allocation in wireless powered communication networks," *IEEE Commun. Lett.*, vol. 20, no. 3, pp. 474–477, Jan. 2016.

[100]  D. Altinel and G. K. Kurt, "Energy harvesting from multiple RF sources in wireless fading channels," *IEEE Trans. Veh. Technol.*, vol. 65, no. 11, pp. 8854–8864, Jan. 2016.

[101]  H. Gonçalves, M. Martins, and J. Fernandes, "Fully integrated energy harvesting circuit with- 25-dBm sensitivity using transformer matching," *IEEE Trans. Circuits Syst. II*, vol. 62, no. 5, pp. 446–450, Jan. 2015.

[102]  S. Ladan and K. Wu, "Nonlinear modeling and harmonic recycling of millimeter-wave rectifier circuit," *IEEE Trans. Microw. Theory Techn.*, vol. 63, no. 3, pp. 937–944, Feb. 2015.

[103]  J. Guo and X. Zhu, "An improved analytical model for RF-DC conversion efficiency in microwave rectifiers," in *Proc. 2012 IEEE/MTT-S International Microwave Symposium Digest*, IEEE, 2012, pp. 1–3.

[104]  S. Pejoski, Z. Hadzi-Velkov, and R. Schober, "Optimal power and time allocation for WPCNs with piece-wise linear EH model," *IEEE Commun. Lett.*, vol. 7, no. 3, pp. 364–367, Nov. 2017.

[105]  K. Xiong, B. Wang, and K. R. Liu, "Rate-energy region of SWIPT for MIMO broadcasting under nonlinear energy harvesting model," *IEEE Trans. Wireless Commun.*, vol. 16, no. 8, pp. 5147–5161, May 2017.

[106]  H. Lyu, X. Liu, Y. Sun, Z. Jian, and A. Babakhani, "A 915-MHz far-field energy harvester with- 22-dBm sensitivity and 3-V output voltage based on antenna-and-rectifier codesign," *IEEE Microw. Wireless Compon. Lett.*, vol. 29, no. 8, pp. 557–559, Jul. 2019.

[107]  B. Clerckx and E. Bayguzina, "Waveform design for wireless power transfer," *IEEE Trans. Signal Process.*, vol. 64, no. 23, pp. 6313–6328, Aug. 2016.

[108] J. Zhang and G. Pan, "Outage analysis of wireless-powered relaying MIMO systems with non-linear energy harvesters and imperfect CSI," *IEEE Access*, vol. 4, pp. 7046–7053, Oct. 2016.

[109] R. Jiang, K. Xiong, P. Fan, L. Zhou, and Z. Zhong, "Outage probability and throughput of multirelay SWIPT-WPCN networks with nonlinear EH model and imperfect CSI," *IEEE Syst. J.*, Oct. 2019.

[110] J. Zhang, G. Pan, and Y. Xie, "Secrecy analysis of wireless-powered multi-antenna relaying system with nonlinear energy harvesters and imperfect CSI," *IEEE Trans. Green Commun. Netw.*, vol. 2, no. 2, pp. 460–470, Dec. 2017.

[111] Y. Huang, T. Q. Duong, J. Wang, and P. Zhang, "Performance of multi-antenna wireless-powered communications with nonlinear energy harvester," in *Proc. 2017 IEEE 86th Vehicular Technology Conference (VTC-Fall)*, IEEE, 2017, pp. 1–6.

[112] Y. Wang, Y. Wu, F. Zhou, Z. Chu, Y. Wu, and F. Yuan, "Multi-objective resource allocation in a NOMA cognitive radio network with a practical non-linear energy harvesting model," *IEEE Access*, vol. 6, pp. 12 973–12 982, Dec. 2017.

[113] Y. Wang, Y. Wang, F. Zhou, Y. Wu, and H. Zhou, "Resource allocation in wireless powered cognitive radio networks based on a practical non-linear energy harvesting model," *IEEE Access*, vol. 5, pp. 17 618–17 626, Jun. 2017.

[114] R. Morsi, E. Boshkovska, E. Ramadan, D. W. K. Ng, and R. Schober, "On the performance of wireless powered communication with non-linear energy harvesting," in *Proc. 2017 IEEE 18th international workshop on signal processing advances in wireless communications (SPAWC)*, IEEE, 2017, pp. 1–5.

[115] L. Cantos and Y. H. Kim, "Max-min fair energy beamforming for wireless powered communication with non-linear energy harvesting," *IEEE Access*, vol. 7, pp. 69 516–69 523, May 2019.

[116] X. Zhang, Y. Wang, F. Zhou, N. Al-Dhahir, and X. Deng, "Robust resource allocation for MISO cognitive radio networks under two practical non-linear energy harvesting models," *IEEE Commun. Lett.*, vol. 22, no. 9, pp. 1874–1877, Jun. 2018.

[117] X. Chen, C. Yuen, and Z. Zhang, "Wireless energy and information transfer tradeoff for limited-feedback multiantenna systems with energy beamforming," *IEEE Trans. Veh. Technol.*, vol. 63, no. 1, pp. 407–412, Jul. 2013.

[118] Z. Chang, S. Zhang, and Z. Wang, "Energy efficient optimisation for large-scale multiple-antenna system with WPT," *IET Commun.*, vol. 12, no. 5, pp. 552–558, Mar. 2018.

[119] W. Zhao, G. Wang, S. Atapattu, C. Tellambura, and H. Guan, "Outage analysis of ambient backscatter communication systems," *IEEE Commun. Lett.*, vol. 22, no. 8, pp. 1736–1739, Jun. 2018.

[120] IEEE. (2020). IEEE 802.15.4, [Online]. Available: `http://www.ieee802.org/15/pub/TG4.html`.

[121] ——, (2020). IEEE 802.11-1999, [Online]. Available: `https://standards.ieee.org/standard/802.11-1999.html`.

[122] H. Lei, J. Zhang, K.-H. Park, P. Xu, Z. Zhang, G. Pan, and M.-S. Alouini, "Secrecy outage of max–min TAS scheme in MIMO-NOMA systems," vol. 67, no. 8, pp. 6981–6990, Apr. 2018.

[123] F. Rezaei, C. Tellambura, A. Tadaion, and A. R. Heidarpour, "Rate analysis of cell-free massive MIMO-NOMA with three linear precoders," *IEEE Trans. Commun.*, Mar. 2020.

[124] C. Zhang, Y. Jing, Y. Huang, and L. Yang, "Performance scaling law for multicell multiuser massive MIMO," *IEEE Trans. Veh. Technol.*, vol. 66, no. 11, pp. 9890–9903, Jul. 2017.

[125] G. Pan, H. Lei, Y. Yuan, and Z. Ding, "Performance analysis and optimization for SWIPT wireless sensor networks," *IEEE Trans. Commun.*, vol. 65, no. 5, pp. 2291–2302, Mar. 2017.

[126] W. Gautschi, *Orthogonal polynomials.* Oxford university press Oxford, 2004.

[127] J. A. Gubner, "A new formula for lognormal characteristic functions," *IEEE Trans. Veh. Technol.*, vol. 55, no. 5, pp. 1668–1671, Sep. 2006.

[128] M.-S. Alouini and A. J. Goldsmith, "Capacity of Rayleigh fading channels under different adaptive transmission and diversity-combining techniques," *IEEE Trans. Veh. Technol.*, vol. 48, no. 4, pp. 1165–1181, Jul. 1999.

# Appendix A

# Proofs for Chapter 3

## A.1  Proof of Proposition 1

To develop this analysis, we must go back to the definition of $\gamma_A$. By using it and revisiting (3.22), we can exactly express the delay-limited throughput as

$$P_{out} = \Pr\left(XY < \frac{(1-\tau)\,\gamma_{th}}{\tau\eta\overline{\gamma}}\right). \tag{A.1}$$

As mentioned before, to find the asymptotics of the outage, we need the series expansion of the PDF of $XY$, similar to (2.9). We then have to consider the behaviour of $K_n(x)$ as $x \to 0$. But the expansion of this function near $x = 0$ has logarithmic terms and negative powers of $x$ [81]. Due to this reason, the classical approach is not viable. Alternatively, we use the two-step process, which was earlier used to derived the asymptotic MGF. The first step is to average over $X$ while keeping $Y$ constant. Since the PDF of $X$ is a weight sum (3.5), the outage for conditioned on $Y$, $P_{out}\,|_Y$, may then be written as

$$P_{out}\,|_Y = \sum_{n=1}^{N} A\,(n)\,\Gamma\,(n)\left[1 - e^{-\frac{\Delta}{y}}\sum_{l=0}^{n-1}\left(\frac{\Delta}{y}\right)^l\frac{1}{l!}\right]. \tag{A.2}$$

The second step is to average the conditional outage over the PDF of $Y$

when $\bar{\gamma} \to \infty$. This can be done as follows:

$$
\begin{aligned}
P_{out} &= \int_0^\infty P_{out} \mid_Y f_Y(y) \, dy \\
&\stackrel{(a)}{=} \sum_{n=1}^N \sum_{m=1}^N B(m,n) \Gamma(n) \int_0^\infty \underbrace{\left[ 1 - e^{-\frac{\Delta}{y}} \sum_{l=0}^{n-1} \left( \frac{\Delta}{y} \right)^l \frac{1}{l!} \right]}_{I} y^{m-1} e^{-y} dy \quad (\text{A.3}) \\
&\stackrel{(b)}{=} 2 \sum_{n=1}^N \sum_{m=1}^N B(m,n) \Delta^{\frac{m+n}{2}} K_{n-m} \left( 2\sqrt{\Delta} \right),
\end{aligned}
$$

where Step (a) is obtained by substituting the PDF of $Y$ in (A.2); The proof of Step (b) is obtained in the Appendix A.2.

Therefore, the average throughput can be written as (3.24).

## A.2 Approximation for OP

Here, we derive the approximation expression of the term in Step (a) in (A.3). Recall that $\Delta = \frac{\gamma_{th}(1-\tau)}{\tau \eta \bar{\gamma}}$, so when $\bar{\gamma} \to \infty$, $\Delta \to 0$ and $I$ can be approximated as

$$
\begin{aligned}
I &= 1 - e^{-\frac{\Delta}{y}} \sum_{l=0}^{n-1} \left( \frac{\Delta}{y} \right)^l \frac{1}{l!} \\
&\stackrel{(a)}{=} e^{-\frac{\Delta}{y}} \left[ e^{\frac{\Delta}{y}} - \sum_{l=0}^{n-1} \left( \frac{\Delta}{y} \right)^l \frac{1}{l!} \right] \\
&\stackrel{(b)}{=} e^{-\frac{\Delta}{y}} \sum_{l=n}^\infty \left( \frac{\Delta}{y} \right)^l \frac{1}{l!} \\
&\stackrel{(c)}{\approx} e^{-\frac{\Delta}{y}} \left( \frac{\Delta}{y} \right)^n \frac{1}{n!},
\end{aligned}
\quad (\text{A.4})
$$

where, (a) follows readily; (b) is due to Taylor expansion $e^{\frac{\Delta}{y}} = \sum_{l=0}^\infty \left( \frac{\Delta}{y} \right)^l \frac{1}{l!}$; When $\Delta \to 0$, the terms for $l \geq n+1$ are much smaller than the $l = n$-th term, so we can ignore all the terms for which $l \geq n+1$. Therefore, we obtain (c).

The integral in Step (a) in (A.3) can be approximated as

$$
\int_0^\infty \left[ 1 - e^{-\frac{\Delta}{y}} \sum_{l=0}^{n-1} \left(\frac{\Delta}{y}\right)^l \frac{1}{l!} \right] y^{m-1} e^{-y} dy
$$

$$
\approx \Delta^n \frac{1}{n!} \int_0^\infty e^{-\frac{\Delta}{y} - y} y^{m-n-1} dy \tag{A.5}
$$

$$
= \Delta^{\frac{m+n}{2}} K_{n-m} \left(2\sqrt{\Delta}\right),
$$

which is obtained by using [81, Eq. (3.471.9)]. By substituting this in (A.3), we obtain the final result.

## A.3  Proof of Proposition 2

For the imperfect CSI case, where $0 \le \rho < 1$, when SNR is large, the first term of (A.3) will be the dominant term, and thus the whole sum in (A.3) can be approximated by it. For the term with $m = 1$ and $n = 1$, equation (b) in (A.3) can be written as

$$
P_{out} \approx 2 \left(1 - \rho^2\right)^{2(N-1)} \Delta K_0 \left(2\sqrt{\Delta}\right)
$$

$$
\overset{(a)}{=} 2 \left(1 - \rho^2\right)^{2(N-1)} \Delta \left(-\frac{1}{2} \ln \Delta - \gamma_{EM}\right) + O\left(\Delta^2\right). \tag{A.6}
$$

$$
\overset{(b)}{=} \left(1 - \rho^2\right)^{2(N-1)} \left( \ln\left(\frac{c\overline{\gamma}}{\gamma_{th}}\right) - 2\gamma_{EM} \right) \frac{\gamma_{th}}{c\overline{\gamma}}
$$

To obtain (a), we note that near $x = 0$, the Bessel function can be expanded as $K_0 \left(2\sqrt{x}\right) = -\frac{1}{2} \ln x - \gamma_{EM} + O\left(x\right)$. We can use this expansion because as $\overline{\gamma} \to \infty$, $\Delta \to 0$. (b) represents the equation in $\overline{\gamma}$.

Therefore, the average throughput is expressed as

$$
R_{DL} = R^* \left[ 1 - \left(1 - \rho^2\right)^{2(N-1)} \left( \ln\left(\frac{c\overline{\gamma}}{\gamma_{th}}\right) - 2\gamma_{EM} \right) \frac{\gamma_{th}}{c\overline{\gamma}} \right]. \tag{A.7}
$$

For the perfect CSI case, when $\rho = 1$, $B\left(m, n\right)$ exists only when $m = N$ and $n = N$, so (A.3) can be written as

$$
P_{out} \approx \frac{2}{\Gamma^2\left(N\right)} \Delta^N K_0 \left(2\sqrt{\Delta}\right)
$$

$$
\overset{(a)}{=} \frac{2}{\Gamma^2\left(N\right)} \Delta^N \left(-\frac{1}{2} \ln \Delta - \gamma_{EM}\right) + O\left(\Delta^{N+1}\right) \tag{A.8}
$$

$$
\overset{(b)}{\approx} \frac{1}{\Gamma^2\left(N\right)} \left( \ln\left(\frac{c\overline{\gamma}}{\gamma_{th}}\right) - 2\gamma_{EM} \right) \left(\frac{\gamma_{th}}{c\overline{\gamma}}\right)^N.
$$

The proof of this is very similar to that of (A.6) and therefore the details are omitted. Thus, the average throughput can be expressed as

$$R_{DL} = R^* \left[ 1 - \frac{1}{\Gamma^2(N)} \left( \ln \left( \frac{c\bar{\gamma}}{\gamma_{\text{th}}} \right) - 2\gamma_{EM} \right) \left( \frac{\gamma_{\text{th}}}{c\bar{\gamma}} \right)^N \right]. \tag{A.9}$$

## A.4  Proof of Proposition 6

First, we show the BER by the Q function, and then take the expectation for the BER to obtain the average BER. Therefore, the BER of BPSK can be calculated as

$$\bar{P}_{BER} = \mathbb{E} \left[ Q \left( \sqrt{2c\bar{\gamma}XY} \right) \right], \tag{A.10}$$

where the Gaussian Q-function is given by $Q(x) = \frac{1}{\sqrt{2\pi}} \int_x^\infty e^{-t^2/2} dt = \frac{1}{2\sqrt{\pi}} \Gamma\left( \frac{1}{2}, \frac{x^2}{2} \right)$. Therefore, (A.10) can be rewritten as

$$\bar{P}_{BER} = \mathbb{E} \left[ \frac{1}{2\sqrt{\pi}} \Gamma\left( \frac{1}{2}, c\bar{\gamma}XY \right) \right]. \tag{A.11}$$

Next, we use two steps to find the asymptotic BER.

In Step 1, we average (A.11) over $X$ while keeping $Y$ constant. Since the PDF of $X$ is a weighted sum of exponential terms (3.5), the BER conditional on $Y$ may be written as

$$\begin{aligned}
\bar{P}_{BER|Y} &= \sum_{n=1}^N \frac{A(n)}{2\sqrt{\pi}} \int_0^\infty \Gamma\left( \frac{1}{2}, c\bar{\gamma}xy \right) x^{n-1} e^{-x} dx \\
&\stackrel{(a)}{=} \sum_{n=1}^N \frac{A(n)}{2n\sqrt{\pi}} \frac{\sqrt{c\bar{\gamma}y}\, \Gamma\left( n + \frac{1}{2} \right)}{(1 + c\bar{\gamma}y)^{n+\frac{1}{2}}} {}_2F_1\left( 1, n + \frac{1}{2}; n+1; \frac{1}{1+c\bar{\gamma}y} \right) \\
&\stackrel{(b)}{\approx} \sum_{n=1}^N \frac{A(n)}{2n\sqrt{\pi}} \frac{\Gamma\left( n + \frac{1}{2} \right)}{(1 + c\bar{\gamma}y)^n} \\
&\stackrel{(c)}{\approx} \frac{1}{4} \frac{1}{1 + c\bar{\gamma}y}.
\end{aligned} \tag{A.12}$$

Step (a) is obtained by calculating the integral part of the conditional BER given by $Y$ and using [81, Eq. (6.455.1)]; ${}_2F_1(a, b; c; z)$ is hypergeometric function [81, Eq. (9.10)] which can be written by the power series when $|z| < 1$. ${}_2F_1(a, b; c; z) = \sum_{k=0}^\infty \frac{(a)_k (b)_k}{(c)_k} \frac{z^k}{k!}$, where if $k = 0$, $(q)_k = 1$ and if $k > 0$,

101

$(q)_k = q\,(q+1)\cdots(q+k-1)$. In step (b), since $\bar{\gamma} \to \infty$, the parts for which $n \geq 2$ is small compared to those with $n = 1$, so the parts for $n \geq 0$ can be omitted. After some algebraic manipulations, we get (c).

Step 2: we average the conditional BER over $Y$. The BER of BPSK may then be written as follows:

$$
\begin{aligned}
\bar{P}_{BER} &= \sum_{m=1}^{N} \frac{B\,(m,1)}{4} \int_0^\infty \frac{1}{1+c\bar{\gamma}y} y^{m-1} e^{-y} dy \\
&= \sum_{m=1}^{N} \frac{B\,(m,1)}{4c\bar{\gamma}} \left[ (-1)^{m-2} \left(\frac{1}{c\bar{\gamma}}\right)^{m-1} e^{\frac{1}{c\bar{\gamma}}} E_i\left(-\frac{1}{c\bar{\gamma}}\right) \right. \\
&\quad \left. + \sum_{k=1}^{m-1} \Gamma\,(k) \left(-\frac{1}{c\bar{\gamma}}\right)^{m-k-1} \right],
\end{aligned}
\tag{A.13}
$$

where the integral is obtained by [81, Eq. (3.353.5)].

## A.5  Proof of Proposition 7

To this end, we can further simplify the asymptotic result in (A.13). When the CSI is imperfect, $0 \leq \rho < 1$, the dominant part occurs when the number of antennas equals to one. Thus, only keeping the dominant part, we find

$$
\begin{aligned}
\bar{P}_{BER} &\approx \frac{(1-\rho^2)^{2(N-1)}}{4} \int_0^\infty \frac{e^{-y}}{1+c\bar{\gamma}y} dy \\
&\approx \frac{(1-\rho^2)^{2(N-1)}}{4} (c\bar{\gamma})^{-1} \left[\ln c\bar{\gamma} - \gamma_{EM}\right].
\end{aligned}
\tag{A.14}
$$

The derivation follows from Corollary 3.

When the CSI is estimated perfectly, $\rho = 1$, the value of $B\,(m,n)$ is not zero only when $m = N$ and $n = N$, so (A.12) can be further simplified as

$$
\bar{P}_{BER|Y} \approx \frac{A\,(N)}{2N\sqrt{\pi}} \frac{\Gamma\left(N + \frac{1}{2}\right)}{(1+c\bar{\gamma}y)^N}.
\tag{A.15}
$$

By averaging this over the PDF of $Y$, we get

$$
\begin{aligned}
\bar{P}_{BER} &= \frac{\Gamma\left(N + \frac{1}{2}\right)}{2N\sqrt{\pi}\,\Gamma^2\,(N)} \int_0^\infty \frac{y^{N-1}e^{-y}}{(1+c\bar{\gamma}y)^N} dy \\
&\overset{(a)}{=} \frac{\Gamma\left(N + \frac{1}{2}\right)}{2N\sqrt{\pi}\,\Gamma\,(N)\,(tc\bar{\gamma})^N} \Psi\left(N, 1; \frac{1}{c\bar{\gamma}}\right),
\end{aligned}
\tag{A.16}
$$

where (a) is obtained by applying [81, Eq. (9.211.4)].

# Appendix B

# Proofs for Chapter 4

## B.1  Generalized Gauss–Laguerre Quadrature

When analyzing the performance of the network (Fig. 4.3), we find that the following integral must be computed often:

$$I = \int_0^\infty g(x)\frac{x^\alpha e^{-x}}{\Gamma(\alpha + 1)}dx. \tag{B.1}$$

Unfortunately, since $g(x)$ is a complicated function in most cases, a closed-form solution to (B.1) is elusive. Fortunately, the evaluation of (B.1) is extremely simple with numerical quadrature. Since the details of this method are not widely available, we briefly describe it herewith. It is based on the Gauss-Laguerre quadrature. The main idea is to use function $w(x) = x^\alpha e^{-x}, \quad 0 \leq x < \infty$, to generate a set of orthogonal polynomials. Then, $g(x)$ in (B.1) is expressed as the weighted sum of these polynomials. Note that if $g(x)$ is a finite polynomial, then this expansion will be exact and error free. However, this is not the case in general. In any case, with this polynomial expansion, we can compute (B.1) as

$$I = \sum_{i=1}^n w_i g(x_i) + E_n, \tag{B.2}$$

where $E_n$ is an error term. The nodes $\{x_k\}$ are the roots of generalized Laguerre polynomials and weights $\{w_k\}$ are selected such that $E_n = 0$ if $g(x)$ is a polynomial of degree $\leq n$ [126]. Of course, in our computations, $g(x)$ is not a polynomial, but it is a smooth function which can be approximated by a polynomial with sufficiently high degree. This means $E_n \to 0$ if we choose

$n$ large enough. Fortunately, the nodes $x_k$ and weights $w_k$ can be computed easily. This is due to the fact that $\{x_k\}$ are the eigenvalues of the following, symmetric tridiagonal Jacobi matrix [127]:

$$J_n = \begin{bmatrix} u_0 & \sqrt{v_1} & & & \\ \sqrt{v_1} & u_1 & \sqrt{v_2} & & \\ & \sqrt{v_2} & \ddots & \ddots & \\ & & \ddots & u_{n-2} & \sqrt{v_{n-1}} \\ & & & \sqrt{v_{n-1}} & u_{n-1} \end{bmatrix} \tag{B.3}$$

where $u_k = 2k+\alpha+1$ and $v_k = k\,(k+\alpha)$, $k = 0,\dots n-1$. Thus, the eigenvalues of this matrix and the formula (B.3) can be easily computed in any software environment such as MATLAB with only a few lines. For instance, we give the following MATLAB code:

```
function[x, w] = GaussLagurre(n, a)
% Generate nodes and weights for
% Gauss-Lagurre quadrature.
% w(x) = x ^a * e ^(-x)
u = (2 * (0 : n-1) + a + 1);
v= sqrt((1 : n - 1) .^2 + a * (1 : n-1));
[V, D] = eig(diag(u) + diag(v, 1)
+ diag(v, -1));
[x, i] = sort(diag(D));
Vtop = V(:, i)';
w = Vtop(:, 1).^2;
```

## B.2   Necessary Integral

The following integral (B.4) frequently arises in the problems of ergodic capacity analysis and others. This integral has been derived in [128, Eq. (78)] as a summation of incomplete upper gamma function, which is more complicated than (B.5). For this reason, we give a proof below.

**Lemma 3.** *Let us consider*

$$I_n(u) = \int_0^\infty e^{-ux} x^n \log_2(1+x)dx, \tag{B.4}$$

*where $n \geq 0$ is a positive integer and $u > 0$. We can prove that*

$$I_n(u) = \log_2(e) \left[ e^u E_1(u) \sum_{k=0}^{n} \frac{n!(-1)^k}{k! u^{n-k+1}} + \sum_{k=1}^{n} \sum_{l=1}^{k} \sum_{m=0}^{l-1} \frac{n!(-1)^{k+l}}{l m!(k-l)! u^{n-k+1-m+l}} \right],$$

(B.5)

*where $n!$ is the factorial and and $E_1(x) = \int_1^\infty \frac{e^{-xt}}{t} dt$ is the exponential integral function.*

*Proof.* We note that

$$I_n(u) = (-1)^n \frac{d^n I_0(u)}{du^n}$$

(B.6)

for $n = 0, 1, \ldots$.

It is easy to show that

$$I_0(u) = \log_2(e) \frac{e^u}{u} \underbrace{\int_1^\infty \frac{e^{-ut}}{t} dt}_{=E_1(u)}.$$

(B.7)

The $n$-th derivative of $I_0(u)$ can be derived as follows:

$$
\begin{aligned}
\frac{d^n I_0(u)}{du^n} &\overset{(a)}{=} \log_2(e) \frac{d^n}{du^n} \left( \frac{e^u}{u} E_1(u) \right) \\
&\overset{(b)}{=} \log_2(e) \sum_{k=0}^{n} \binom{n}{k} \frac{d^{n-k} [u^{-1}]}{du^{n-k}} \frac{d^k [e^u E_1(u)]}{du^k} \\
&\overset{(c)}{=} \log_2(e) \sum_{k=0}^{n} \binom{n}{k} \frac{(-1)^{n-k}(n-k)!}{u^{n-k+1}} \frac{d^k [e^u E_1(u)]}{du^k} \\
&\overset{(d)}{=} \log_2(e) \sum_{k=0}^{n} \frac{n!(-1)^{n-k}}{k! u^{n-k+1}} \frac{d^k [e^u E_1(u)]}{du^k}.
\end{aligned}
$$

(B.8)

The above steps are based upon the standard formula for the derivative of the product of two functions.

The $k$-th derivative of $e^u E_1(u)$ can be derived as follows:

$$
\begin{aligned}
\frac{d^k \left[e^u E_1(u)\right]}{du^k} &\overset{(a)}{=} \frac{d^k}{du^k}\left(e^u \int_1^\infty \frac{e^{-ut}}{t}dt\right)\\
&\overset{(b)}{=} \frac{d^k}{du^k}\left(\int_1^\infty \frac{e^{-u(t-1)}}{t}dt\right)\\
&\overset{(c)}{=} (-1)^k \int_1^\infty \frac{(t-1)^k e^{-u(t-1)}}{t}dt\\
&\overset{(d)}{=} (-1)^k \int_1^\infty \sum_{l=0}^{k}\binom{k}{l}t^l(-1)^{k-l}\frac{e^{-u(t-1)}}{t}dt\\
&\overset{(e)}{=} \left[e^u E_1(u) + \int_1^\infty \sum_{l=1}^{k}\binom{k}{l}t^l(-1)^l\frac{e^{-u(t-1)}}{t}dt\right]\\
&\overset{(f)}{=} \left[e^u E_1(u) + \int_1^\infty \sum_{l=1}^{k}\binom{k}{l}t^{l-1}(-1)^l e^{-u(t-1)}dt\right]\\
&\overset{(g)}{=} \left[e^u E_1(u) + \int_0^\infty \sum_{l=1}^{k}\binom{k}{l}(t+1)^{l-1}(-1)^l e^{-ut}dt\right]\\
&\overset{(h)}{=} \left[e^u E_1(u) + \int_0^\infty (-1)^l \sum_{l=1}^{k}\sum_{m=0}^{l-1}\binom{k}{l}\binom{l-1}{m}t^{l-1-m}e^{-ut}dt\right]\\
&\overset{(i)}{=} \left[e^u E_1(u) + (-1)^l \sum_{l=1}^{k}\sum_{m=0}^{l-1}\binom{k}{l}\binom{l-1}{m}\frac{(l-m-1)!}{u^{l-m}}\right].
\end{aligned}
\tag{B.9}
$$

Since the above steps are self-explanatory, we omit the details. By substituting (B.9) in (B.8) and after some manipulations, we obtain (B.5). ∎

## B.3   Proof of Proposition 1

Since the received signal power at the IRS is random, it is possible that the SNR may drop below the required threshold, resulting in an outage. Thus, OP is defined as

$$
P_{out} = \Pr\left(\gamma < \gamma_{\mathrm{th}}\right) = \Pr\left(||\mathbf{g}||^2 < \frac{\gamma_{\mathrm{th}}}{cP_h}\right),
\tag{B.10}
$$

where $\gamma_{\mathrm{th}} = 2^R - 1$ is a predetermined threshold.

In order to evaluate (B.10), we first average over $||\mathbf{g}||^2$ while keeping $P_h$

constant:

$$P_{out}\,|_{P_h} = \int_0^{\frac{\gamma_{\text{th}}}{cP_h}} \frac{1}{\Gamma(M)} y^{M-1} e^{-y} dy$$

$$\stackrel{(a)}{=} \frac{1}{\Gamma(M)} \gamma\left(M, \frac{\gamma_{\text{th}}}{cP_h}\right),$$

(B.11)

where the above follows from the fact that $||\mathbf{g}||^2$ is Gamma distributed and the incomplete Gamma function is given by [81, Eq. (5.531.1)].

Second, since $P_h$ is a function of $||\mathbf{h}||^2$, we must average the conditional outage (B.11) over the PDF of $||\mathbf{h}||^2$. This can be done as follows

$$P_{out} = \int_0^\infty P_{out}\,|_{P_h}\, f_{||\mathbf{h}||^2}(x)\, dx$$

$$= \frac{1}{\Gamma(N)\Gamma(M)} \int_0^\infty \gamma\left(M, \frac{\gamma_{\text{th}}}{cq\left(\bar{P}_t x\right)}\right) x^{N-1} e^{-x} dx.$$

(B.12)

Finally, inserting (B.12) into (4.12), the average throughput of delay-limited mode can be expressed as (4.13).

## B.4   Proof of Proposition 2

Starting from the definition of the EC, we have

$$C_e = \mathbb{E}\left[\log_2\left(1 + cP_h||\mathbf{g}||^2\right)\right]$$

$$\stackrel{(a)}{=} \mathbb{E}\left[\frac{1}{\Gamma(M)} \int_0^\infty \log_2\left(1 + cP_h y\right) y^{M-1} e^{-y} dy\right]$$

$$\stackrel{(b)}{=} \mathbb{E}\left[\frac{1}{\Gamma(M)} (cP_h)^{-M} \int_0^\infty \log_2\left(1 + x\right) x^{M-1} e^{-\frac{x}{cP_h}} dx\right]$$

$$\stackrel{(c)}{=} \mathbb{E}\left[\frac{(cP_h)^{-M}}{\Gamma(M)} I_{M-1}\left(\frac{1}{cP_h}\right)\right]$$

$$\stackrel{(d)}{=} \frac{1}{\Gamma(N)\Gamma(M)} \int_0^\infty I_{M-1}\left(\frac{1}{cq\left(\bar{P}_t x\right)}\right) \frac{x^{N-1} e^{-x}}{\left(cq\left(\bar{P}_t x\right)\right)^M} dx,$$

(B.13)

where Step (a) is obtained by substituting the PDF of $||\mathbf{g}||^2$ into the definition of ergodic capacity; Let $x = cP_h y$ we obtain Step (b); Step (c) follows the Lemma 1; (d) is due to averaging (c) over $||\mathbf{h}||^2$.

# B.5 Proof of Proposition 3

The average BER of BPSK for a communication link that has a single antenna transmitter and multiple receive antennas with maximal ratio combining has been studied in [45, Section(14.4)]. The received SNR in this system is given by $\gamma = c||\mathbf{g}||^2$. This system is thus comparable to our WD-IRS link in Fig. 4, if $P_h$ is assumed to be constant. Using this analysis, we find

$$\begin{aligned}
\bar{P}_{BER} &= \mathbb{E}\left[Q\left(\sqrt{2cP_h||\mathbf{g}||^2}\right)\right] \\
&\stackrel{(a)}{=} \mathbb{E}\left[\left[\frac{1}{2}\left(1-\eta_1\right)\right]^M \sum_{k=0}^{M-1}\binom{M-1+k}{k}\left[\frac{1}{2}\left(1+\eta_1\right)\right]^k\right],
\end{aligned}$$
(B.14)

where $\eta_1 = \sqrt{\frac{cq\left(\bar{P}_t||\mathbf{h}||^2\right)}{1+cq\left(\bar{P}_t||\mathbf{h}||^2\right)}}$ and the Gaussian Q-function is given by $Q(x) = \frac{1}{\sqrt{2\pi}}\int_x^\infty e^{-t^2/2}dt = \frac{1}{2\sqrt{\pi}}\Gamma\left(\frac{1}{2},\frac{x^2}{2}\right)$. Step (a) above is obtained by [45, Eq. (14.4.15)]. Averaging over $||\mathbf{h}||^2$, we have (4.16).

# B.6 Proof of Proposition 4

The conditional BER of BDPSK can be expressed as $P_c(x) = \frac{1}{2}e^{-x}$. Thus, the average BER is related to the MGF method [90]. Since by definition MGF of $X$ is the expected value of random variable $e^{tX}$, where for the problem at hand $X$ is the received SNR at the IRS, we first derive the MGF of it as

$$\begin{aligned}
M(t) &= \mathbb{E}\left[e^{-cP_h||\mathbf{g}||^2 t}\right] \\
&\stackrel{(a)}{=} \mathbb{E}\left[\frac{1}{1+ctq\left(P_t||\mathbf{h}||^2\right)}\right]^M \\
&\stackrel{(b)}{=} \frac{1}{\Gamma(N)}\int_0^\infty \frac{x^{N-1}e^{-x}}{\left[1+ctq\left(P_t x\right)\right]^M}dx,
\end{aligned}$$
(B.15)

where (a) is obtained by taking the expectation over the distribution of $||\mathbf{g}||^2$, which is Gamma distributed and thus follows from and then averaging over $||\mathbf{h}||^2$, we can have (b).

Thus, the average BER of BDPSK can be obtained via (B.15), which results in (4.17).